学位論文

Hadron-Quark Crossover and Massive Neutron Stars

(ハドロンクォーククロスオーバーと重い中性子星)

平成２７年１２月博士（理学）申請

東京大学大学院理学系研究科
物理学専攻
益田　晃太

Hadron-Quark Crossover and Massive Neutron Stars

Kota Masuda

Department of Physics, The University of Tokyo

December 2015

PhD Thesis

Abstract

Bulk properties of cold and hot neutron stars (NSs) are studied on the basis of the hadron-quark crossover picture where a smooth transition from the hadronic phase to the quark phase takes place at finite baryon density. We developed a phenomenological equation of state (EOS) "CRover" EOS, which interpolates the two phases at around 3 times the nuclear matter density (ρ_0), and found that the cold NSs with the gravitational mass larger than $2M_\odot$ can be sustained. This is in sharp contrast to the case of the first-order hadron-quark transition where the quark matter inevitably leads to soft EOS. We show this novel stiffening of EOS by the appearance of quark matter through the hadron-quark crossover does not depend on the methods of interpolation nor the choice of hadronic EOSs. The radii of the cold NSs with the CRover EOS are in the narrow range (12.5 ± 0.5) km which is insensitive to the NS masses. Due to the stiffening of the EOS induced by the hadron-quark crossover, the central density of the NSs is at most 4 ρ_0 and the hyperon-mixing barely occurs inside the NS core if we have the repulsive three body force between hyperons. This constitutes a solution of the long-standing hyperon puzzle about the maximum mass and the rapid cooling of neutron stars with hyperons. The effect of color superconductivity (CSC) on the NS structures is also examined with the hadron-quark crossover. For the typical strength of the diquark attraction, a slight softening of the EOS due to two-flavor CSC (2SC) takes place at the core of neutron stars and the maximum mass is reduced by about 0.2 $M_\odot$. However, the maximum mass of NSs sustained by this phenomenological EOS with CSC can still exceed $2M_\odot$. Through the percolation of nucleons to quarks with the diquark correlation, the effects of CSC can be seen even in low mass neutron stars. The CRover EOS is also generalized to the supernova matter at finite temperature to describe the hot NSs at birth. The hadron-quark crossover is found to decrease the central temperature of the hot NSs under isentropic condition due to the color degrees of freedom. The gravitational energy release and the spin-up rate during the contraction from the hot NS to the cold NS are also estimated.

Table of Contents

1 Introduction **1**

2 The Hadronic Phase **9**

2.1 Phenomenological Baryon-Baryon Interactions 9

2.2 Models for Hadronic EOS 14

2.3 Hyperon Puzzle 18

2.4 Brief Summary 20

3 The Quark Phase **23**

3.1 $\bar{q}q$ Correlation 23

3.2 qq Correlation 25

3.3 Chiral Anomaly 27

3.4 $(2+1)$-flavor Nambu-Jona-Lasinio (NJL) Model 27

3.5 Brief Summary 34

4 Cold Neutron Stars with Crossover **35**

4.1 Phenomenological Model for Crossover 35

4.2 Neutron Star Properties with P-interpolation without CSC 38

4.2.1 Interpolated EOS 38

4.2.2 Mass-Radius Relation 39

4.2.3 Dependence on Q-EOS 43

4.2.4 Dependence on Crossover Window 44

4.2.5 Sound Velocity of Interpolated EOS 44

4.2.6 Stability of Hybrid Star 45

4.3 Neutron Star Properties with ε-interpolation without CSC 46

4.3.1 Interpolated EOS 46

4.3.2 Bulk Properties of NSs 48

4.4 Neutron Star Properties with ε-interpolation with CSC 49

4.5 Brief Summary 51

5 Hot Neutron Stars with Crossover **53**
5.1 Hot Neutron Stars 53
5.2 Crossover at Finite Temperature 54
5.3 Construction of Hot EOS 56
5.4 Bulk Properties of Hot Neutron Stars 57
5.5 Brief Summary 63

6 Summary and Discussion **65**

A Magnetic Properties of Neutron $^3P_2$ Superfluids **71**
A.1 Magnetic Field of NSs 71
A.2 Ginzburg Landau Free Energy for $^3P_2$ Superfluids and the Ground State 72
A.3 Vortex Structures in $^3P_2$ Superfluids 75
A.4 Vortex Solutions 79
A.5 Spontaneous Magnetization of the $^3P_2$ Vortex Core 80

B Tolman-Oppenheimer-Volkov Equation **83**

C Fierz Transformation **87**

D The Bogoliubov-Valatin Approach **91**

E Calculation of the Thermodynamic Potential **95**

F Crossover at Finite Temperature **99**

Original works related to the present thesis.

Contents	Original works
Section 2.3: Hyperon Puzzle	[1, 2, 3]
Section 3.4: $(2+1)$-flavor Nambu-Jona-Lasinio (NJL) Model	[1, 2, 3]
Chapter 4: Cold Neutron Stars with Crossover	[1, 2, 3]
Chapter 5: Hot Neutron Stars with Crossover	[3, 4]
Appendix A: Magnetic Properties of Neutron ${}^3P_2$ Superfluids	[5]

Chapter 1

Introduction

The strongly interacting systems of quarks and gluons are known to be described by quantum chromo dynamics (QCD) which is the color $SU(3)_C$ gauge theory with the Lagrangian $\mathcal{L}_{\rm QCD}$ below [6]:

$$\mathcal{L}_{\rm QCD} = \overline{q}^f_\alpha (i\gamma^\mu D^{\alpha\beta}_\mu - m_f \delta^{\alpha\beta}) q^f_\beta - \frac{1}{4} F^a_{\mu\nu} F^{a\mu\nu}. \tag{1.1}$$

where

$$\begin{aligned} F^a_{\mu\nu} &= \partial_\mu A^a_\nu - \partial_\nu A^a_\mu + g f^{abc} A^b_\mu A^c_\nu, \\ D_\mu &= \partial_\mu - igt^a A^a_\mu, \end{aligned}$$

$A^a_\mu (a = 1, ..., 8)$ is the gauge field in the adjoint representation, q^f_α is the quark field in the fundamental representation (α and f are color and flavor respectively), g is the coupling constant of the strong interaction and m_f is the current mass matrix for the flavor space. The generators for $SU(3)_C$, t_a, are defined by $t_a \equiv \frac{1}{2}\tau_a$ where τ_a are the Gell-Mann matrices. They are normalized by the condition $\mathrm{Tr}(t^a t^b) = \frac{1}{2}\delta^{ab}$. f^{abc} are the structure constant defined by $[t_a, t_b] = i f^{abc} t_c$. The fine structure constant in QCD, $\alpha_s = g^2/(4\pi)$, which is an effective coupling strength among quarks and gluons at the energy scale Q, is governed by the QCD beta-function $\beta(\alpha_s) \equiv Q^2 \frac{d\alpha_s}{dQ^2}$. For large Q, the beta function can be evaluated by perturbation theory as

$$\beta(\alpha_s) = -(b_0 \alpha_s^2 + b_1 \alpha_s^3 + b_2 \alpha_s^4 + ...). \tag{1.2}$$

In the $\overline{MS}$ renormalization scheme, the numerical constants, $b_{0,1,2}$, are given as $b_0 = \frac{33-2N_f}{12\pi}$, $b_1 = \frac{153-19N_f}{24\pi^2}$ and $b_2 = \left(2857 - \frac{5033}{9}N_f + \frac{325}{27}N_f^2\right)/(128\pi^3)$ where N_f is the number of flavors. From this differential equation (1.2), we can evaluate the running coupling constant as follows [7]

$$\begin{aligned} \alpha_s(Q^2) &= \frac{1}{b_0 t}\left(1 - \frac{b_1}{b_0^2}\frac{\log t}{t} + \frac{b_1^2((\log t)^2 - \log t - 1) + b_0 b_2}{b_0^4 t^2}\right. \\ &\quad \left. - \frac{b_1^3\left((\log t)^3 - \frac{5}{2}(\log t)^2 - 2\log t + \frac{1}{2}\right) + 3 b_0 b_1 b_2 \log t}{b_0^6 t^3}\right), \end{aligned} \tag{1.3}$$

$$t \equiv \log(Q^2/\Lambda^2_{\rm QCD}) \tag{1.4}$$

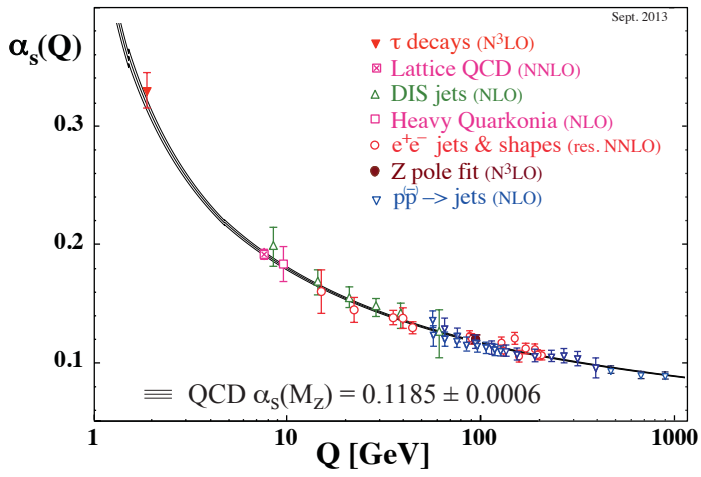

Figure 1.1: The coupling constant α_s as a function of the energy scale Q. At the high energy scale, we can see $g(Q) \to 0$ ($Q^2 \to \infty$), which corresponds to the asymptotic freedom. On the other hand, at low energy scale, the non-perturbative effects can be seen. At around $Q \sim \Lambda_{\rm QCD}$, the confinement of quarks occurs. This figure is taken from [7].

up to the 3-loop calculation. Here $\Lambda_{\rm QCD}$ is the energy scale, at which the coupling constant becomes divergent and the non-perturbative effects of QCD appear.

In Fig. 1.1, we show the behavior of the running coupling constant [7]. Since b_0 is positive in QCD, $\alpha_s(Q) \to 0$ ($Q^2 \to \infty$). As a result, the coupling constant becomes small as the system scale becomes high energy. This property is called as the asymptotic freedom and is a unique property of the non-Abelian gauge theory such as QCD [8, 9]. On the other hand, the other important feature for QCD, confinement of quarks, takes place at the low energy scale $Q \sim \Lambda_{\rm QCD}$ where the coupling becomes strong and the perturbation theory breaks down. Experimentally, only the confinement of quarks and gluons is observed and isolated quarks and gluons have never been observed.

Due to these non-perturbative effects, strongly interacting matter described by QCD is believed to have a rich phase structure under the change of external parameters such as the temperature (T) and the baryon chemical potential (μ) [11] as shown Fig. 1.2. At low T and μ, the system is in the hadronic phase where the dynamical breaking of chiral symmetry (we discuss the chiral symmetry in detail in Chapter 3) and the confinement of quarks and gluons take place. At high T and low μ, the quark-gluon plasma with deconfined quarks and gluons was predicted theoretically and is under active experimental studies by the relativistic heavy-ion collisions (HIC) at relativistic heavy ion collider (RHIC) and large hadron collider (LHC) [12]. At low T and high μ, the superconducting quark matter with deconfined quarks is expected to appear, which is relevant to the central core of neutron stars [13].

The transition from the hadronic matter to the quark-gluon plasma at high T has been

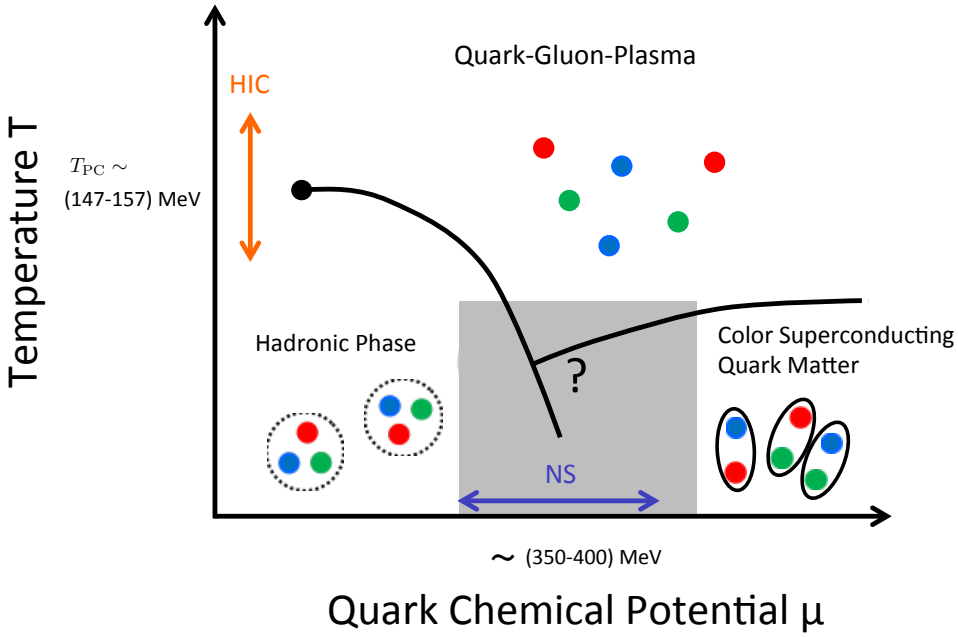

Figure 1.2: Schematic QCD phase diagram at finite temperature (T) and at finite quark chemical potential (μ) . As the temperature increases, the chiral symmetry is partially restored and the quark-gluon plasma with deconfined quarks and gluons emerges. Physics along the vertical axis is under active experimental studies by the relativistic heavy-ion collisions at RHIC and LHC and studied by the lattice QCD simulations theoretically. The pseudo critical temperature $T_{\rm PC}$ is estimated as $(147-157)$MeV in [10]. As the quark chemical potential increases, the superconducting quark matter with deconfined quarks is expected to appear. QCD properties along the horizontal axis still is not understood well since Monte Carlo simulations in lattice QCD cannot be done due to the sign problem. The finite size baryons start to overlap with each other and the percolation of quarks will take place at about $\mu \sim (350-400)$MeV from the rough estimation.

studied quantitatively by using the lattice QCD Monte Carlo simulations [10]. The results from the lattice QCD Monte Carlo simulations predict the crossover transition from the hadronic phase to this quark-gluon plasma phase at the pseudo critical temperature $T_{\rm PC} \sim (147-157)$MeV for physical quark masses in the continuum limit with $N_f = 2+1$ flavor case [10]. On the other hand, the transition from the hadronic matter to the quark matter at high μ is not well understood partly due to the lack of reliable first-principle theoretical methods; the Monte Carlo simulations in lattice QCD are not suitable for $\mu/T \gg 1$ because of the fermion sign problem [11]. Let us make a phenomenological estimate of the quark chemical potential μ where the transition from the hadronic phase to the quark phase takes place. As the baryon density increases, the finite size baryons start to percolate at a certain baryon density $\rho_{\rm per}$. This baryon density can be characterized by $\frac{1}{\rho_{\rm per}} = \frac{4\pi}{3} r_b^3$, where r_b is the radius of baryons. If we take $r_b = 0.8(0.5)$ fm, which corresponds to the proton charge radius [7] (the range of the repulsive core of the nuclear force [14]), we obtain $\rho_{\rm per} \sim 0.466(1.91)/\text{fm}^3$. Since the quark

chemical potential μ is related with the baryon number density ρ by $\rho = \frac{2\mu^3}{3\pi^2}$ for the u and d quark matter and at zero temperature, the typical quark chemical potential μ for the transition from the hadronic phase to the quark phase can be estimated as 351(402)MeV.

Under such circumstance, any information from neutron stars (NSs), whose central cores may reach the baryon density relevant to the hadron-quark transition, provides us with a testing ground for the rich phase structure of QCD through the observables such as the mass (M), the radius (R), the surface temperature ($T_{\rm sur}$), the surface magnetic field ($B_{\rm sur}$)[1] and so on [15]. Among these observables, M and R are particularly important probes for constraining the equation of state (EOS) and the composition of high density matter.

In Fig. 1.3 (a), we show the observed NS mass list, which is taken from [15]. We can see the masses for double NS binaries can be determined very well and the canonical masses for the neutron star binaries are about $1.4M_\odot$. Recently, a massive NS (PSR J1614-2230) with $M = (1.97 \pm 0.04)M_\odot$ has been observed through the Shapiro delay technique [17] and another massive NS (PSR J0348+0432) with $M = (2.01 \pm 0.04)M_\odot$ [18] was also reported. Especially, it is believed that the first observation is very reliable since the mass determination requires only the Shapiro delay technique, which is the pure effect of general relativity. We will discuss the impact of this observation on nuclear physics in detail in Chapter 2.

Theoretically, we can obtain a mass and radius relation (M-R relation) through Tolman-Oppenheimer-Volkov (TOV) equation [2],

$$\begin{aligned} \frac{dP}{dr} &= -\frac{G}{r^2}\left(M(r) + 4\pi P r^3\right)(\varepsilon + P)\left(1 - 2GM(r)/r\right)^{-1} \\ M(r) &= \int_0^r 4\pi r'^2 \varepsilon(r') dr' \end{aligned} \tag{1.5}$$

where we have assumed the spherical symmetry with r being the radial distance from the center of the star. Fig. 1.3 (b) shows the M-R relation by phenomenological polytrope EOSs[3], which can sustain $1.97M_\odot$-NS [16]. From Fig. 1.3 (b), the radius of NSs sustained by EOSs consistent with the causality and the crust BPS EOS [19] around ρ_0, which is a well-established EOS below ρ_0, is in the range, $(10-13)$km. This result is consistent with the results from the observations of the quiescent low mass X-ray binaries (qLMXB) and photospheric radius expansion (PRE) X-ray bursts with some uncertainties [20, 21, 22, 23].

Let us turn to the internal compositions of NSs. The onset of the strangeness degrees of freedom inside the NSs has attracted much attention in recent years: General consensus is that the hyperons (Y) such as Λ and Σ^- would participate in NS cores at densities of several times nuclear matter density [24, 25, 26, 27, 28, 29, 30]. As we will discuss in Chapter 2, strong

[1] We consider the spontaneous magnetization along quantized vortices in the neutron $^3P_2$ superfluidity in Appendix A.

[2] We derive the TOV equation in Appendix B.

[3] Polytrope type EOSs are given by $P = K\rho^{1+\frac{1}{\gamma}}$. Here γ is called as the adiabatic index defined by $\gamma \equiv d\log P / d\log\rho$.

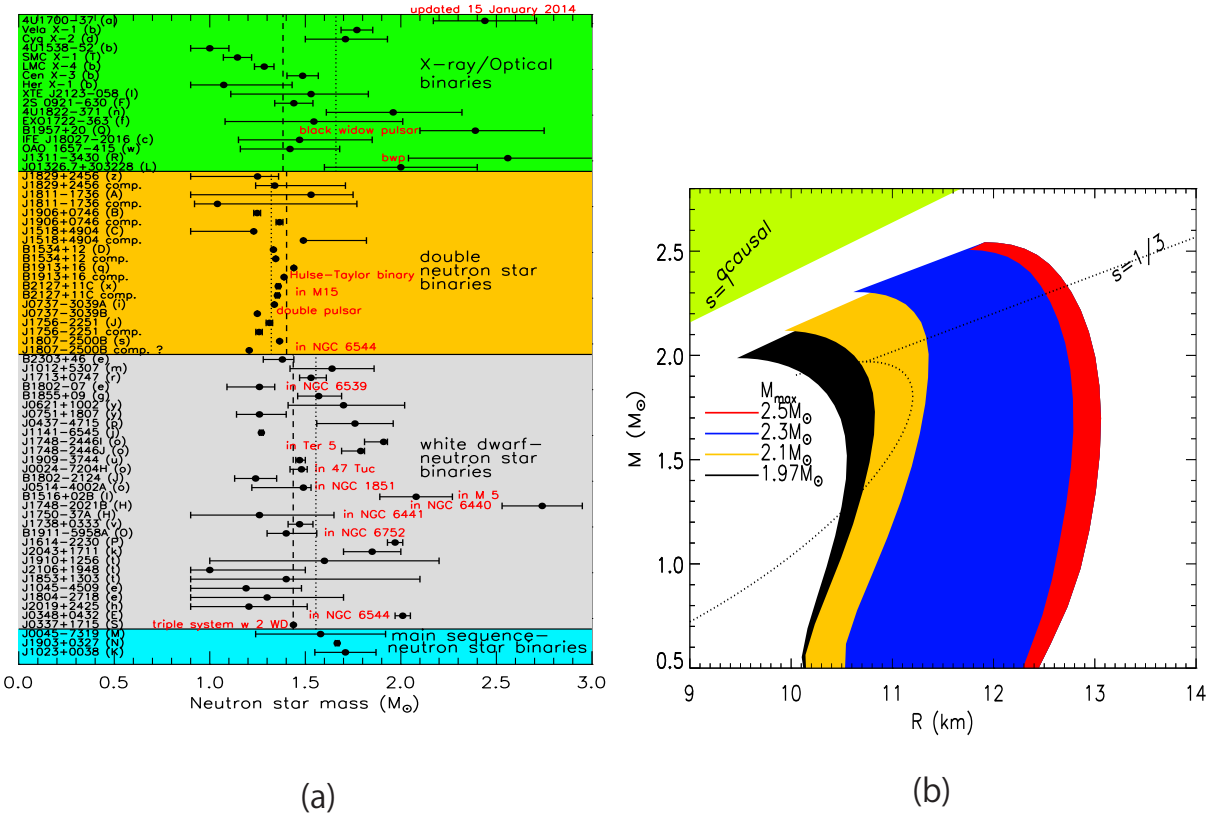

Figure 1.3: (a) The observed neutron star mass list. For neutron star binaries, the typical neutron star mass is about $1.4M_\odot$. In 2010, the very massive neutron star with $(1.97 \pm 0.04)M_\odot$ is observed through the Shapiro delay technique. The other massive neutron star with $(2.01 \pm 0.04)M_\odot$ was also reported in 2013. This figure is taken from [15]. (b) Mass and Radius relations (M-R relation) obtained through the TOV equation. Polytrope type EOSs smoothly connected with BPS crust EOS at $\rho_0/2.7$ are used. Black, orange, blue and red regions correspond to EOSs whose maximum masses are $1.97, 2.1, 2.3$ and $2.5M_\odot$ respectively. The light green shaded area means the region where the causality is violated. The radius of NSs lighter than $2M_\odot$ can be restricted in the region, $(10 - 13)$km. This figure is taken from [16].

softening of EOS takes place due to the hyperon mixture. As a result, even the canonical mass $1.4M_\odot$ cannot be sustained with the hyperon mixture. We need some repulsive forces at high density region such as the three body force between hyperons [31]. To solve the confliction between the observation of massive NSs and the appearance of hyperons in the core of NSs is one of the most important topics related with NSs.

The hot NS also provides us with various information on the properties and dynamics of high density matter with finite temperature [32, 33]. In the core-collapsed Type-II supernova explosion, the proto-neutron star (PNS) with the radius $\sim 100-200$ km is formed. During the first few seconds after the core bounce, the PNS undergoes a rapid contraction and evolves into either a "hot" neutron star with the radius $\sim 10-20$ km or a black hole. The hot NS at birth in quasi-hydrostatic equilibrium is composed of the supernova matter with the typical lepton

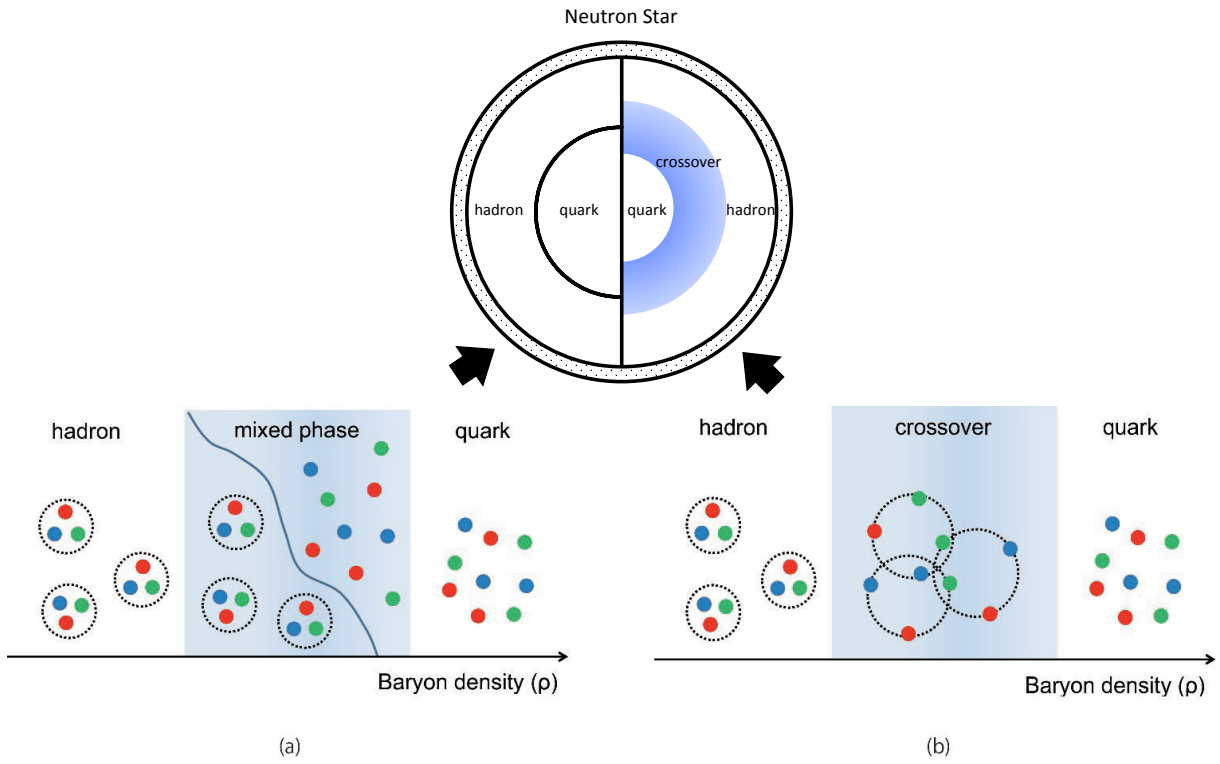

Figure 1.4: Schematic pictures of the relation between the neutron star interior and how the transition to the quark matter takes place and the QCD phases as a function of the baryon density (ρ) under the assumption of (a) the first-order transition and (b) the hadron-quark crossover. The dotted area at the surface of a neutron star is the crust. The mixed-phase region in (a) and the crossover region in (b) are indicated by the shaded area. This figure is adopted from [3].

fraction, $Y_l = Y_e + Y_\nu \sim 0.3 - 0.4$, and the typical entropy per baryon [4], $\hat{S} \sim 1 - 2$: They are caused by the neutrino trapping at the baryon density ρ exceeding $10^{12}\mathrm{g/cm}^3$. With this as an initial condition, the hot NS contracts gradually by the neutrino diffusion with the time scale of several tens of seconds and evolves to a nearly "cold" NS with $Y_\nu \simeq 0$ and $\hat{S} \simeq 0$), unless another collapse to a black hole does not take place [34, 35, 36].

The main purpose of this thesis is to investigate whether the "hybrid stars" which have quark matter in the core are compatible with $2M_\odot$-NS. Historically, the transition from the hadronic matter to the quark matter has been assumed to be of first order and the Gibbs phase equilibrium conditions are imposed. However, treating the point-like hadron as an independent degree of freedom is not fully justified in the transition region because all hadrons are extended objects composed of quarks and gluons. Furthermore, the system must be strongly interacting in the transition region, so that it can be described neither by an extrapolation of the hadronic EOS from the low-density side nor by an extrapolation of the quark EOS from the high-density

[4] Throughout this thesis, we put hat-symbol for the thermodynamic quantities per baryon.

side [37]. This is analogous to the BEC-BCS crossover realized in the many-body system of ultra-cold fermionic atoms [38].

Fig. 1.4 illustrates the relation between the NS interior and how the phase transition occurs and the difference between (a) the first-order transition where the phase separation between hadrons and quarks takes place, and (b) the crossover where the percolation of finite size hadrons takes place. Such a percolation picture of hadrons has been first discussed in Refs.[39, 40], and later elaborated in the contexts of the hadron-quark continuity [41, 42] and the hadron-quark crossover [43, 44].

This thesis is organized as follows. In Chapter 2, after we briefly introduce the phenomenological nuclear force, some effective models to describe hadronic EOSs (H-EOSs) are introduced. The characteristic features of H-EOSs to be used at low density region are summarized. In section 2.3, we note the hyperon puzzle which is the contradiction between the observation of massive NSs and the softening of EOS due to the hyperon mixture. We show M-R relations for various hadronic EOSs with and without hyperons. The calculation was done by Prof. Takatsuka and me. In Chapter 3, after summarizing the dynamical breaking of chiral symmetry in QCD as well as the color superconductivity, we investigate the strongly interacting quark matter by using the $(2+1)$-flavor Nambu-Jona-Lasinio (NJL) type model and derive the quark EOS (Q-EOS) to be used at high densities. The calculation about this Q-EOS was done by me. In Chapter 4, we introduce an interpolation procedure at zero temperature to obtain the EOS (CRover-C EOS) in the smooth hadron-quark crossover picture by considering the pressure (P) or energy density (ε) as a basic quantity. Then, we discuss the bulk properties of cold hybrid stars, such as the M-R relationship, the maximum mass $M_{\rm max}$ and the M-ρ_c(central density) relationship with CRover-C EOS. We also discuss how these results depend on the different choice of H-EOSs and Q-EOSs. A comment on the cooling of NSs with respect to the hyperon mixture inside the core is also given. We show the effects of color superconducting (CSC) phase on the bulk properties of NSs are small. After our original works for cold NSs [1, 2], similar phenomenological models with similar conclusions for cold NSs have been reported by several other groups [45, 46, 47]. In Chapter 5, we generalize the idea of the hadron-quark crossover at zero temperature to finite temperature by considering the Helmholtz free energy $F(N, V, T)$ as a basic quantity to interpolate the hadronic matter and the quark matter. Here N and V are the total baryon number and the total volume, respectively. By using this phenomenological EOS (CRover-H EOS) for supernova matter with fixed Y_l and $\hat{S}$, we study not only the bulk observables such as M-R relation of the hot neutron star at birth, but also the temperature, density and sound velocity profiles inside the star. In chapter 4 and 5, phenomenological interpolation methods are suggested by Prof. Hatsuda, Prof. Takatsuka and me. Calculations of cold and hot NS bulk properties was done by me. Chapter 6 is devoted to summary and discussion.

Chapter 2

The Hadronic Phase

In this chapter, we first summarize the phenomenological models for the two body nuclear force and three body force which reproduce the nuclear saturation properties. Then, by using G-matrix, which is a many-body method to include the medium effect, we construct the hadronic EOSs with and without hyperons. With these EOSs, M-R relations are derived. Finally we point out that the universal three-body repulsion among baryons, which is necessarily to sustain the canonical $1.4M_\odot$ NSs, is still not enough to sustain $2M_\odot$ NSs.

2.1 Phenomenological Baryon-Baryon Interactions

After the introduction of the meson theory by Yukawa in 1935 [48], Taketani proposed that the nuclear force can be divided into three parts [49, 50] as shown in Fig. 2.1: (I) the phenomenological repulsive part $rM_\pi \lesssim 0.7$, (II) the intermediate region $0.7 \lesssim rM_\pi \lesssim 1.5$ where the two pion exchange or the heavy meson exchange are dominant and (III) the long range part $1.5 \lesssim rM_\pi$ where the one pion exchange (OPE) is dominant. Here M_π is the pion mass. Below, we introduce several examples of phenomenological baryon interactions to be used in our analysis.

Reid Soft Core NN Potential [51]

Reid "soft core" NN potential is written as

$$V_{\rm Reid} = V_c(M_\pi r) + V_{12}(M_\pi r)S_{12} + V_{LS}(M_\pi r)\boldsymbol{L}\cdot\boldsymbol{S}. \tag{2.1}$$

Here, the first term is the central potential, the second term is the tensor potential and the third term is the spin-orbit potential. An operator S_{ij} is defined as

$$S_{ij} = 3(\boldsymbol{\sigma}_i\cdot\hat{\boldsymbol{r}}_{ij})(\boldsymbol{\sigma}_j\cdot\hat{\boldsymbol{r}}_{ij}) - \boldsymbol{\sigma}_i\cdot\boldsymbol{\sigma}_j, \tag{2.2}$$

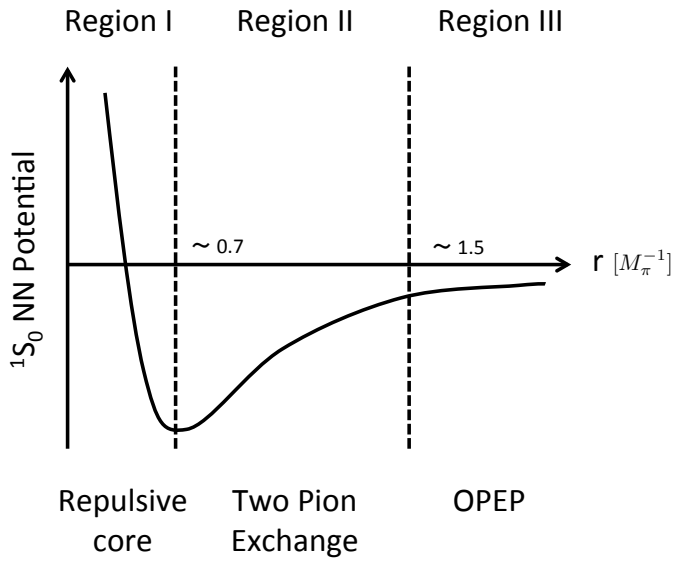

Figure 2.1: The nuclear force can be divided into three regions. (I) Short range region with the repulsive core. (II) Intermediate region where the two pion exchange or the heavy meson exchange become dominant. (III) Long range region where the one pion exchange is dominant.

and $V_c(x)$, $V_{12}(x)$ and $V_{LS}(x)$ are

$$V_c(x) = \sum_{n=1}^{\infty} a_n \frac{e^{-nx}}{x}, \quad V_{LS}(x) = \sum_{n=1}^{\infty} c_n \frac{e^{-nx}}{x}, \tag{2.3}$$

$$V_{12}(x) = \frac{b_1}{x}\left(\frac{1}{3} + \frac{1}{x} + \frac{1}{x^2}\right) e^{-x} + \sum_{n=2}^{\infty} b_n \frac{e^{-nx}}{x}. \tag{2.4}$$

a_1, b_1 and c_1 are determined to reproduce the one pion exchange potential (OPEP) $V_{\rm OPEP}$ defined as

$$V_{\rm OPEP} = \frac{G_{\pi N}^2}{3}(\boldsymbol{\tau}_1 \cdot \boldsymbol{\tau}_2)\left[\frac{e^{-M_\pi r}}{r}(\boldsymbol{\sigma}_1 \cdot \boldsymbol{\sigma}_2) + \left(1 + \frac{3}{M_\pi r} + \frac{3}{(M_\pi r)^2}\right)\frac{e^{-M_\pi r}}{r} S_{12}\right] \tag{2.5}$$

where $\boldsymbol{\tau}$ is the isospin matrices and $G_{\pi N}$ is the coupling constant between pions and nucleons. Other coefficients (up to $n = 7$) are determined to reproduce the NN scattering data with the total angular momentum $J \leq 2$. For $J \geq 3$, OPEP is used.

Paris NN Potential [52]

Paris group proposed a different phenomenological NN potential $V_{\rm Paris}$,

$$V_{\rm Paris} = V_0(r, p^2)\Omega_0 + V_1(r, p^2)\Omega_1 + V_{12}(r)S_{12} + V_{LS}(r)\boldsymbol{L} \cdot \boldsymbol{S} + V_Q(r)Q_{12} \tag{2.6}$$

where

$$\Omega_0 = \frac{1 - \boldsymbol{\sigma}_1 \cdot \boldsymbol{\sigma}_2}{4}, \quad \Omega_1 = \frac{3 + \boldsymbol{\sigma}_1 \cdot \boldsymbol{\sigma}_2}{4}, \tag{2.7}$$

$$Q_{12} = 2(\boldsymbol{L}\cdot\boldsymbol{S})^2 + \boldsymbol{L}\cdot\boldsymbol{S} - \boldsymbol{L}^2. \tag{2.8}$$

Q_{12} is a quadratic LS potential. The important point of Paris potential is that the central potential depends on the velocity $|\boldsymbol{p}|$ in the following way,

$$V_{0,1}(r,p^2) = V^a_{0,1}(r) + \frac{\boldsymbol{p}^2}{M}V^b_{0,1}(r) + V^b_{0,1}(r)\frac{\boldsymbol{p}^2}{M} \tag{2.9}$$

where $\boldsymbol{p}$ is the momentum operator and M is the nucleon mass. The coefficients $V^a_{0,1}$, $V^b_{0,1}$ and $V_{12,LS,Q}$ are defined as

$$V^a_0(r) = \sum_{n=1}^{\infty} a_n \frac{e^{-m_n r}}{m_n r}, \quad V^a_1(r) = \sum_{n=1}^{\infty} b_n \frac{e^{-m_n r}}{m_n r}, \tag{2.10}$$

$$V^b_0(r) = \sum_{n=1}^{\infty} c_n \frac{e^{-m_n r}}{m_n r}, \quad V^b_1(r) = \sum_{n=1}^{\infty} d_n \frac{e^{-m_n r}}{m_n r}, \tag{2.11}$$

$$V_{12}(r) = \sum_{n=1}^{\infty} e_n \left(1 + \frac{3}{m_n r} + \frac{3}{(m_n r)^2}\right)\frac{e^{-m_n r}}{m_n r}, \tag{2.12}$$

$$V_{LS}(r) = \sum_{n=1}^{\infty} f_n \left(\frac{1}{m_n r} + \frac{1}{(m_n r)^2}\right)\frac{e^{-m_n r}}{m_n r}, \tag{2.13}$$

$$V_Q(r) = \sum_{n=1}^{\infty} g_n \frac{1}{(m_n r)^2}\left(\frac{1}{m_n r} + \frac{1}{(m_n r)^2}\right)\frac{e^{-m_n r}}{m_n r}. \tag{2.14}$$

The coefficients $a_n, b_n, c_n, d_n, e_n, f_n$ and m_n with $n = 1$ are determined to reproduce OPEP in Eq. (2.5). Other coefficients (up to $n = 12$) are determined to reproduce NN scattering data.

Argonne V18 NN potential [53]

One of the modern and high-precision phenomenological potentials is the Argonne V18 (AV18) potential. Here, the potential V_{AV18} is decomposed into 18 parts:

$$V_{AV18} = \sum_{i=1,18} V^i \mathcal{O}_i \tag{2.15}$$

where $\mathcal{O}_i$ are the central, spin-spin, tensor, LS, centrifugal and quadratic centrifugal terms with and without isospin dependence,

$$\begin{aligned}\mathcal{O}_i = \quad & 1, \boldsymbol{\tau}_1\cdot\boldsymbol{\tau}_2, \boldsymbol{\sigma}_1\cdot\boldsymbol{\sigma}_2, (\boldsymbol{\sigma}_1\cdot\boldsymbol{\sigma}_2)(\boldsymbol{\tau}_1\cdot\boldsymbol{\tau}_2), S_{12}, S_{12}(\boldsymbol{\tau}_1\cdot\boldsymbol{\tau}_2), (\boldsymbol{L}\cdot\boldsymbol{S}), (\boldsymbol{L}\cdot\boldsymbol{S})(\boldsymbol{\tau}_1\cdot\boldsymbol{\tau}_2), \boldsymbol{L}^2, \\ & \boldsymbol{L}^2(\boldsymbol{\tau}_1\cdot\boldsymbol{\tau}_2), \boldsymbol{L}^2(\boldsymbol{\sigma}_1\cdot\boldsymbol{\sigma}_2), \boldsymbol{L}^2(\boldsymbol{\sigma}_1\cdot\boldsymbol{\sigma}_2)(\boldsymbol{\tau}_1\cdot\boldsymbol{\tau}_2), (\boldsymbol{L}\cdot\boldsymbol{S})^2, (\boldsymbol{L}\cdot\boldsymbol{S})^2(\boldsymbol{\tau}_1\cdot\boldsymbol{\tau}_2), \\ & T_{12}, T_{12}(\sigma_1\cdot\sigma_2), S_{12}T_{12}, (\tau_1)_z + (\tau_2)_z\end{aligned} \tag{2.16}$$

where

$$T_{ij} = 3(\tau_i)_z(\tau_j)_z - \boldsymbol{\tau}_i\boldsymbol{\tau}_j. \tag{2.17}$$

The coefficient V^i can be divided into three parts related with Taketani's three regions,

$$V^i = V^i_\pi + V^i_R + V^i_{EM}. \tag{2.18}$$

Here V_π is OPEP, V_R is the potential for the remaining parts (the short range region and the intermediate region) and V_{EM} is the electromagnetic potential including one and two photon exchange, Darwin-Foldy potential, vacuum polarization and magnetic-moment interaction. AV18 potential includes 40 parameters which are fitted to reproduce pp and np scattering data in the Nijmegen database, low energy nn scattering parameters and the deutron binding energy.

Hyperon-Nucleon and Hyperon-Hyperon Interactions

Since the experimental data on the hyperon (Y)-nucleon (N) and Y-Y interactions are still limited, we take the Nijmegen one-boson-exchange potential for these interactions. It is based on the flavor $SU(3)$ classification of baryons and mesons. For example, the eight $J^P = \frac{1}{2}^+$ baryon octet B can be written

$$B = \begin{pmatrix} \frac{\Sigma^0}{\sqrt{2}} + \frac{\Lambda}{\sqrt{6}} & \Sigma^+ & p \\ \Sigma^- & -\frac{\Sigma^0}{\sqrt{2}} + \frac{\Lambda}{\sqrt{6}} & n \\ -\Xi^- & \Xi^0 & -\frac{2\Lambda}{\sqrt{6}} \end{pmatrix}. \tag{2.19}$$

The scalar, pseudo scalar, vector and axial vector mesons form $SU(3)$-nonets, respectively. For example, the pseudo-scalar nonet with $J^P = 0^-$ reads

$$M_{PS} = \frac{\eta_0}{\sqrt{3}}\mathbf{1} + \begin{pmatrix} \frac{\pi^0}{\sqrt{2}} + \frac{\eta_8}{\sqrt{6}} & \pi^+ & K^+ \\ \pi^- & -\frac{\pi^0}{\sqrt{2}} + \frac{\eta_8}{\sqrt{6}} & K^0 \\ K^- & \bar{K}^0 & -\frac{2\eta_8}{\sqrt{6}} \end{pmatrix}. \tag{2.20}$$

Then, the $SU(3)$ invariant couplings between the baryon octet and pseudo-scalar nonet have three possible structures, F-type, D-type and S-type:

$$[\bar{B}BM_{PS}]_F = \mathrm{tr}(\bar{B}M_{PS}B) - \mathrm{tr}(\bar{B}BM_{PS}), \tag{2.21}$$

$$[\bar{B}BM_{PS}]_D = \mathrm{tr}(\bar{B}M_{PS}B) + \mathrm{tr}(\bar{B}BM_{PS}) - \frac{2}{3}\mathrm{tr}(\bar{B}B)\mathrm{tr}(M_{PS}), \tag{2.22}$$

$$[\bar{B}BM_{PS}]_S = \mathrm{tr}(\bar{B}B)\mathrm{tr}(M_{PS}). \tag{2.23}$$

By using these combinations, we can construct $SU(3)$ flavor symmetric Lagrangian $\mathcal{L}_{\mathrm{NIJ}}$,

$$\mathcal{L}_{\mathrm{NIJ}} = G_{\mathrm{OCT}}\{\alpha[\bar{B}BM_{PS}]_F + (1-\alpha)[\bar{B}BM_{PS}]_D\} + G_{\mathrm{SIN}}[\bar{B}BM_{PS}]_S \tag{2.24}$$

where G_{OCT} and G_{SIN} are the coupling constants and α means the ratio between F and D type interactions. By using this Lagrangian together with other couplings to scalar and vector

mesons, one may construct the phenomenological NN, YN and YY interactions with certain constraints from the experimental NN and YN scattering data.

Baryon-Baryon interactions with with scalar, pseudo-scalar, and vector mesons with the D (F) type couplings with phenomenological hard-core repulsion are called the Nijmegen D (F) potentials [54]([55]). More sophisticated potentials of this type with a phenomenological soft-core repulsion and fine-tuned spin-spin interactions are called Nijmegen NSC97a-f models [56]. In Table 2.1, we summarize the single particle potential of Λ for each partial wave in ND, NF and NSC97a-f. We note that it is important to have new data on hyperon interactions from the Y-N scattering and hypernuclei experiments at J-PARC [57, 58, 59] and also from the lattice QCD simulations at the physical quark masses [60].

Three Body Force

By using phenomenological two baryon forces, we can derive hadronic EOSs by using nuclear many-body methods to be explained shortly. To reproduce the experimental data, we need the attractive force at low density region and the repulsive force at high density region. The three body forces are considered as one of origins of such effects. At present, many phenomenological three body forces have been proposed. Here, we show two examples; (I) Three Nucleon Interaction (TNI) model suggested by Lagaris-Pandharipande and (II) Urbana IX type phenomenological Three Body Force (TBF) [62, 63]. The TNI three body potential $V_{\rm TNI}$ is

$$\begin{aligned} V_{\rm TNI} &= V_{\rm TNA} + V_{\rm TNR} \\ &= V_2 e^{-(r/\lambda_a)^2} \rho e^{-\eta_2 \rho} (\boldsymbol{\tau}_1 \cdot \boldsymbol{\tau}_2)^2 + V_1 e^{-(r/\lambda_r)^2} (1 - e^{-\eta_1 \rho}) \end{aligned} \tag{2.25}$$

where $\rho \equiv \rho_n + \rho_p$. The first term $V_{\rm TNA}$ gives the attractive force and the second term $V_{\rm TNR}$ gives the repulsive force. In [64], λ_a , λ_r and η_1 are fixed at 2.00fm, 1.40fm and 0.15fm^3.

Table 2.1: Partial wave contributions to Λ single particle potential $U_\Lambda(k_\Lambda = 0)$ at $k_F = 1.35\text{fm}^{-1}$ in the various models (MeV) [56, 61].

	$U_\Lambda(S)$	$U_\Lambda(^1S_0)$	$U_\Lambda(^3S_1)$	$U_\Lambda(P)$	U_Λ
ND	-32.5	-7.4	-25.1	-8.0	-40.5
NF	-30.5	-10.0	-20.7	-0.9	-31.6
NSC97a	-34.5	-3.8	-30.7	0.6	-33.9
NSC97b	-35.5	-5.5	-30.0	1.4	-34.1
NSC97c	-37.5	-7.8	-29.7	2.1	-35.3
NSC97d	-38.7	-11.0	-27.7	3.5	-35.1
NSC97e	-38.8	-12.8	-26.0	4.5	-34.3
NSC97f	-37.3	-14.4	-22.9	6.2	-37.4

The other three parameters are determined to reproduce the saturation properties such as the saturation density and the binding energy for the symmetric nuclear matter and the nuclear incompressibility. The TBF three body potential $V_{\rm TBF}$ is

$$\begin{aligned}(V_{\rm TBF})_{ijk} &= V_{ijk}^{2\pi} + V_{ijk}^{R} \\ &= A\sum_{\rm cyc}\left(\{X_{ij},X_{jk}\}\{\boldsymbol{\tau}_i\cdot\boldsymbol{\tau}_j,\boldsymbol{\tau}_j\cdot\boldsymbol{\tau}_k\}+\frac{1}{4}[X_{ij},X_{jk}][\boldsymbol{\tau}_i\cdot\boldsymbol{\tau}_j,\boldsymbol{\tau}_j\cdot\boldsymbol{\tau}_k]\right) \\ &\quad +U\sum_{\rm cyc}T^2(r_{ij})T^2(r_{jk}) \end{aligned} \tag{2.26}$$

where

$$X_{ij} = Y(r_{ij})\boldsymbol{\sigma}_i\cdot\boldsymbol{\sigma}_j + T(r_{ij})S_{ij}. \tag{2.27}$$

Here $Y(r)$ is the Yukawa function, which is defined by $Y(r)\equiv\frac{e^{-r}}{r}$ and $T(r)$ is the tensor function, $T(r)\equiv\left(1+\frac{1}{r}+\frac{1}{r^2}\right)\frac{e^{-r}}{r}$. Parameters A and U are fitted to reproduce the saturation density and the binding energy for the symmetric nuclear matter.

2.2 Models for Hadronic EOS

In this subsecton, we review briefly the hadronic EOSs obtained by combining the baryon-baryon interactions and the nuclear many-body methods.

APR EOS from variational method [65]

In constructing the standard APR EOS, one uses the AV18 two body nuclear force and Urbana IX type phenomenological three body force with the relativistic boost correction. The Hamiltonian $\mathcal{H}_{\rm APR}$ is

$$\mathcal{H}_{\rm APR} = \mathcal{H}_0 + \sum(V^*_{AV18})_{ij} + \sum(V^*_{\rm TBF})_{ijk}. \tag{2.28}$$

Here $\mathcal{H}_0$ is the free part, and $*$ denotes that the relativistic corrections are included in the forms of the 2-body and 3-body forces. The variational wave function Ψ for hadronic matter at zero temperature is written as

$$\Psi = {\rm Sym}\left[\prod_{i<j}f_{ij}\right]\Phi \tag{2.29}$$

where Φ is the Fermi-gas wave function, Sym is a symmetrizer, and f_{ij} is the Jastrow type correlation function,

$$f_{ij} = \sum_{T=0,1}\sum_{S=0,1}\left[f_c(r_{ij})(1)_{ijTS} + f_{12}(r_{ij})(S_{ij})_{ijTS} + f_{LS}(r_{ij})(\boldsymbol{L}\cdot\boldsymbol{S})_{ijTS}\right]. \tag{2.30}$$

Here S is the total spin, T is the total isospin and i, j are the proton or neutron. The variational parameters, f_c, f_{12} and f_{LS} are determined by minimizing the total energy,

$$E_{\rm tot}[f] = \frac{\langle\Psi|\,\mathcal{H}_{\rm APR}\,|\Psi\rangle}{\langle\Psi|\Psi\rangle}. \tag{2.31}$$

EOS from Bethe-Brueckner-Goldstone (BBG) Theory [66, 67, 68]

Suppose we have only 2-body forces. Then the total Hamiltonian Hamiltonian $\mathcal{H}$ with the free Hamiltonian $\mathcal{H}_0$ reads

$$\mathcal{H} = \mathcal{H}_0 + \mathcal{H}_1 \equiv \sum_k \frac{\hbar^2\boldsymbol{k}^2}{2m} + \frac{1}{2}\sum_{\{k_i\}} \langle k_1 k_2|\, v\,|k_3 k_4\rangle\, a^\dagger_{k1} a^\dagger_{k2} a_{k3} a_{k4}. \tag{2.32}$$

From Gell-Mann and Low theorem[69], under the assumption of an adiabatic evolution of the system, the ground state of $\mathcal{H}$ and $\mathcal{H}_0$, $|\psi_0\rangle$ and $|\phi_0\rangle \equiv \prod_{|\boldsymbol{k}|<k_F} a^\dagger_{\boldsymbol{k}}\,|0\rangle$ satisfying $\mathcal{H}_0\,|\phi_0\rangle = E_0\,|\phi_0\rangle$ respectively, have the following relation:

$$|\psi_0\rangle = \lim_{\varepsilon\to 0} \frac{U^{(\varepsilon)}(-\infty)\,|\phi_0\rangle}{\langle\phi_0|\,U^{(\varepsilon)}(-\infty)\,|\phi_0\rangle}. \tag{2.33}$$

Here

$$\begin{aligned} U^{(\varepsilon)}(-\infty) &= 1 - \frac{i}{\hbar}\int_{-\infty}^0 \mathcal{H}_I(t_1)dt_1 + \left(-\frac{i}{\hbar}\right)^2 \int_{-\infty}^0 \mathcal{H}_I(t_2)dt_2 \int_{-\infty}^{t_2} \mathcal{H}_I(t_1)dt_1 + \dots \\ &= 1 + \sum_{n=1}^\infty \left(-\frac{i}{\hbar}\right)^n \frac{1}{n!}\int_{-\infty}^0 dt_n \dots \int_{-\infty}^0 dt_1 T[\mathcal{H}_I(t_n)\dots\mathcal{H}_I(t_1)], \end{aligned} \tag{2.34}$$

$$\mathcal{H}_I(t) = e^{i\mathcal{H}_0 t/\hbar} e^{-\varepsilon|t|} \mathcal{H}_1 e^{-i\mathcal{H}_0 t/\hbar}. \tag{2.35}$$

As a result, the energy difference ΔE by adding the interaction $\mathcal{H}_1$ can be written as

$$\Delta E = \lim_{\varepsilon\to 0} \frac{\langle\phi_0|\,\mathcal{H}_1 U^\varepsilon(-\infty)\,|\phi_0\rangle}{\langle\phi_0|\,U^\varepsilon(-\infty)\,|\phi_0\rangle} \tag{2.36}$$

$$= \lim_{\varepsilon\to 0} \langle\phi_0|\,\mathcal{H}_1 U^\varepsilon(-\infty)\,|\phi_0\rangle_{\rm CL} \tag{2.37}$$

where the subscript CL denotes the connected diagrams. Thus we obtain

$$\begin{aligned} \Delta E &= \lim_{\varepsilon\to 0} \langle\phi_0|\,\mathcal{H}_1 \left(1 + \sum_{n=1}^\infty \prod_{m=1}^n \left(\frac{1}{E_0 - \mathcal{H}_0 - im\varepsilon}\mathcal{H}_1\right)\right)|\phi_0\rangle_{\rm CL} \\ &= \lim_{\eta\to 0} \langle\phi_0|\,\mathcal{H}_1 \sum_{n=0}^\infty \left(\frac{1}{E_0 - \mathcal{H}_0 - i\eta}\mathcal{H}_1\right)^n |\phi_0\rangle_{\rm CL}\,. \end{aligned} \tag{2.38}$$

In the BBG theory, ΔE is expanded in terms of the number of hole lines in the diagrammatic representation of the perturbative series, which physically corresponds the low density

expansion. For example, we show the typical diagrams for 2-hole line expansion in Fig. 2.2 (a) and (b). However, there are infinite number of diagrams at the level of the 2-hole line expansion as shown in Fig. 2.2 (c). As a tool to include them all together, the two-body scattering matrix G is introduced:

$$\begin{aligned}\langle k_1, k_2|\, G(\omega)\, |k_3, k_4\rangle &= \langle k_1, k_2|\, v\, |k_3, k_4\rangle + \sum_{k_3', k_4'} \langle k_1, k_2|\, v\, |k_3', k_4'\rangle \\ &\times \frac{(1-\theta_F(k_3'))(1-\theta_F(k_4'))}{\omega - e_{k_3'} - e_{k_4'}} \langle k_3', k_4'|\, G(\omega)\, |k_3, k_4\rangle\,. \end{aligned} \tag{2.39}$$

Here, ω is the initial energy and the intermediate states, $|k_3', k_4'\rangle$, are restricted to those above the Fermi sea (the particle states), which is clearly shown explicitly by the factor $(1-\theta_F(k_3'))(1-\theta_F(k_4'))$ with

$$\theta_F(k_3') \equiv \begin{cases} 1 & (|\boldsymbol{k}| < k_F) \\ 0 & (|\boldsymbol{k}| > k_F). \end{cases} \tag{2.40}$$

Now ΔE_2, which is ΔE up to the 2-hole line expansion, can be written as

$$\Delta E_2 = \frac{1}{2} \sum_{k_1, k_2 < k_F} \langle k_1 k_2|\, G(\omega)\, |k_1 k_2\rangle_A \tag{2.41}$$

where the subscript A denotes the anti-symmetrization.

Instead of Eq. (2.32), one may introduce a decomposition with an arbitrary single-particle potential (or the self-energy) U:

$$\mathcal{H} = (\mathcal{H}_0 + U) + (\mathcal{H}_1 - U) = \mathcal{H}_0' + \mathcal{H}_1'. \tag{2.42}$$

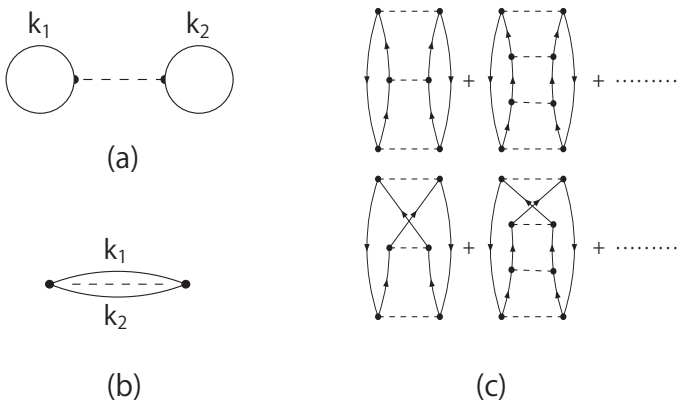

Figure 2.2: (a,b) The typical diagrams for 2-hole line expansion. (a) is the Hartree term and (b) is the Fock term. (c) The diagrams contributing at the same time in the 2-hole line expansion [70].

With the new interaction term $\mathcal{H}'_1$, we can construct the U-dependent G-matrix. The choice of U motivated by the Hartree-Fock approximation reads

$$U(k) = \sum_{k'<k_F} \langle kk'| G(\omega) |kk'\rangle_A . \tag{2.43}$$

This is called as the continuous choice. On the other hand, in the gap choice, Eq. (2.43) is adopted only for $k < k_F$ and otherwise $U = 0$.

EOS from Chiral $SU(3)$ Relativistic Mean Field Model [71]

The chiral $SU(3)$ Lagrangian $\mathcal{L}_{\rm SCL}$ describing the baryons and σ and ζ scalar mesons and ω, ρ^0 and ϕ vector mesons is written as

$$\begin{aligned}\mathcal{L}_{\rm SCL} = \quad & \sum_i \bar{q}_i[i\gamma_\mu\partial^\mu - M_i^* - \gamma_\mu U_i^\mu]q_i + \frac{1}{2}\partial_\mu\psi_\sigma\partial^\mu\psi_\sigma - \frac{1}{2}m_\sigma^2\psi_\sigma^2 + \frac{1}{2}\partial_\mu\psi_\zeta\partial^\mu\psi_\zeta - \frac{1}{2}m_\zeta^2\psi_\zeta^2 \\ & -\frac{1}{4}W_{\mu\nu}W^{\mu\nu} + \frac{1}{2}m_\omega^2\omega_\mu\omega^\mu + \frac{1}{4}c_\omega(\omega_\mu\omega^\mu)^2 \\ & -\frac{1}{4}R_{\mu\nu}R^{\mu\nu} + \frac{1}{2}m_\rho^2\rho_\mu\rho^\mu - \frac{1}{4}\Phi_{\mu\nu}\Phi^{\mu\nu} + \frac{1}{2}m_\phi^2\phi_\mu\phi^\mu \\ & -\frac{1}{4}F_{\mu\nu}F^{\mu\nu} - V_{\sigma\zeta}(\psi_\sigma, \psi_\zeta).\end{aligned} \tag{2.44}$$

Here, q_i represents the $SU(3)$ baryon field, σ, ω^μ, ρ^μ and ϕ^μ are the σ, ω, ρ^0 and ϕ meson fields respectively,

$$M_i^* = M_i - g_{\sigma i}\psi_\sigma - g_{\zeta i}\psi_\zeta, \tag{2.45}$$

$$U_i^\mu = g_{\omega i}\omega^\mu + g_{\rho i}\rho^\mu + \frac{1+\lambda_3}{2}eA^\mu, \tag{2.46}$$

$$\psi_\sigma = f_\pi - \sigma, \quad \psi_\zeta = f_\zeta - \zeta, \tag{2.47}$$

$W^{\mu\nu}$, $R^{\mu\nu}$ and $\Phi^{\mu\nu}$ are the field strength tensors for ω, ρ^0 and ϕ mesons and g_{mB} is the coupling constant between meson m and baryon B. $g_{\phi N}$ is ignored since the suppression of this coupling is predicted by the Okubo-Zweig-Iizuka rule [72, 73, 74]. c_ω is the coupling constant between ω mesons. $V_{\sigma\zeta}$ is a logarithmic potential, which can be obtained from the staggered fermion action with the chiral limit and the strong coupling limit. The explicit form of $V_{\sigma\zeta}$ is given by

$$V_{\sigma\zeta} = -a\left\{2f_{\rm SCL}\left(\frac{\psi_\sigma}{f_\pi}\right) + f_{\rm SCL}\left(\frac{\psi_\zeta}{f_\zeta}\right)\right\} + \xi_{\sigma\zeta}\psi_\sigma\psi_\zeta \tag{2.48}$$

where $f_{\rm SCL}(x) \equiv \log(1-x) + x + \frac{x^2}{2}$. The parameters except m_σ, $g_{\omega N}$, g_{ρ_N}, c_ω and the coupling constants between hyperons and mesons are determined to reproduce the masses of π, K and ζ mesons and the vacuum condensates of σ and ζ mesons. Parameters, $g_{\omega N}$ and c_ω, are determined

to reproduce the saturation density and the binding energy of the nuclear matter at a given m_σ. Then, m_σ and $g_{\rho N}$ are fitted to reproduce the binding energy of Sn and Pb isotopes. The coupling constants between hyperons and vector mesons are determined under the flavor $SU(3)$ symmetry as we have already discussed in the previous section. Finally, we determine $g_{\sigma\Lambda}$ and $g_{\zeta\Lambda}$ to reproduce the separation energy of Λ of ^{13}C and ^{12}C and $\Lambda\Lambda$ binding energy.

Summary of Hadronic EOSs (H-EOSs) to be employed in this thesis

- APR EOS [65]: APR EOS is obtained by the variational method by AV18 potential and the three-body force of Urbana-type with the relativistic boost correction. APR EOS does not include hyperons. Phenomenological parameters in three body force are determined to reproduce the saturation properties.

- TNI2, TNI3, TNI2u and TNI3u [31, 75]: TNI2 and TNI3 are obtained by the G-matrix calculation with Reid soft-core potential for NN and Nijmegen type-D hard-core potential for YN and YY. Also, a phenomenological TNI type three-body force [63] is introduced in a form of effective NN force to reproduce the saturation point of symmetric nuclear matter with the incompressibility κ=250MeV (TNI2) and κ=300MeV (TNI3). For TNI2u and TNI3u, the three-body interaction is introduced *universally* in a form of effective NN, NY and YY forces.

- AV18+TBF and Paris+TBF [76]: They are obtained by the G-matrix calculation but with different choice of potentials, AV18 and Paris potentials for NN and Nijmegen soft-core potential for YN and YY. Also, the three-body force of Urbana-type is introduced in a form of effective NN force to meet the saturation condition.

- SCL3$\Lambda\Sigma$ [71]: It is based on RMF model with chiral SU(3) symmetry and logarithmic potential motivated by the strong coupling lattice QCD approach. Phenomenological parameters of the model are determined to reproduce the saturation condition, bulk properties of normal nuclei and separation energies of single- and double-Λ hypernuclei.

In Fig.2.3(a), we plot the hadronic EOSs with hyperons (TNI2u, TNI2, TNI3u, TNI3, AV18+TBF+$\Lambda\Sigma$ and SCL3$\Lambda\Sigma$) together with APR. Filled circles on each line denote the density where the hyperon-mixing starts to occur. One can see that (i) the mixture of hyperons softens the equation of state relative to APR, and (ii) onset of the hyperon-mixing is shifted to higher density if we consider the three-body interaction in the hyperon sector.

2.3 Hyperon Puzzle

Let us consider what would be the NS structure under the hadronic EOS with and without hyperons . Although there exist large uncertainties for the two-body Y-N interactions, various

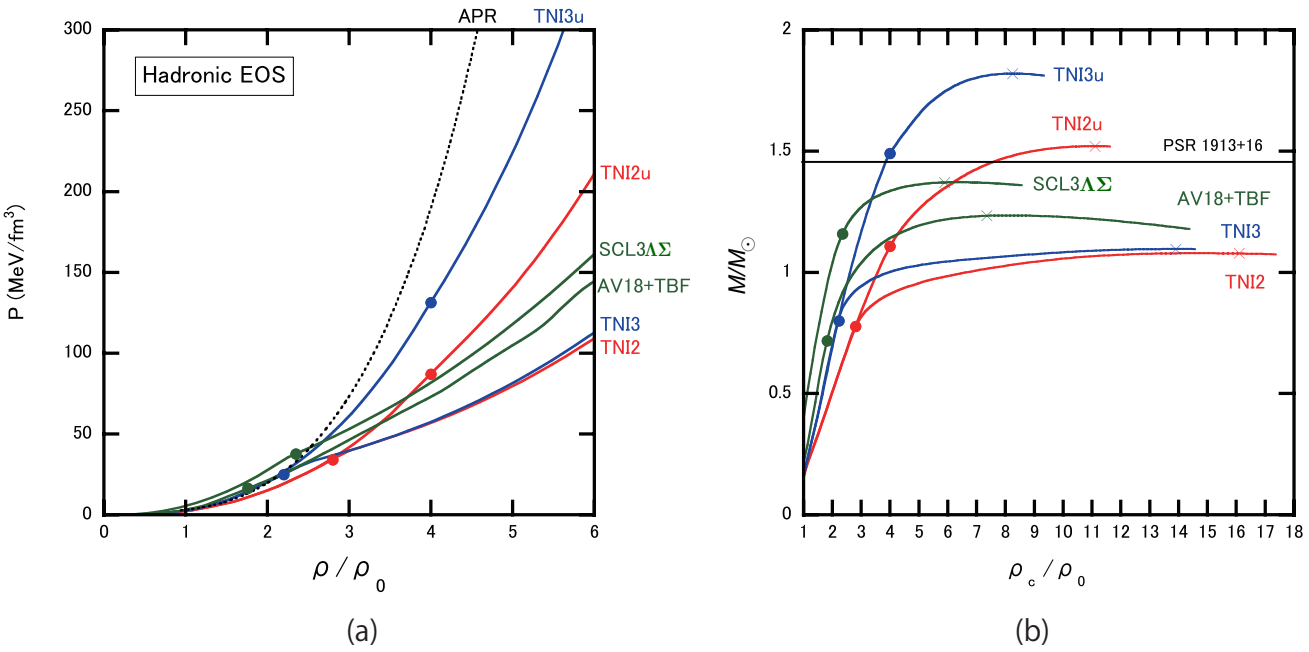

Figure 2.3: (a) The hadronic equation of states with and without the hyperon mixing. The black line denotes the EOS without hyperon, APR (AV18+δV+UIX*). The red lines correspond to the EOS with hyperons; TNI2 (only three-nucleon force with $\kappa = 250$MeV) and TNI2u (universal three-baryon force with $\kappa = 250$MeV). The blue lines correspond to TNI3 (only three-nucleon force with $\kappa = 300$MeV) and TNI3u (universal three-baryon force with $\kappa = 300$MeV). The green line corresponds to AV18+TBF+$\Lambda\Sigma$ (G-matrix with AV18 + 3-nucleon force + hyperons), and SCL3$\Lambda\Sigma$ (relativistic mean-field model with chiral $SU(3)$ symmetry). (b) $M-\rho$ relations for seven EOSs considered in (a). In both figures, filled circles on each line show the density where the hyperons start to mix. The cross points are the densities where the maximum mass is obtained. The solid horizontal line shows $M = 1.44M_\odot$ corresponding to PSR 1913+16. Those figures are adopted from [1, 2].

different models suggest that hyperons may appear at densities of several times ρ_0 as shown in Fig.2.3(a). Those hyperons introduce significant softening of EOS and even the well-established $1.4M_\odot$ NSs may not be reproduced if we do not include the repulsive three body force among hyperons at high densities (see the reviews, [24, 77] and the references therein). The three-body force in the hyperon sector originally suggested in [31] may or may not describe the $2M_\odot$ NSs depending on its strength [24, 78, 79, 80, 81]. This is called the "Hyperon Puzzle". In Fig.2.3(b), the M-ρ relations with these EOSs are plotted by the same color lines. The solid horizontal line shows $M = 1.44M_\odot$ corresponding to PSR 1913+16. The cross points correspond to the maximum mass. As we have already mentioned, if the three body force in hyperon sector is not included (TNI2, TNI3, AV18+TBF+$\Lambda\Sigma$ and SCL3$\Lambda\Sigma$), the canonical NSs with $1.44M_\odot$ cannot be sustained due to the hyperon mixture. The universal three body force certainly makes EOS

Table 2.2: Properties of various hadronic EOSs with hyperons; TNI2, TNI3, TNI2u, TNI3u [31, 75], Paris+TBF, AV18+TBF [76, 82, 83] and SCL3ΛΣ [71]. κ is the nuclear incompressibility and $\rho_{\rm th}$ is the threshold density of hyperon-mixing with ρ_0 (=0.17/fm^3) being the normal nuclear density. R and ρ_c denote the radius and central density for the maximum mass ($M_{\rm max}$) NS, respectively. The numbers in the parentheses are those without hyperons. $*$s indicate that the numbers are read from the figures in [76].

EOS	TNI2	TNI3	TNI2u	TNI3u	Paris+TBF	AV18+TBF	SCL3ΛΣ
κ (MeV)	250	300	250	300	281	192	211
$\rho_{\rm th}(\Lambda)/\rho_0$	2.95	2.45	4.01	4.01	2.9*	2.8*	2.24
$\rho_{\rm th}(\Sigma^-)/\rho_0$	2.83	2.23	4.06	4.01	1.9*	1.8*	2.24
$M_{\rm max}/M_\odot$	1.08	1.10	1.52	1.83	1.26	1.22	1.36
	(1.62)	(1.88)			(2.06)	(2.00)	(1.65)
R(km)	7.70	8.28	8.43	9.55	10.46	10.46	11.42
	(8.64)	(9.46)			(10.50)	(10.54)	(10.79)
ρ_c/ρ_0	16.10	13.90	11.06	8.26	7.35	7.35	6.09
	(9.97)	(8.29)			(6.47)	(6.53)	(6.85)

stiff. However, it is still not enough to sustain $2M_\odot$ NSs.

In Table 2.2, we show the nuclear incompressibility κ defined by $\kappa \equiv 9\left.\frac{d^2\hat{E}}{d\rho^2}\right|_{\rho=\rho_0}$, the threshold densities of hyperon-mixing, $\rho_{\rm th}(\Lambda)$ and $\rho_{\rm th}(\Sigma^-)$, for each H-EOS. In the same table, we show the maximum-mass $M_{\rm max}$, the radius R and the central density $\rho_{\rm c}$ of the NS obtained from each H-EOS. The values obtained by switching off the Y-mixing are given in the parentheses for comparison. For the H-EOSs without universal three-body repulsion, significant softening due to Y-mixing reduces $M_{\rm max}$, i.e., $M_{\rm max}$ (without Y)=$(1.62-2.00)\rightarrow$ $M_{\rm max}$ (with Y)=$(1.08-1.26)$. This clearly contradicts the observed mass $M_{\rm obs}=1.44M_\odot$ for PSR1913+16. On the other hand, H-EOSs with universal three-body repulsion (TNI2u, TNI3u), $M_{\rm max}$ is recovered nearly to that without Y. The radius of NSs with SCL3ΛΣ becomes large since EOS obtained by RMF becomes stiff at low densities as shown in Fig. 2.3(a).

The use of several kinds of EOS mentioned above, from different theoretical methods (G-matrix, RMF), with various stiffness ranging from $\kappa\sim 190$ MeV to 300 MeV and with the variation of $\rho_{\rm th}(Y)\simeq(2-4)\rho_0$, is expected to cover the present uncertainties of the H-EOSs.

2.4 Brief Summary

In this chapter, we have introduced examples of the phenomenological 2-body and 3-body baryon potentials with and without hyperons. Also, we have summarized the hadronic EOSs obtained by the several many-body approaches (the variational method, the Bethe-Brueckner-Goldstone approach and the relativistic mean field theory). Then, by solving the TOV equation,

we have shown that (i) the maximum mass of the NSs is substantially reduced by the hyperon mixture, and (ii) $2M_\odot$ NS cannot be sustained even if we introduced universal 3-body repulsion among baryons. We call this as the "hyperon puzzle", a serious conflict between the astrophysical observation and the nuclear theory.

Chapter 3

The Quark Phase

In this chapter, we introduce quark EOS (Q-EOS) to be used in the high density region. Two important condensations in Quantum Chromo Dynamics (QCD), the chiral and the diquark condensations, are considered. Q-EOS in NSs cannot be described by the dynamics of free fermions since the quark matter is still strongly interacting at the density relevant to the NS interior. In this thesis, we employ the $(2+1)$-flavor Nambu-Jona-Lasinio (NJL) model, which captures the essential properties of QCD such as the dynamical breaking of chiral symmetry and its restoration at finite T and μ.

3.1 $\bar{q}q$ Correlation

Let us define the chiral invariant part of the QCD Lagrangian, $\mathcal{L}_{\rm chiral}$, as

$$\mathcal{L}_{\rm QCD} \equiv \mathcal{L}_{\rm chiral} - \bar{q}^f_\alpha m_f \delta^{\alpha\beta} q^f_\beta \tag{3.1}$$

where $\mathcal{L}_{\rm QCD}$ is given in Eq. (1.1). We consider 3-flavor QCD from now on. The quark field q can be divided into two parts by using the eigenstates of γ_5.

$$q = q_R + q_L,$$

$$q_{R/L} = \frac{1 \pm \gamma_5}{2} q \equiv P_{R/L} q. \tag{3.2}$$

$\mathcal{L}_{\rm chiral}$ is invariant under the $SU(3)_R \times SU(3)_L$ chiral rotations;

$$q_{R/L} \to q_{R/L} = e^{i\theta^a_{R/L}\lambda_a/2} q_{R/L} \tag{3.3}$$

where θ^a_R and θ^a_L are space-time independent parameters and λ_a are generators for the flavor space. The conserved current $j^{a\mu}_{R/L}$ and the conserved charge $Q^a_{R/L}$ for this global symmetry are

$$j^{a\mu}_{R/L} = \bar{q}_{R/L}\gamma^\mu \frac{\lambda^a}{2} q_{R/L}, \tag{3.4}$$

$$Q^a_{R/L} = \int d^3x j^{a0}_{R/L}. \tag{3.5}$$

From these $j^{a\mu}_{R/L}$, we define the vector current $j^{a\mu}_V$ and the axial vector current $j^{a\mu}_A$ as follows.

$$j^{a\mu}_V \equiv j^{a\mu}_R + j^{a\mu}_L, \tag{3.6}$$
$$j^{a\mu}_A \equiv j^{a\mu}_R - j^{a\mu}_L. \tag{3.7}$$

We can also define the conserved current for vector and axial vector current as $Q^a_{V/A} \equiv \int d^3x j^{a0}_{V/A}$ respectively. By considering the commutation relations between the conserved charges for the vector and the axial vector currents and the Hamiltonian H, the angular momentum operator J and the parity operator P

$$[Q^a_{V/A}, H] = [Q^a_{V/A}, J] = 0, \tag{3.8}$$
$$PQ^a_V P^{-1} = Q^a_V, \tag{3.9}$$
$$PQ^a_A P^{-1} = -Q^a_A, \tag{3.10}$$

the hadronic states can be characterized by the mass m, the angular momentum j and parity p. Therefore, the hadronic states $|m, j, p\rangle$ and $Q^a_A |m, j, p\rangle$ have the same energy, the same angular momentum and different parities. If the chiral symmetry is preserved in the QCD vacuum, there must be the degenerate states, which have the same energy, the same angular momentum and different parities. However, these degenerate states do not appear in the hadronic spectrum. To solve this confliction, the concept "the spontaneous symmetry breaking" was introduced. From the Nambu-Goldstone theorem [84, 85] , the pseudo scalar mesons π, K, η are considered as NG bosons for

$$SU_L(3) \times SU_R(3) \to SU_{L+R}(3) \tag{3.11}$$

from their quantum numbers. The pion mass comes from the explicit symmetry breaking due to the current mass term. In this case, the scalar field $\bar{q}q$ satisfying

$$[iQ^a_5, \bar{q} i\gamma_5 \lambda^b q] = \frac{1}{2}\bar{q}\{\lambda^a, \lambda^b\}q = \delta^{ab}\bar{q}q \tag{3.12}$$

is called as the chiral condensation. In fact, from Gell-Mann-Oakes-Renner relation [86],

$$f^2_\pi m^2_{\pi^\pm} = -m\langle \bar{u}u + \bar{d}d\rangle + \mathcal{O}(m^2_{u,d}), \quad m \equiv (m_u + m_d)/2 \tag{3.13}$$

where f_π is the pion decay constant , we find that the QCD vacuum has strong chiral condensates due to strong $\bar{q}q$ correlation;

$$\langle \bar{u}u\rangle \sim \langle \bar{d}d\rangle = (-(270 - 293)\mathrm{MeV})^3 \tag{3.14}$$

in the case of $m = (3.5^{+0.7}_{-0.2})$MeV at the renormalization scale of 2 GeV [7].

3.2 qq Correlation

To illustrate the fact that QCD has not only the strong $\bar{q}q$ correlation but also a strong qq correlation, let us consider the effective 4-fermi interaction induced by the one-gluon exchange (OGE):

$$\mathcal{L}_{\rm OGE} = -G_{\rm OGE}(p^2)\left(q\gamma^\mu\frac{\tau_a}{2}q\right)^2 \tag{3.15}$$

where $G_{\rm OGE}(p^2) > 0$ is the momentum-dependent effective coupling and τ_a are the $SU(3)_C$ generators. From the Fierz transformation (see Appendix C), we can rewrite the color part of the interaction as

$$(\tau_a)^{ij}(\tau_a)^{kl} = -\frac{N_c+1}{N_c}(\tau_A)^{ik}(\tau_A)^{lj} + \frac{N_c-1}{N_c}(\tau_S)^{ik}(\tau_S)^{lj} \tag{3.16}$$

where N_c is the number of colors and $\tau_{A/S}$ are antisymmetric / symmetric $SU(3)_C$ generators. As we can see clearly, the color-antisymmetric channel is attractive from the sign of $(\tau_A)(\tau_A)$ term. Therefore, it leads to a strong diquark correlation inside hadrons at low density and also the color superconductivity (CSC) at high baryon density by the condensation of diquarks [87]. Since we treat the CSC phase in NSs in later sections, let us explain the two phases of CSC, 2-flavor colorsuperconducting (2SC) phase and color flavor locked (CFL) phase.

Ginzburg−Landau Potential for CSC

Let us consider the following diquark condensation, $\langle q^T\mathcal{O}q\rangle$. Because the Pauli principle,

$$q^T\mathcal{O}q = \mathcal{O}_{ij}q_iq_j = -\mathcal{O}_{ij}q_jq_i = -q^T\mathcal{O}^Tq \tag{3.17}$$

must be satisfied, $\mathcal{O}$ should be an antisymmetric operator satisfying $\mathcal{O}^T = -\mathcal{O}$. If we consider the ${}^1S_0$ pairing, this pairing should be the flavor antisymmetric since the condensate is already color antisymmetric from Eq. (3.15) and Eq. (3.16). In the color and flavor antisymmetric channel, the order parameter of the condensate $\Psi \in \bar{\mathbf{3}}_C \otimes \bar{\mathbf{3}}_F$ transforms

$$\Psi \to g_C\Psi g_F \tag{3.18}$$

where $g_{C/F} \in SU(3)_{C/F}$. Then, the Ginzburg-Landau (GL) effective potential V invariant under the color and flavor rotations reads

$$V = -a^2{\rm tr}(\Psi^\dagger\Psi) + \lambda_1[{\rm tr}(\Psi^\dagger\Psi)]^2 + \lambda_2{\rm tr}[(\Psi^\dagger\Psi)^2]. \tag{3.19}$$

By the stability analysis of the potential [88, 89, 90], if $\lambda_2 < 0$ and $\lambda_1 + \lambda_2 > 0$ are satisfied, the ground state is given by

$$\Psi = \begin{pmatrix}\Delta & 0 & 0\\ 0 & 0 & 0\\ 0 & 0 & 0\end{pmatrix}. \tag{3.20}$$

This state is called as 2-flavor superconducting (2SC) phase. In 2SC phase, a red (green) u quark and a green (red) d quark make a condensate. On the other hand, in the case of $\lambda_2 > 0$ and $3\lambda_1 + \lambda_2 > 0$,

$$\Psi = \begin{pmatrix} \Delta & 0 & 0 \\ 0 & \Delta & 0 \\ 0 & 0 & \Delta \end{pmatrix} \tag{3.21}$$

becomes the ground state. This state is called as color flavor locked (CFL) phase.

2-Flavor Superconducting Phase [87]

If the strange quark mass M_s is relatively large compared with the quark chemical potential μ, the Fermi momentum of u and d quarks becomes much larger than that of s quark. Therefore, only the condensate between u and d quarks appears. The order parameter of 2SC phase $\Psi_{\rm 2SC}$ can be written as

$$\Psi_{\rm 2SC} \equiv \varepsilon^{\alpha\beta 3}\varepsilon_{ij3}\langle (q^T)^i_\alpha C\gamma_5 q^j_\beta\rangle = \varepsilon^{\alpha\beta 3}\varepsilon_{ij3}\Delta_{\rm 2SC}. \tag{3.22}$$

Here, $C = i\gamma_2\gamma_0$ is the charge conjugation matrix[1]. Symmetry breaking pattern of 2SC phase is

$$SU(3)_c \times SU(3)_L \times SU(3)_R \times U(1)_B \to SU(2)_C \times SU(2)_L \times SU(2)_R \times U(1)_{\bar{B}}. \tag{3.23}$$

Here $U(1)_{\bar{B}}$ is the combination of the $U(1)_B$ and $U(1)_8 \in SU(3)_c$. 2SC phase is not superfluid phase but superconducting phase since the global $U(1)_{\bar{B}}$ survives.

Color Flavor Locked Phase [91]

At very high density at which the mass of strange quarks M_s becomes much smaller than the quark chemical potential, the CFL phase is expected to be realized. The order parameter of CFL phase $\Psi_{\rm CFL}$ is

$$\Psi_{\rm CFL} \equiv \varepsilon^{\alpha\beta\gamma}\varepsilon_{ijk}\langle (q^T)^j_\beta C\gamma_5 q^k_\gamma\rangle = \delta^\alpha_i \Delta_{\rm CFL}. \tag{3.24}$$

As the name shows, in the CFL phase, the simultaneous rotation for color and flavor space is invariant. In this phase, the symmetry breaking pattern is

$$SU(3)_C \times SU(3)_L \times SU(3)_R \times U(1)_B \to SU(3)_{C+L+R}. \tag{3.25}$$

In CFL phase, u, d and s quarks contribute the paring equally. This symmetry breaking pattern is very similar with the symmetry breaking pattern for ^{3}He-B phase, in which the simultaneous rotation for orbital angular momentum and spin space is invariant. CFL phase is both superfluid and superconducting since local $SU(3)_C$ and global $U(1)_B$ are completely broken.

[1]Due to this operator C, the condensate with the positive parity state is selected. An analysis of the instanton induced interaction suggests that the positive parity state is realized in the ground state.

3.3 Chiral Anomaly

Classically, $\mathcal{L}_{\rm chiral}$ is invariant under the $U(1)_V$ and $U(1)_A$ transformation. However, due to the quantum effect, the axial vector current j_A^μ is not conserved even for massless quark [92]

$$\partial_\mu j_A^\mu = -\frac{N_f g^2}{32\pi^2}\varepsilon^{\mu\nu\rho\sigma}F_{\mu\nu}F_{\rho\sigma}. \tag{3.26}$$

This explicit breaking of $U(1)_A$ symmetry explains the reason why the η' mass is much heavier than other pseudo-scalar mesons. An effective 6 quark interaction which preserves $SU(3)_L \times SU(3)_R$ but breaks $U(1)_A$ was introduced by Kobayashi, Maskawa [93] and later by 'tHooft [94]:

$$\mathcal{L}_{\rm KMT} = -G_{_D}(p^2)\det\left(\bar{q}(1+\gamma_5)q\right) + \text{h.c.}. \tag{3.27}$$

Here, $G_{_D}(p^2) > 0$ and the determinant is taken for the flavor space. The Fierz transformation of Eq. (3.27) has a structure,

$$\sum_{i,j,k=1,2,3}[(q\tilde{\lambda}_i\tilde{\tau}_k(1+\gamma_5)C\bar{q}^T)(\bar{q}\tilde{\lambda}_j\tilde{\tau}_k(1+\gamma_5)Cq)(\bar{q}_i(1+\gamma_5)q_j) + \text{h.c.}] \tag{3.28}$$

where $\tilde{\lambda}_{1,2,3} \equiv \lambda_{7,5,2}$ and $\tilde{\tau}_{1,2,3} \equiv \tau_{7,5,2}$ and λ_i (τ_i) are the $SU(3)$ generators for flavor (color) space. From Eq. (3.27) and Eq. (3.28), we can see $U(1)_A$ anomaly contributes both to the $\bar{q}q$ and qq correlations.

3.4 $(2+1)$-flavor Nambu-Jona-Lasinio (NJL) Model

In this section, we consider EOS in the high density region. One way to describe EOS at high densities is the perturbative treatment of QCD (pQCD). Due to the asymptotic freedom, at extremely high energy scale, we can treat QCD EOS perturbatively. At present, QCD EOS is calculated up to $\mathcal{O}(g^4)$ [95]. Fig. 3.1 shows the pressure of massless 3-flavor QCD matter as a function of the quark chemical potential μ. Light (dark) shaded area corresponds to the pressure from the renormalization scale between $\Lambda = \mu$ and $\Lambda = 4\mu$ up to $\mathcal{O}(g^2)$ ($\mathcal{O}(g^4)$) and $P_0(\mu)$ is the pressure without interactions. Up to the energy scale $\mu \sim (1-2)$GeV, the results strongly depend on the renormalization scale as shown in Fig. 3.1. Therefore, we cannot trust the result of pQCD calculation in the region below $\mu \sim 1$GeV.

The baryon density at the central core of the NSs would be at most $10\rho_0$. Even for such a high density, the chemical potential of the quarks are about $(400-500)$MeV which is not large enough for pQCD to be reliable. Namely, the deconfined quarks inside the NSs, even if they exist, would be still strongly interacting.

Since the lattice QCD Monte Carlo simulation is unfortunately not possible due to the notorious sign problem at present, we adopt an effective theory of QCD, the $(2+1)$-flavor

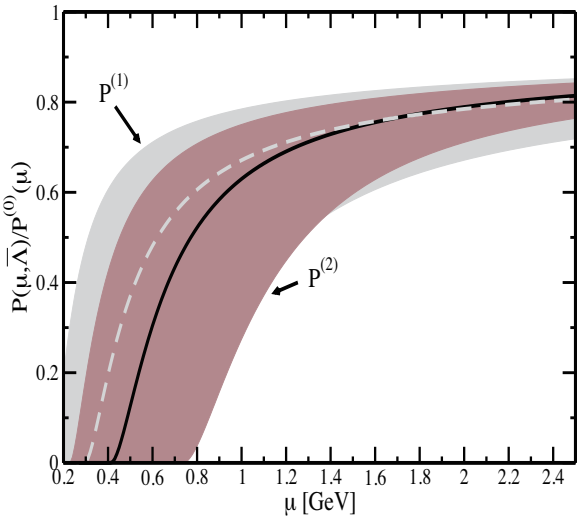

Figure 3.1: Pressure (P) of massless 3 flavor QCD matter as a function of the quark chemical potential μ. Light (dark) shaded area corresponds to the pressure from the renormalization scale from $\Lambda = \mu$ to $\Lambda = 4\mu$ up to $\mathcal{O}(g^2)$ ($\mathcal{O}(g^4)$). The solid (dashed) line comes from the pressure with $\Lambda = 2\mu$ up to $\mathcal{O}(g^2)$ ($\mathcal{O}(g^4)$). This figure is taken from [95].

Nambu-Jona-Lasinio (NJL) model instead of pQCD. This model is particularly useful to take into account the important phenomena such as the partial restoration of chiral symmetry at high density [96, 97, 98, 99].

The model Lagrangian we consider reads

$$\begin{aligned}
\mathcal{L}_{\rm NJL} &= \bar{q}(i\partial\!\!\!/ - m)q + \frac{1}{2}G_{_S}\sum_{a=0}^{8}[(\bar{q}\lambda^a q)^2 + (\bar{q}i\gamma_5\lambda^a q)^2] - G_{_D}[\det\bar{q}(1+\gamma_5)q + \text{h.c.}] \\
&+\frac{H}{2}\sum_{I,A=2,5,7}(\bar{q}i\gamma_5\lambda^I\tau^A C\bar{q}^T)(q^T Ci\gamma_5\lambda^I\tau^A q) \\
&+\frac{G'_{_D}}{8}\sum_{i,j,k=1,2,3}[(q\tilde{\lambda}_i\tilde{\tau}_k(1+\gamma_5)C\bar{q}^T)(\bar{q}\tilde{\lambda}_j\tilde{\tau}_k(1+\gamma_5)Cq)(\bar{q}_i(1+\gamma_5)q_j) + \text{h.c.}] \\
&-\begin{cases} \frac{1}{2}g_{_V}(\bar{q}\gamma^\mu q)^2 \\ \frac{1}{2}G_{_V}\sum_{a=0}^{8}[(\bar{q}\gamma^\mu\lambda^a q)^2 + (\bar{q}i\gamma^\mu\gamma_5\lambda^a q)^2] \end{cases}.
\end{aligned} \tag{3.29}$$

The term proportional to $G_{_S}$ makes a $\bar{q}q$ interaction and has a $U(3)_L \times U(3)_R$ symmetric four-fermi interaction where λ^a are the Gell-Mann matrices in flavor space with $\lambda^0 = \sqrt{2/3}$ I. The term proportional to $G_{_D}$ is called as the Kobayashi-Maskawa-'t Hooft (KMT) coupling which breaks $U(1)_A$ symmetry explicitly [93, 94]. We consider two types of vector interaction (the final line of Eq.(3.29)): The term proportional to $g_{_V}(>0)$ gives a universal repulsion among different flavors, while the one proportional to $G_{_V}(>0)$ gives flavor-dependent repulsion. The term proportional to H gives a qq interaction and a diquark condensation with color antitriplet,

flavor antitriplet and $J^P = 0^+$ state where $C = i\gamma_2\gamma_0$ is the charge conjugation matrix and τ^a are the Gell-Mann matrices in color space with $\tau^0 = \sqrt{2/3}$ I. The term proportional to ${G'_{_D}}^2$ is obtained by the Fierz transformation of the KMT term and gives a coupling between the chiral condensate and the diquark condensate. Here we have introduced a notation, $\tilde{\lambda}_{1,2,3} \equiv \lambda_{7,5,2}$ and $\tilde{\tau}_{1,2,3} \equiv \tau_{7,5,2}$.

In the mean field approximation, the constituent quark masses M_i and the gap parameters Δ_i are generated dynamically through the NJL interactions[3],

$$M_i = m_i - 2G_{_S}\sigma_i + 2G_{_D}\sigma_j\sigma_k + \frac{G'_{_D}}{4}|s_i|^2, \tag{3.30}$$

$$\Delta_i = -\left(H - \frac{G'_{_D}}{2}\sigma_i\right)s_i, \tag{3.31}$$

where $\sigma_i = \langle\bar{q}_i q_i\rangle$ is the chiral condensate in each flavor, $s_i = \langle\bar{q}^T C\gamma_5\tilde{\lambda}_i\tilde{\tau}_i q\rangle$ is the diquark condensate in each color and flavor with (i,j,k) corresponding to the cyclic permutation of u, d and s. The thermodynamic potential Ω is related to the pressure as $\Omega = -T\log Z = -PV$ with P given by

$$\begin{aligned} P(T,\mu_{u,d,s}) &= \frac{T}{2}\sum_\ell \int \frac{d^3p}{(2\pi)^3}\mathrm{Trln}\left(\frac{S^{-1}(i\nu_\ell,\mathbf{p})}{T}\right) \\ &\quad -G_{_S}\sum_i \sigma_i^2 - 4G_{_D}\sigma_u\sigma_d\sigma_s + \frac{g_{_V}}{2}\left(\sum_i n_i\right)^2 - \sum_{i=1,2,3}\frac{1}{2}(H - G'_{_D})|s_i|^2. \end{aligned} \tag{3.32}$$

Here $i\nu_\ell = (2\ell+1)\pi T$ is the Matsubara frequency, $n_i = \langle q_i^\dagger q_i\rangle$ is the quark number density in each flavor, and S is the quark propagator in the Nambu-Gor'kov representation [4],

$$\left[S^{-1}\right]^{ij}_{\alpha\beta} = \begin{pmatrix} [G_0^+]^{-1} & \sum_{i=1,2,3}\Delta_i\gamma_5\tilde{\lambda}_i\tilde{\tau}_i \\ -\sum_{i=1,2,3}\Delta_i^*\gamma_5\tilde{\lambda}_i\tilde{\tau}_i & [G_0^-]^{-1} \end{pmatrix} \tag{3.33}$$

where

$$[G_0^\pm]^{-1} = \not{p} - \hat{M} \pm \gamma_0\hat{\mu}^{\mathrm{eff}}. \tag{3.34}$$

Here, $\hat{M}$ is a unit matrix in color space and a diagonal matrix in flavor space, $\mathrm{diag}(M_u, M_d, M_s)$. The effective chemical potential matrix $\hat{\mu}^{\mathrm{eff}}$ is defined from

$$\hat{\mu}^{\mathrm{eff}} \equiv \hat{\mu} - g_{_V}\sum_j n_j \tag{3.35}$$

[2]In the GL approach and 3-flavor massless NJL model, this term, which comes from $U(1)_A$ anomaly, favors the coexistence of the chiral condensation and the diquark condensation from the context of hadron-quark continuity.

[3]In Appendix D, we derive this gap equation by using Bogoliubov-Valatin transformation.

[4]In the numerical simulation, we decompose this matrix into some metrices. We show the detail of this decomposition in Appendix E.

where each component of $\hat{\mu}$ is given by

$$\mu^{ij}_{\alpha\beta} = (\mu\delta^{ij} + \mu_Q Q^{ij})\delta_{\alpha\beta} + (\mu_3(\tau_3)_{\alpha\beta} + \mu_8(\tau_8)_{\alpha\beta})\delta^{ij}.$$

There are nine independent parameters in the (2+1)-flavor NJL model; the UV cutoff, Λ, the coupling constants, $G_{_S}, G_{_D}, g_{_V}, H$ and $G'_{_D}$ and the current quark masses, $m_{u,d}$ and m_s. Five parameters except for $g_{_V}(G_{_V}), H$ and $G'_{_D}$ have been determined from hadron phenomenology in the vacuum. We consider three parameter sets summarized in Table 3.1; HK (Hatsuda and Kunihiro), RKH (Rehberg, Klevansky and Hufner) and LKW (Lutz, Klimt and Weise) [96, 97, 98, 99].

Table 3.1: Parameter sets of (2+1)-flavor NJL model [96, 97, 98, 99].

	Λ(MeV)	$G_{_S}\Lambda^2$	$G_{_D}\Lambda^5$	$m_{u,d}$(MeV)	m_s(MeV)
HK	631.4	3.67	9.29	5.5	135.7
RKH	602.3	3.67	12.36	5.5	140.7
LKW	750	3.64	8.9	3.6	87

The magnitude of $g_{_V}(G_{_V})$ has not been determined well: Recent studies of the PNJL model applied to the QCD phase diagram suggest that $g_{_V}$ may be comparable to or larger than $G_{_S}$ [100, 101], so that we change its magnitude in the following range,

$$0 \leq \frac{g_{_V}}{G_{_S}} \leq 1.5. \tag{3.36}$$

The parameters H and $G'_{_D}$ are chosen to be $H = G_{_S}$ and $G'_D = G_{_D}$ as characteristic values [5].

The EOS of quark matter with strangeness is obtained from the above model under three conditions: (i) the charge neutrality among quarks and leptons, $\frac{2}{3}n_u - \frac{1}{3}n_d - \frac{1}{3}n_s - n_e - n_\mu = 0$, (ii) the color neutrality among quarks, $n_r = n_g = n_b$, and (iii) the β-equilibrium among quarks and leptons, $\mu_d = \mu_s = \mu_u + \mu_e$ and $\mu_e = \mu_\mu$. The ground state of the system is obtained by searching the maximum of the pressure in Eq. (3.32) with the conditions,

$$\frac{\partial P}{\partial \sigma_{u,d,s}} = \frac{\partial P}{\partial \Delta_{1,2,3}} = \frac{\partial P}{\partial \mu_{3,8}} = 0. \tag{3.37}$$

Let us first discuss a composition of the β-equilibrated quark matter at $T = 0$ without color superconductivity ($H = G'_{_D} = 0$). In Fig.3.2 (a), the number fractions ($n_{u,d,s,e}/n_{\rm tot}$ with $n_{\rm tot} = n_u + n_d + n_s = 3\rho$) as a function of the baryon density ρ are plotted. In Fig.3.2 (b), the constituent quark masses (M_i) as a function of ρ are plotted. These figures do not depend

[5] Corresponding values from the Fierz transformation are $H = \frac{3}{4}G_{_S}$ and $G'_D = G_{_D}$. For extensive analyses with other choice of parameters in the diquark channels, see [43, 102, 103].

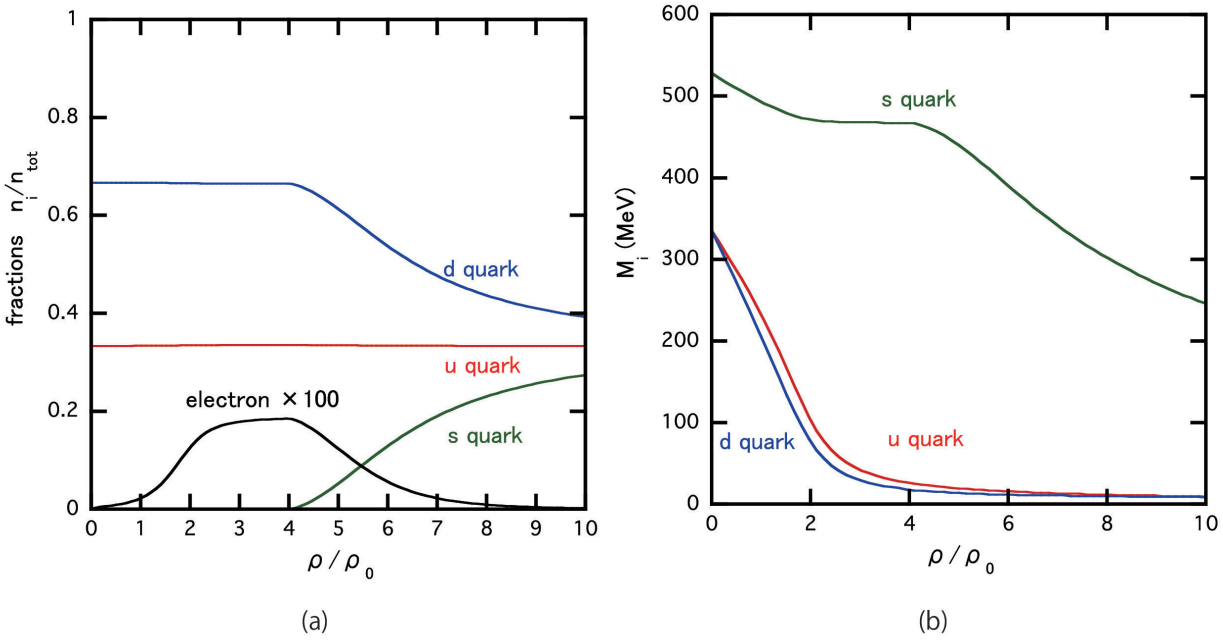

Figure 3.2: (a) The number fractions ($n_{u,d,s,e}/n_{\rm tot}$ with $n_{\rm tot} = n_u + n_d + n_s = 3\rho$) as a function of the baryon density ρ without color superconductivity ($H = G'_{D} = 0$). Red, blue and green lines correspond to u, d and s quark, respectively. The black line corresponds to the electron number fraction × 100. Muon does not appear due to the emergence of s quarks. (b) The constituent quark masses (M_i) as a function of ρ. Colors on each line are the same with those in (a). These figures are taken from [2].

on the magnitude of the vector type interaction g_{V} because the flavor-independent g_{V}-type interaction leads to a pressure in Eq.(3.32) depending only on $\mu^{\rm eff}_{\alpha,a}$.

At low densities, the s quark appears only above $\rho_{\rm th} \simeq 4\rho_0$ due to its heaviness as can be seen from Fig.3.2 (a): Here $\rho_{\rm th}$ is determined by the condition, $\mu_s(\rho_{\rm th}) = M_s(\rho_{\rm th})$. The dynamical masses of u and d quarks decrease rapidly below $\rho_{\rm th}$ due to partial restoration of chiral symmetry, while the s quark is affected only a little through the KMT interaction as seen from Fig.3.2 (b). Once the s-quark whose electric charge is negative starts to appear above $\rho_{\rm th}$, the number of electrons decreases to satisfy the charge neutrality. Since the electron

Table 3.2: The baryon density where the transition occurs for $0 < \rho < 6\rho_0$. NQ means the normal quark matter. We fix $(g_{V}/G_{S}, G'_{D}/G_{D}) = (0.5, 1)$.

	$H/G_{S} = 0.5$	$H/G_{S} = 0.75$	$H/G_{S} = 1$	$H/G_{S} = 1.5$	$H/G_{S} = 2$
NQ to 2SC	none	$(4.4 - 4.8)\rho_0$	0	0	none
2SC to CFL	none	none	$(4.8 - 5.8)\rho_0$	$(2.9 - 3.7)\rho_0$	none
NQ to CFL	none	none	none	none	0

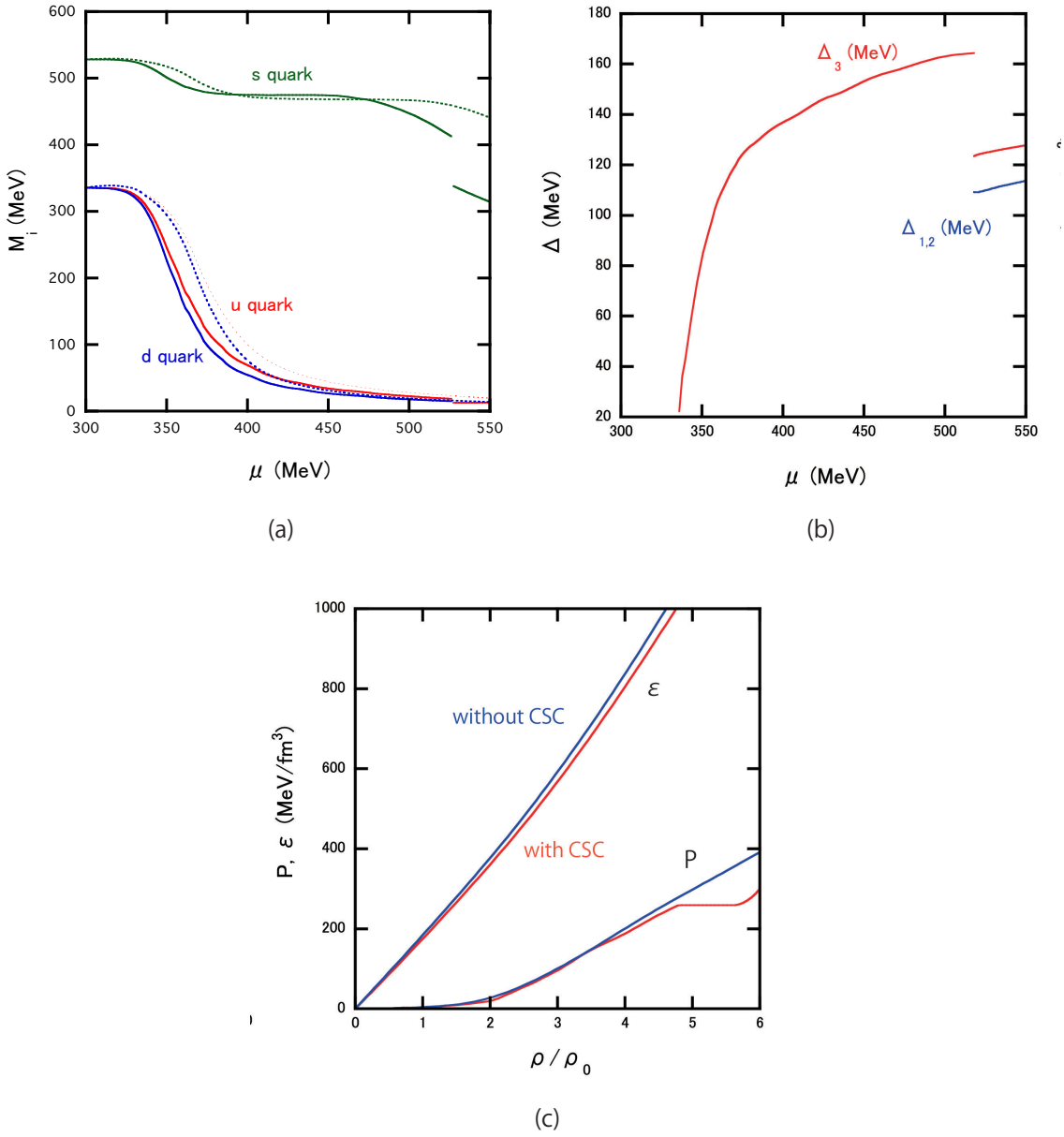

Figure 3.3: (a) The constituent mass as a function of the quark chemical potential μ. Solid (dotted) lines is the case with (without) CSC. Red, blue and green lines are u, d and s quarks respectively. (b) The gap parameters Δ_i $(i = 1, 2, 3)$ as a function of the quark chemical potential μ. Solid red line: Δ_3 corresponding to the pairing between u quark and d quark. Solid blue line: Δ_1 and Δ_2 corresponding to the ds pairing and su pairing, respectively. (c) The energy density (ε) and pressure (P) as a function of baryon number density ρ. The red lines show the quark EOSs with diquark condensate. The blue lines show the quark EOSs without diquark condensate. Figures (b) and (c) are taken from [4].

chemical potential does not exceed the muon mass 106MeV, the muons do not appear even at high density. In the high density limit, the system approaches the flavor symmetric u, d, s matter without leptons.

Let us discuss the effects of the interactions in the diquark channels (H and G'_D). We

survey how the color superconductivity (CSC) develops with $H/G_{_S} = 0.5, 0.75, 1, 1.5$ and 2 and $(g_{_V}/G_{_S}, G'_{_D}/G_{_D}) = (0.5, 1)$ for $0 < \rho < 6\rho_0$ related with the central density of NSs. We consider only 2SC and CFL phases. In Table 3.2, we summarize the baryon density where the transition takes place for various diquark interactions. NQ means the normal quark matter. Typically, if the magnitude of the diquark interaction is enough small ($H/G_{_S} = 0.5$), 2SC phase does not appear and only CFL phase appears at very high densities ($\rho > 6\rho_0$). As the diquark interaction becomes strong $H/G_{_S} = 0.75, 1, 1.5$, 2SC phase starts to emerge and CFL appears at lower densities. For example, in the case of $H/G_{_S} = 0.75$, the first order transition from the normal quark phase to 2SC phase takes place at $\mu = 520$ MeV (around $(4.4-4.8)\rho_0$) and CFL phase does not appear below $6\rho_0$. If we take $H/G_{_S} = 1(1.5)$, 2SC phase appears as the quark matter emerges and the first order transition from 2SC phase to CFL phase occurs at $\mu = 520(400)$ MeV (around $(4.8-5.8)((2.9-3.7))\rho_0$). Finally, if the diquark correlation becomes enough strong, CFL phase appears as the quark matter appears. If we take $H/G_{_S} = 0.75$ corresponding to the Fierz transformation, CSC barely appears inside NSs. Therefore, in this thesis, we take $H/G_{_S} = 1$ to see the effects of CSC on bulk properties of NSs. [6].

In Fig. 3.3 (a), we plot the constituent masses for u, d and s quarks as a function of the quark chemical potential μ. Solid and dotted lines correspond to the cases with and without CSC. The diquark condensates affect the behavior of the constituent quark masses (M_i) and the number fractions ($n_{i,e}/n_{\rm tot}$) through the coupled equations, Eq.(3.30). The threshold density for s quark becomes lower $\rho_{\rm th} \simeq 3.6\rho_0$ since the number of d quarks decreases in 2SC phase at a given baryon density with the condition of the charge neutrality. At around $\mu = 520$MeV, we can see the jump of constituent masses, which corresponds to the first order transition from 2SC to CFL phase. Fig. 3.3 (b) shows the gap parameters Δ_i as a function of the quark chemical potential μ. The red line corresponds to the ud pairing, and blue line corresponds to the ds or su pairings. With $H/G_{_S} = 1$, two-color superconductivity (2SC) appears as soon as the baryon density of the quark matter becomes finite at $\mu = 335$ MeV. The first-order transition from the 2SC to CFL phase can be seen more clearly. Fig. 3.3 (c) shows the thermodynamic quantities (P and ε) as a function of ρ in the (2+1)-flavor NJL model. The red (blue) lines correspond to the case with (without) CSC. In terms of the baryon density, 2SC (CFL) appears for $\rho < 5\rho_0$ ($5\rho_0 < \rho$) in the present parameter set. The plateau of the red line (P with CSC) reflects the fact that there is a first-order transition from 2SC to CFL. As we will see later, baryon density relevant to neutron stars with the hadron-quark crossover is below $5\rho_0$. Therefore, the CFL phase barely appears in the central core of the NSs in the present model.

[6]The EOS of [104], where $H/G_{_S} = 1.5$ is adopted, is consistent with our EOS at the same value of $H/G_{_S}$.

3.5 Brief Summary

In this chapter, we first summarized the two non-perturbative aspects of QCD; the chiral condensate induced by the strong $\bar{q}q$ correlation and the color superconductivity induced by the strong qq correlation. To treat the strongly interacting quark matter relevant to the central core of the neutron stars, we then introduced the $(2+1)$-flavor NJL model as as an effective theory of QCD. We showed how the chiral and diquark condensates evolve as a function of the baryon density and found that the partial restoration of chiral symmetry and the transition to the 2-flavor color superconducting phase take place for the quark chemical potential relevant to NSs, $\mu = 350 - 500$ MeV . Finally we derived the Q-EOS of strongly interacting quark matter which embodies these characteristic features.

Chapter 4

Cold Neutron Stars with Crossover

In this chapter, we introduce a phenomenological interpolation method at finite density region and apply the resultant EOS to cold neutron star observables. We show the smooth crossover from the hadronic phase to the quark phase makes EOS stiff so that massive NSs with $2M_\odot$ can be sustained independent of the choice of various hadronic EOSs and the choice of the interpolating methods. The internal structure and the cooling of NSs with the crossover and the effects of CSC on the bulk NS properties are also discussed. The discussions of this chapter are based on [1, 2, 3].

4.1 Phenomenological Model for Crossover

As discussed in Chapter 1, treating the point-like hadron as an independent degree of freedom loses its validity as the baryon density approaches the percolation region. In other words, the system in the intermediate density region can be described neither by an extrapolation of the hadronic EOS from the low-density side nor by an extrapolation of the quark EOS from the high-density side. Under such situation, it does not make much sense to apply the Gibbs criterion of two phases I and II, $P_{\rm I}(T_c, \mu_c) = P_{\rm II}(T_c, \mu_c)$ since $P_{\rm I}$ and $P_{\rm II}$ are not reliable in the transition region.

One may expect a gradual onset of quark degrees of freedom in dense matter associated with the percolation of finite size hadrons, i.e., a smooth crossover from the hadronic matter to the quark matter. A similar concept about the crossover is already considered as the BEC-BCS crossover [38]. Such a percolation picture of hadrons has been also discussed in seminal works such as [39, 40]. Also, hadron-quark continuity [41, 42] and hadron-quark crossover [44, 105] have been discussed in relation to the existence of color superconductivity at high density.

Fig. 4.1 illustrates the above situation. At the low densities, quarks are confined inside baryons. As density increases, quarks in the finite size baryons become percolated. Finally, the deconfined quarks emerge at high density region. The resultant EOS based on the smooth crossover picture should be the smooth curve as shown by the solid line in this figure. In the intermediate region, the hadronic EOS based on the point-like hadron picture and the weakly

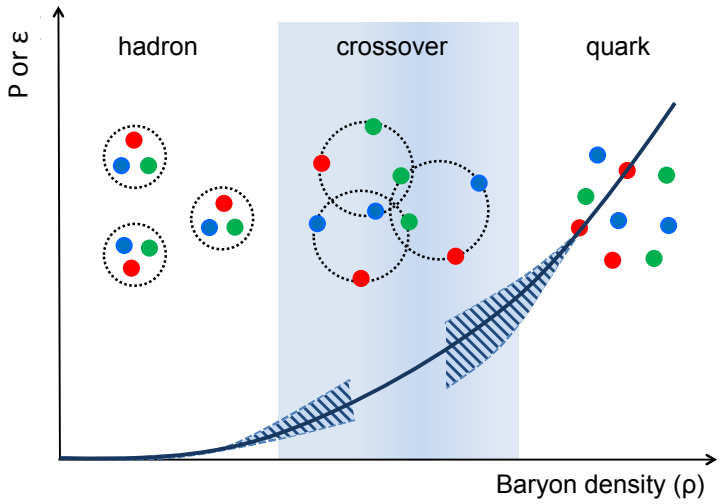

Figure 4.1: Schematic picture of the QCD thermodynamic quantities (such as the pressure P or the energy density ε) as a function of the baron density (ρ) under the assumption of the hadron-quark crossover. The crossover region where finite-size hadrons start to overlap and percolate is shown by the shaded area. The thermodynamic quantities calculated on the basis of the point-like hadrons (shown by the dashed line at low density) and that calculated on the basis of weakly interacting quarks (shown by the dashed line at high density) lose their validity in the crossover region. This figure is adopted from [2].

interacting quark EOS break down and have large uncertainties shown in the shaded areas at low and high densities.

Since the first principle QCD calculation at high baryon density is not available and effective models at finite baryon density with proper treatment of the confinement phenomena do not exist at present, we will consider a phenomenological "interpolation" between the H-EOS and Q-EOS as a first step. Such an interpolation is certainly not unique: Here we consider two simplest possibilities, P-interpolation and ε-interpolation as described below.

- P-interpolation as a function of baryon density

$$P(\rho) = P_H(\rho)w_-(\rho) + P_Q(\rho)w_+(\rho), \tag{4.1}$$

$$w_\pm(\rho) = \frac{1}{2}\left(1 \pm \tanh\left(\frac{\rho - \bar{\rho}}{\Gamma}\right)\right), \tag{4.2}$$

where P_H and P_Q are the pressure in the hadronic matter and that in the quark matter, respectively. The interpolating function $w_\pm$ is similar to the phenomenological interpolation method at finite temperature in [106, 107, 108] (see Appendix F). There are two phenomenological parameters, $\bar{\rho}$ and Γ. $\bar{\rho}$ means the typical crossover density and Γ is the width of the crossover region. The window $\bar{\rho} - \Gamma \sim \rho \sim \bar{\rho} + \Gamma$ characterizes the crossover region in which both hadrons and quarks are strongly interacting, so that neither pure hadronic EOS nor pure quark EOS are reliable. The percolation picture illustrated in Fig.

4.1 is best implemented by the interpolation in terms of the baryon density ρ instead of the baryon chemical potential. One should not confuse Eq.(4.1) with the pressure in the mixed phase associated with the first-order phase transition in which $w_\pm$ is considered to the volume fraction of each phase. In our crossover picture, the system is always uniform and w_- (w_+) should be interpreted as the degree of reliability of H-EOS (Q-EOS) at the given baryon density.

To calculate the energy density ε as a function of ρ in a thermodynamically consistent way, we integrate the thermodynamical relation,

$$P = \rho^2 \frac{\partial(\varepsilon/\rho)}{\partial\rho} \tag{4.3}$$

and obtain

$$\begin{aligned} \varepsilon(\rho) &= \varepsilon_H(\rho) w_-(\rho) + \varepsilon_Q(\rho) w_+(\rho) + \Delta\varepsilon & (4.4)\\ \Delta\varepsilon &= \rho \int_{\bar\rho}^{\rho} (\varepsilon_H(\rho') - \varepsilon_Q(\rho')) \frac{g(\rho')}{\rho'} d\rho' & (4.5) \end{aligned}$$

with

$$\begin{aligned} g(\rho) &= \frac{2}{\Gamma}(e^X + e^{-X})^{-2}, & (4.6)\\ X &= \frac{\rho - \bar\rho}{\Gamma}. & (4.7) \end{aligned}$$

Here ε_H (ε_Q) is the energy density obtained from H-EOS (Q-EOS). $\Delta\varepsilon$ is an extra term which guarantees the thermodynamic consistency. Note that the energy per baryon from the extra term $\Delta\varepsilon/\rho$, which receives main contribution from the crossover region, is finite even in the high-density limit. Therefore the energy density obtained by the procedure does not reach to the energy density of the pure quark matter.

- ε-interpolation as a function of baryon density

$$\varepsilon(\rho) = \varepsilon_H(\rho) w_-(\rho) + \varepsilon_Q(\rho) w_+(\rho). \tag{4.8}$$

Other thermodynamic quantities are obtained through the thermodynamic relation;

$$\begin{aligned} P(\rho) &= P_H(\rho) w_-(\rho) + P_Q(\rho) w_+(\rho) + \Delta P & (4.9)\\ \Delta P &= \rho(\varepsilon_Q(\rho) - \varepsilon_H(\rho)) g(\rho), & (4.10) \end{aligned}$$

and $\mu = (\varepsilon + P)/\rho$. Here ΔP is an extra term which guarantees the thermodynamic consistency; it is a localized function in the crossover region and obeys the property, $\Delta P(0) = \Delta P(\infty) = 0$.

In the following, we consider crossover window which satisfies the following physical conditions: (i) The system is always thermodynamically stable $dP/d\rho > 0$, and (ii) the normal nuclear matter is well described by the H-EOS so that $\bar\rho - 2\Gamma > \rho_0$ is satisfied.

4.2 Neutron Star Properties with P-interpolation without CSC

4.2.1 Interpolated EOS

In the present section, we consider the case of P-interpolation without diquark condensation ($H = G'_D = 0$). In Fig.4.2 (a) and (b), pressure and energy density as a function of density are plotted in the case of the P-interpolation between TNI2u for H-EOS and NJL with $g_V = G_S$ for Q-EOS according to Eq.(4.1). The crossover window is chosen to be $(\bar{\rho}, \Gamma) = (3\rho_0, \rho_0)$ and is shown by the shaded area on the horizontal axis. The filled circles denote the onset of strangeness degrees of freedom, either hyperons or strange quarks. We comment on that TNI2u and NJL with the "universal" four-Fermi vector type interaction g_V include hyperons or strange quarks at almost the same density $\rho_{\rm th} \sim 4\rho_0$. An important lesson one can learn from Fig.4.2 is that the H-EOS (Q-EOS) is nothing more than the asymptotic form of the "true" $P(\rho)$ around $\rho = 0$ ($\rho = \infty$). Therefore, naive extrapolation of H-EOS and Q-EOS beyond their applicability would miss essential physics. To see the stiffness of the interpolated EOS, we plot the pressure as a function of energy density in Fig.4.3 (a). The parameters are the same as in Fig. 4.2. At higher density region than the crossover window, the interpolated EOS

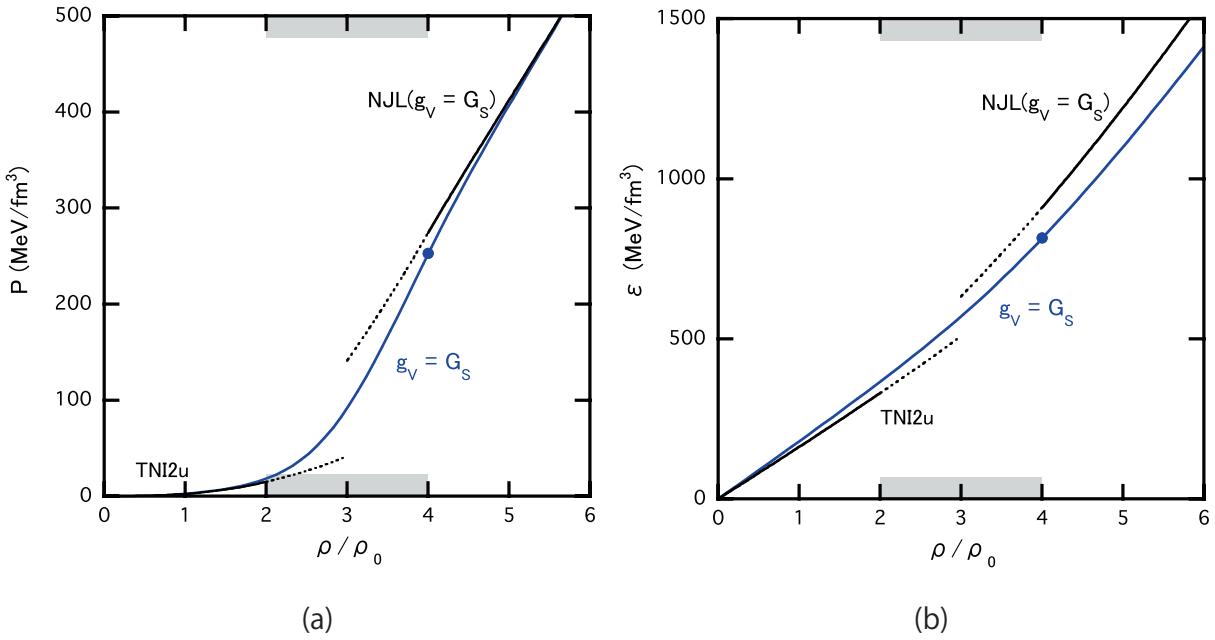

Figure 4.2: (a) The interpolated pressure between TNI2u H-EOS and NJL Q-EOS with $g_V = G_S$ for $(\bar{\rho}, \Gamma) = (3\rho_0, \rho_0)$. Pressure is illustrated by a blue line. The filled circle denotes the threshold density of strangeness. (b) The energy density obtained from the interpolated pressure in (a). Energy density is illustrated by a blue line. The filled circle denotes the threshold density of strangeness. These figures are taken from [2].

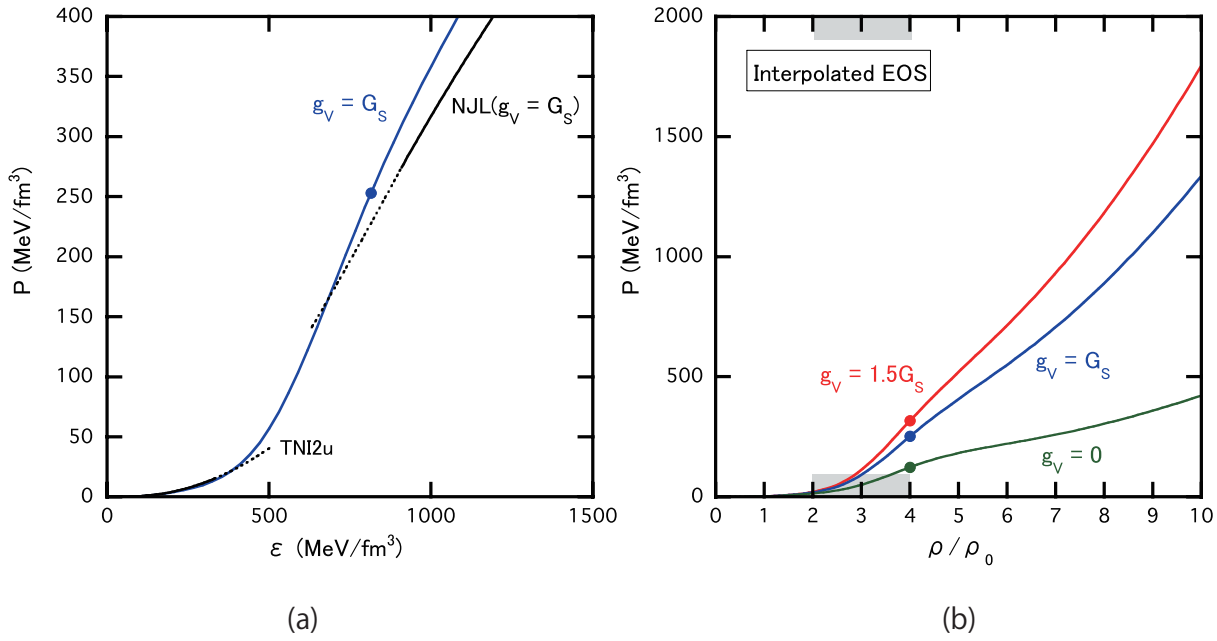

Figure 4.3: (a) The relation between interpolated pressure and the energy density. The parameters are same as Fig. 4.2 (a). The filled circle denotes the threshold density of strangeness. (b) Interpolated pressure (P) as a function of baryon density ρ for the case $(\bar{\rho}, \Gamma) = (3\rho_0, \rho_0)$ with $g_V/G_S = 0, 1.0, 1.5$. These figures are taken from [2].

is certainly stiffer that the hadronic and quark EOSs. In Fig.4.3 (b), we plot the interpolated EOS using TNI2u and NJL for various different values of $g_V/G_S = 0, 1.0, 1.5$. From this figure, we can clearly see the vector type interaction g_V makes EOS stiff. In the following, we call this phenomenological EOS as "CRover-C" EOS.

4.2.2 Mass-Radius Relation

We now solve the Tolman-Oppenheimer-Volkov (TOV) equation Eq. (1.5) to obtain M-R relationship by using the EOSs with and without the hadron-quark crossover.

In Fig. 4.4(a), we show the M-R relationship for various H-EOSs with hyperons whose onset is denoted by the filled circles. The crosses denote the points where maximum masses are realized: In all cases, $M_{\rm max}$ does not reach $2M_\odot$ due to the huge softening of EOS by the hyperon mixture. In Fig. 4.4(b), we show the M-R relationship with the CRover-C EOSs: For the H-EOS, we consider the same EOSs as shown in Fig. 4.4(a), while for the Q-EOS, we adopt the HK-parameter set with $g_V = G_S$ as a typical example. The crossover window is fixed to be $(\bar{\rho}, \Gamma) = (3\rho_0, \rho_0)$. Cases for different parameters in Q-EOS as well as for different window parameters are discussed in the next subsection.

The red lines in Fig. 4.4(b) correspond to the cases with TNI2u and TNI2, the blue lines correspond to TNI3u and TNI3, and the green lines correspond to SCL3ΛΣ and AV18+TBF.

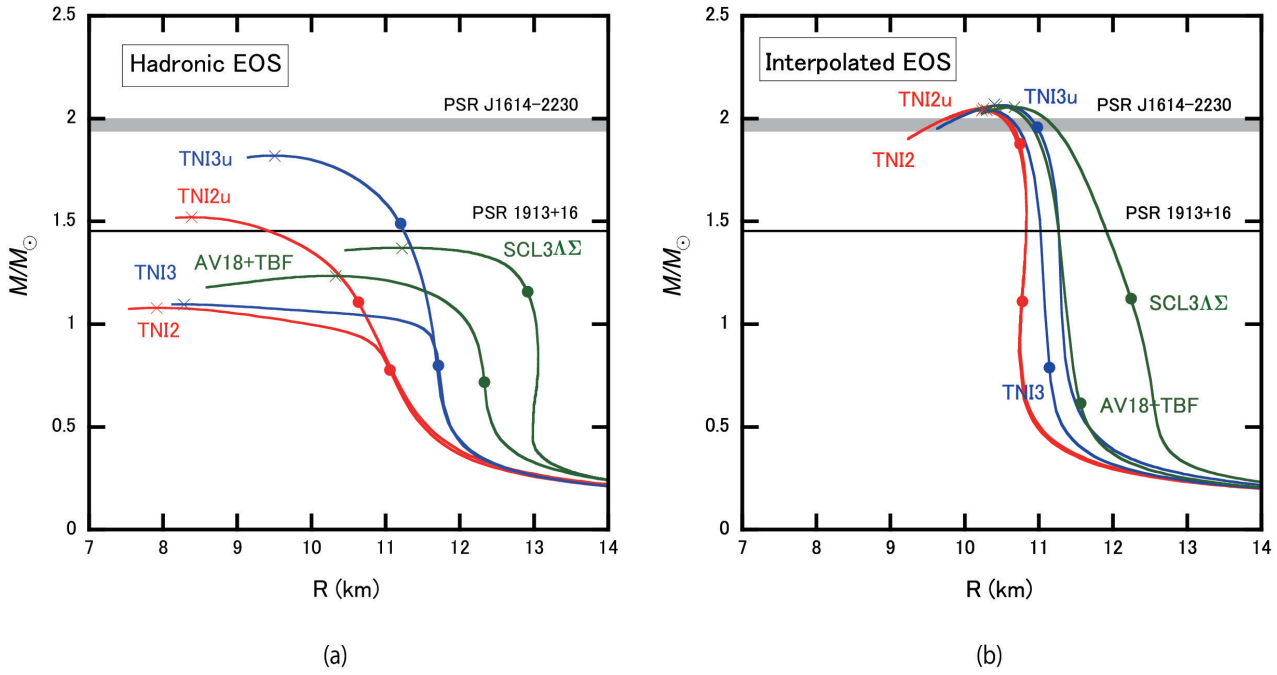

Figure 4.4: $M-R$ relationships. (a)$M-R$ relationships with various H-EOS including hyperons. Solid red lines: TNI2u (universal 3-body force with $\kappa = 250$MeV) and TNI2 (3-nucleon force with $\kappa = 250$MeV). Solid blue lines: TNI3u (universal 3-body force with $\kappa = 300$MeV) and TNI3 (3-nucleon force with $\kappa = 300$MeV) [31, 75]. Solid green lines: AV18+TBF (G-matrix approach with hyperons) [76] and SCL3ΛΣ (Relativistic mean field model with a chiral SU(3) symmetry) [71]. The gray band denotes $M = (1.97 \pm 0.04)M_\odot$ for PSR J1614-2230. The solid black line denotes $M = 1.44M_\odot$ for PSR 1913+16. (b) M-R relationship with the EOS interpolated between H-EOS in (a) and Q-EOS with the HK parameter set and $g_V = G_S$, by the window parameters $(\bar{\rho}, \Gamma) = (3\rho_0, \rho_0)$. Colors on each line are the same with those in (a). These figures are taken from [2].

The onset of strangeness and the maximum mass are denoted by the filled circles and the crosses, respectively. Irrespective of the H-EOSs, the interpolated EOS can sustain hybrid star with $M_{\rm max} > 2M_\odot$: A smooth crossover around $\rho \sim 3\rho_0$ and the stiff Q-EOS due to repulsive vector interaction are two fundamental reasons behind this fact. Also, we note that the radius of the hybrid star with interpolated EOS is in a range $R = (11 \pm 1)$km for $0.5 < M/M_\odot < 2.0$, except for the case of SCL3ΛΣ. The reason why the case with SCL3ΛΣ is different from others can be easily seen from Fig. 2.3 (a): The pressure P of SCL3ΛΣ is nearly twice as large as that of the other EOSs at $\rho = (1-2)\rho_0$. This leads to a larger R of light NSs. Such a narrow window of R independent of the values of M is consistent with the phenomenological constraints on R based on recent observations of both transiently accreting and bursting sources [16, 22, 23, 109].

It is in order here to comment on the relationship between the maximum mass and the nuclear incompressibility κ. From the properties of finite nuclei, the nuclear incompressibility κ is estimated to be (240 ± 20)MeV [110]. The interpolated EOSs with TNI2 and TNI2u are consistent with this empirical κ, and yet they can reach $M_{\rm max} > 2M_\odot$. In other words, what

Table 4.1: $M_{\max}/M_\odot$ (ρ_c/ρ_0) for different choice of H-EOS and different stiffness of Q-EOS.

H-EOS	$g_{_V}$=$G_{_S}$	$g_{_V}$=1.5$G_{_S}$
TNI2u	2.05 (6.1)	2.17 (5.5)
TNI2	2.04 (6.1)	2.16 (5.9)
TNI3u	2.07 (5.9)	2.18 (5.4)
TNI3	2.04 (6.1)	2.16 (5.5)
Paris+TBF	2.06 (6.1)	2.17 (5.6)
AV18+TBF	2.06 (6.1)	2.17 (5.5)
SCL3ΛΣ	2.06 (5.9)	2.17 (5.5)

is important to sustain massive hybrid stars is not the value of the incompressibility, but the stiffness of the EOS at and above $\sim 3\rho_0$. The value of radius mainly comes from the EOS properties around $(1-2)\rho_0$. On the other hand, the maximum mass strongly depends on the stiffness of EOS around $(3-4)\rho_0$.

In Table 4.1, we summarize the maximum mass and the associated central density of the hybrid star with CRover-C EOS with $g_{_V}$=$G_{_S}$ and $g_{_V}$=1.5$G_{_S}$. In all combinations of H-EOS and Q-EOS, $M_{\max}$ exceeds $2M_\odot$ with the central density, $\rho_c = (5.4-6.1)\rho_0$.

Now, let us discuss the internal structure of the hybrid star, in particular its strangeness content. From the location of the filled circles in Fig. 4.4(b), one finds that the flavor-independent universal three-baryon repulsion in TNI2u and TNI3u increases the onset density of the strangeness inside the hybrid star due to the repulsive force acting on the hyperons. This can be seen more explicitly by plotting the radial profile of the hybrid star: The upper panels of Fig.4.5 show the $\rho - r$ relationships for $2M_\odot$ and $1.44M_\odot$ hybrid stars with TNI2 (left) and TNI2u (right). The threshold densities of the strangeness given in Table 2.2 are indicated by the double lines. In CRover-C EOSs, the above stars turn out to have almost the same radius. The lower illustrations of Fig.4.5 show the cross sections of the corresponding hybrid stars.

These figures imply that, even if the mass and the radius are the same, the strangeness content of the hybrid stars can be quite different. There are two important points. (i) Due to the stiffness of EOSs, which comes from crossover, the central density for NSs with crossover is much smaller that that without crossover even if the masses are the same. (ii) The threshold density for strangeness for TNI2u larger than that for TNI2 due to the repulsive force among hyperons.

This point is of particular interest for the cooling problem of NSs. As is well known, NSs with a Y-mixed core undergo an extremely rapid cooling due to the efficient ν-emission processes called "hyperon direct URCA" (Y-Durca, e.g., $\Lambda \to p + e^- + \bar{\nu}_e$, $p + e^- \to \Lambda + \nu_e$) and are cooled very rapidly below the detection limit of thermal X-ray. Therefore, for the NSs consisting of pure hadronic components with Y, only the very light-mass NSs ($M < (1.0-1.2)M_\odot$ without

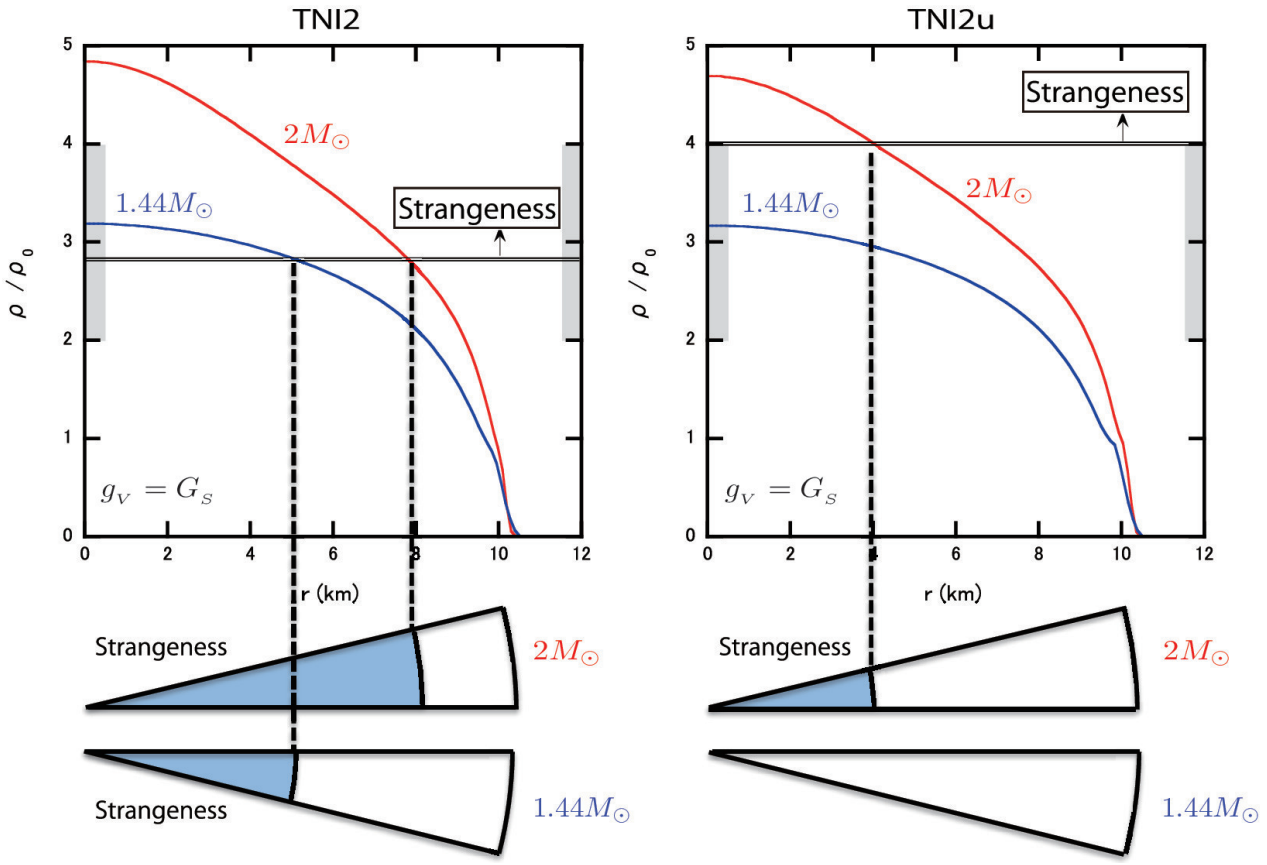

Figure 4.5: Density-profiles $\rho(r)$ with r being the distance from the center for the $2.0M_\odot$ star (red line) and $1.44M_\odot$ star (blue line). In the left upper panel TNI2 H-EOS and Q-EOS with $g_V = G_S$ and the HK parameter set are used in the interpolation with the window parameters $(\bar{\rho}, \Gamma) = (3\rho_0, \rho_0)$, while in the right upper panel TNI2u H-EOS and Q-EOS above are used. Double line shows the density above which the strangeness appears. Lower illustrations show the schematic internal structure. Only the blue shaded regions contain strangeness degrees of freedom. This figure is taken from [2].

hyperons, as in Fig. 2.3 (b) with TNI2u case) can escape from Y-Durca rapid cooling. This means an unlikely situation that all the NSs whose $T_{\rm sur}$ are observed should be light-mass stars in spite of the fact that the observed mass distribution is centered around $(1.4 - 1.5)M_\odot$ [15]. On the contrary, in the case of the hybrid star with $g_V = G_S(1.5G_S)$ under consideration, NSs as heavy as up to $1.9(2.0)M_\odot$ can avoid this rapid cooling, allowing the $T_{\rm sur}$-observed NSs to be from the light-mass to heavy mass stars ($M \leq (1.9 - 2.0)M_\odot$, as in Fig. 4.6 (a)). However, in the case of the hybrid star with smooth crossover, "quark direct URCA" (Q-Durca) instead of Y-Durca may takes place in the crossover region. The effect of spin-singlet and spin-triplet color superconductivity on this Q-Durca is an interesting open question to be studied.

4.2.3 Dependence on Q-EOS

To see how the hybrid star structure changes by the stiffness of Q-EOS, we plot $M-\rho_c$ relationship for $g_{_V}/G_{_S}=0,0.5,1.0,1.5$ with HK parameter set in Fig.4.6(a). We take TNI2u for H-EOS and the same crossover window $(\bar{\rho},\Gamma)=(3\rho_0,\rho_0)$ as in Fig.4.4. For comparison, the $M-\rho_c$ relationship only with TNI2u is plotted by the dashed line. Fig.4.6(b) shows the corresponding $M-R$ relations. As anticipated, $M_{\rm max}$ increases as $g_{_V}$ increases.

In Table 4.2, we show how $M_{\rm max}$ and ρ_c depend on the choice of $g_{_V}$ and the choice of the NJL parameter set. Although the parameter dependence is not entirely negligible, the massive hybrid star with $2M_\odot$ can be sustained for sufficiently large values of $g_{_V}$.

Finally, we consider the flavor-dependent vector interaction proportional to $G_{_V}$ given in Eq.(3.29). In the high density limit where u,d,s quarks have equal population, $\langle u^\dagger u\rangle=\langle d^\dagger d\rangle=\langle s^\dagger s\rangle$, the $g_{_V}$ interaction and the $G_{_V}$ interaction have the same contribution to the pressure in the mean-field approximation if we make the identification, $G_{_V}=\frac{3}{2}g_{_V}$. Motivated by this relation, we show $M_{\rm max}$ and ρ_c for $G_{_V}/G_{_S}=1.5,2.25,3.0$ in Table 4.3. For the density relevant to the core of the hybrid stars, the flavor $SU(3)$ limit is not yet achieved due to the s-quark mass (see Fig. 3.2 (a)). Therefore, the EOS for the flavor-dependent repulsion with $G_{_V}=\frac{3}{2}g_{_V}$

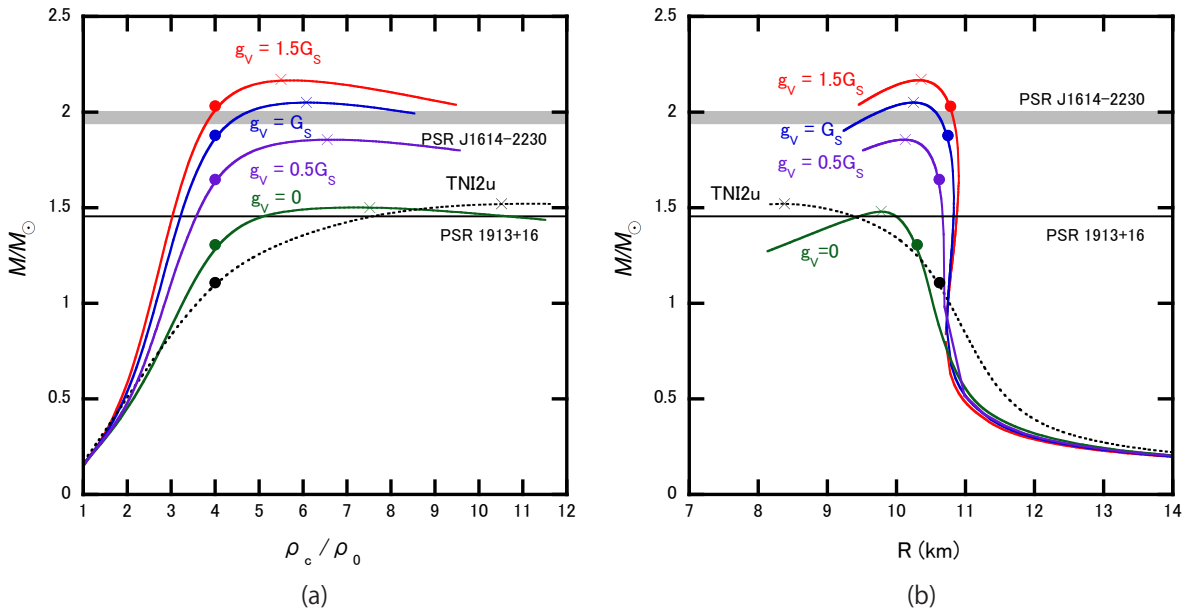

Figure 4.6: (a) $M-\rho_c$ relationships with the interpolated EOSs. We adopt the HK-parameter set for the Q-EOS with various $g_{_V}/G_{_S}=0,0.5,1.0,1.5$. The crossover window are fixed to be $(\bar{\rho},\Gamma)=(3\rho_0,\rho_0)$. The cross symbols denote the points of $M_{\rm max}$, while the filled circles denote the points beyond which the strangeness appears. The gray band denotes $M=(1.97\pm0.04)M_\odot$ for PSR J1614-2230. The solid black line denotes $M=1.44M_\odot$ for PSR 1913+16. (b) M-R relationships with the interpolated EOSs. These figures are taken from [2].

Table 4.2: The values of $M_{\max}/M_\odot$ (ρ_c/ρ_0) for $g_{_V}/G_{_S} = 1.0, 1.5, 2.0$ with $(\bar{\rho}, \Gamma) = (3\rho_0, \rho_0)$ and TNI2u. The parameter sets of the NJL model, HK, RKH and LKW, are given in Table 3.1.

Q-EOS	$g_{_V}$=$G_{_S}$	$g_{_V}$=1.5$G_{_S}$	$g_{_V}$=2$G_{_S}$
HK	2.05 (6.1)	2.17 (5.5)	2.24 (5.4)
RKH	1.99 (6.2)	2.12 (5.8)	2.20 (5.4)
LKW	1.72 (7.5)	1.87 (6.7)	1.97 (6.3)

is softer than the flavor independent repulsion with $g_{_V}$. This can be seen by comparing the corresponding values in Table 4.3 and those in Table 4.2. In any case, the massive hybrid star is possible for sufficiently large values of $G_{_V}$.

Table 4.3: $M_{\max}/M_\odot$ (ρ_c/ρ_0) for the HK parameter set with the flavor-dependent repulsion $G_{_V}$. The crossover window is $(\bar{\rho}, \Gamma) = (3\rho_0, \rho_0)$ and the hadronic EOS is TNI2u.

$G_{_V}$=1.5$G_{_S}$	$G_{_V}$=2.25$G_{_S}$	$G_{_V}$=3.0$G_{_S}$
1.87 (6.6)	1.99 (6.2)	2.07 (5.8)

4.2.4 Dependence on Crossover Window

In Table 4.4, we show $M_{\max}$ and ρ_c for different choice of the crossover window parameterized by $\bar{\rho}$ and Γ. TNI2u and HK parameter set are adopted for H-EOS and Q-EOS for various vector interaction $g_{_V}$, respectively. As the crossover window becomes lower and/or wider in baryon density, the CRover-C EOS becomes stiffer and $M_{\max}$ becomes larger. This can be understood by considering that the effects of the crossover and strongly interacting quark matter make EOSs stiff. To be compatible with the observed massive NS with $M = (1.97 \pm 0.04)M_\odot$, the crossover needs to occur in $(2-4)\rho_0$.

4.2.5 Sound Velocity of Interpolated EOS

One of the measures to quantify the stiffness of EOS is the sound velocity

$$v_{_S} = \sqrt{dP/d\varepsilon}. \tag{4.11}$$

In Fig.4.7, we plot $v_{_S}^2$ for our interpolated EOS with $g_{_V}/G_{_S} = 0, 1.0, 1.5$ as a function of ρ. For a comparison, we plot the sound velocity squared of TNI2u by the dotted line. The kinks of $v_{_S}$ at $\rho \simeq 4\rho_0$ are caused by the softening of EOS by the appearance of strangeness. The enhancement of $v_{_S}$ of CRover-C EOS relative to the pure hadronic EOS takes place just at and above the crossover window.

Table 4.4: $M_{\max}/M_\odot$ (ρ_c/ρ_0) under the variation of the parameters, $\bar{\rho}$ and Γ, which characterize the crossover window. H-EOS and Q-EOS are obtained from TNI2u and HK parameter set, respectively. Columns without numbers are the excluded cases corresponding to $\bar{\rho} - 2\Gamma < \rho_0$.

	$\Gamma/\rho_0 = 1$		$\Gamma/\rho_0 = 2$	
$\bar{\rho}$	g_V=G_S	g_V=1.5G_S	g_V=G_S	g_V=1.5G_S
$3\rho_0$	2.05 (6.1)	2.17 (5.5)	–	–
$4\rho_0$	1.89 (7.2)	1.97 (6.8)	–	–
$5\rho_0$	1.73 (8.2)	1.79 (8.0)	1.74 (8.0)	1.80 (7.7)
$6\rho_0$	1.60 (9.6)	1.64 (9.3)	1.62 (9.2)	1.66 (9.0)

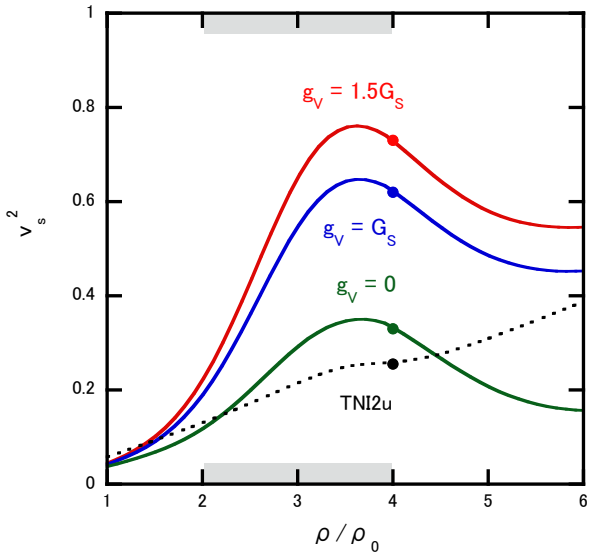

Figure 4.7: Sound velocity squared v_S^2 as a function of baryon density ρ. Solid lines: $v_S^2 - \rho$ obtained from the interpolated EOS between the H-EOS with TNI2u and the Q-EOS with $g_V/G_S = 0, 1.0, 1.5$. The crossover window is $(2-4)\rho_0$ and is shown by the shaded area in the horizontal axis. Dotted line : that for pure H-EOS with TNI2u. The filled circles denote the points beyond which strangeness starts to appear. This figure is adopted from [2].

4.2.6 Stability of Hybrid Star

The NSs are gravitationally stable if the average adiabatic index $\tilde{\gamma}$ satisfies the following inequality [111]:

$$\tilde{\gamma} \equiv \frac{\int_0^R \gamma P d^3r}{\int_0^R P d^3r} > \frac{4}{3} + \lambda \frac{GM}{R}. \tag{4.12}$$

Here

$$\gamma \equiv \frac{d\ \log P}{d\ \log \rho} \tag{4.13}$$

is the adiabatic index. Also, $\lambda GM/R$ with λ being a numerical constant of order unity is a general relativistic correction whose magnitude is much less than 1. Since γ of our H-EOS is about 2 at all densities and γ of our Q-EOS is larger than 4/3 due to the constituent quark mass and the repulsive vector interaction, Eq.(4.12) is always satisfied and our hybrid star is gravitationally stable. [1]

4.3 Neutron Star Properties with ε-interpolation without CSC

4.3.1 Interpolated EOS

In this section we consider the different interpolation procedure using the energy density ε as a function of ρ given in Eq.(4.8) without the diquark correlation ($H = G'_D = 0$). Shown

[1] For the free non-relativistic matter, $\gamma = 5/3$. On the other hand, for the free relativistic matter, $\gamma = 4/3$.

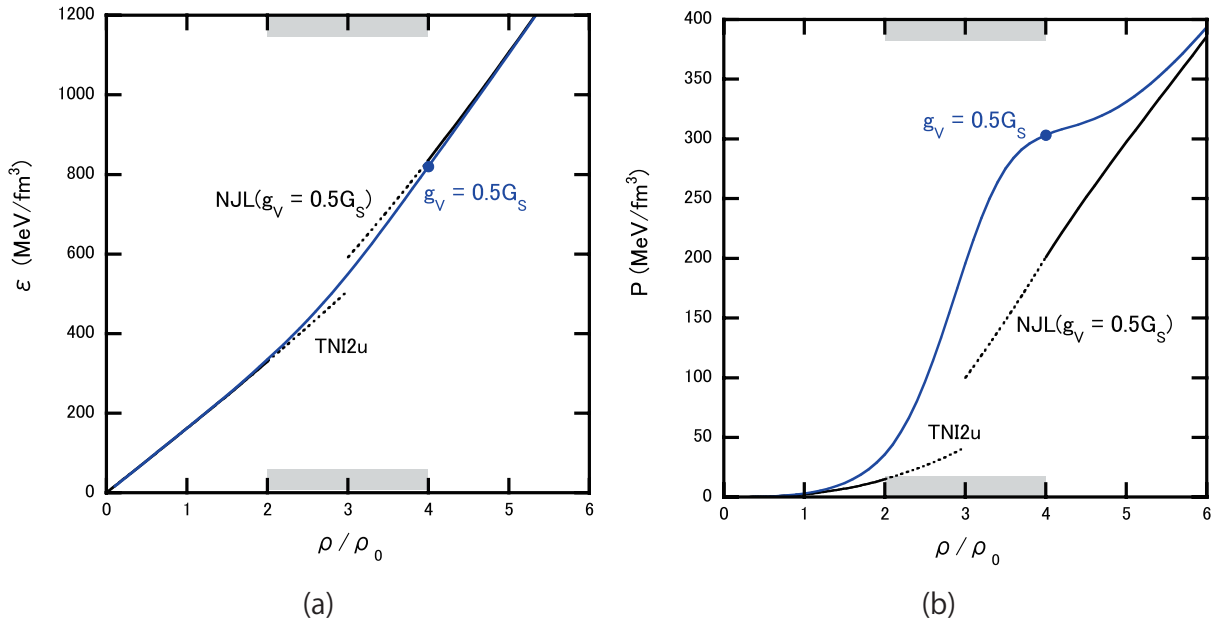

Figure 4.8: (a) The interpolated energy density between TNI2u H-EOS and NJL Q-EOS with $g_V = 0.5G_S$ for $(\bar{\rho}, \Gamma) = (3\rho_0, \rho_0)$. Energy density is illustrated by a blue line. The filled circle denotes the threshold density of strangeness. (b) The pressure obtained from the interpolated energy density in (a). The pressure is illustrated by a blue line. The filled circle denotes the threshold density of strangeness. These figures are taken from [2].

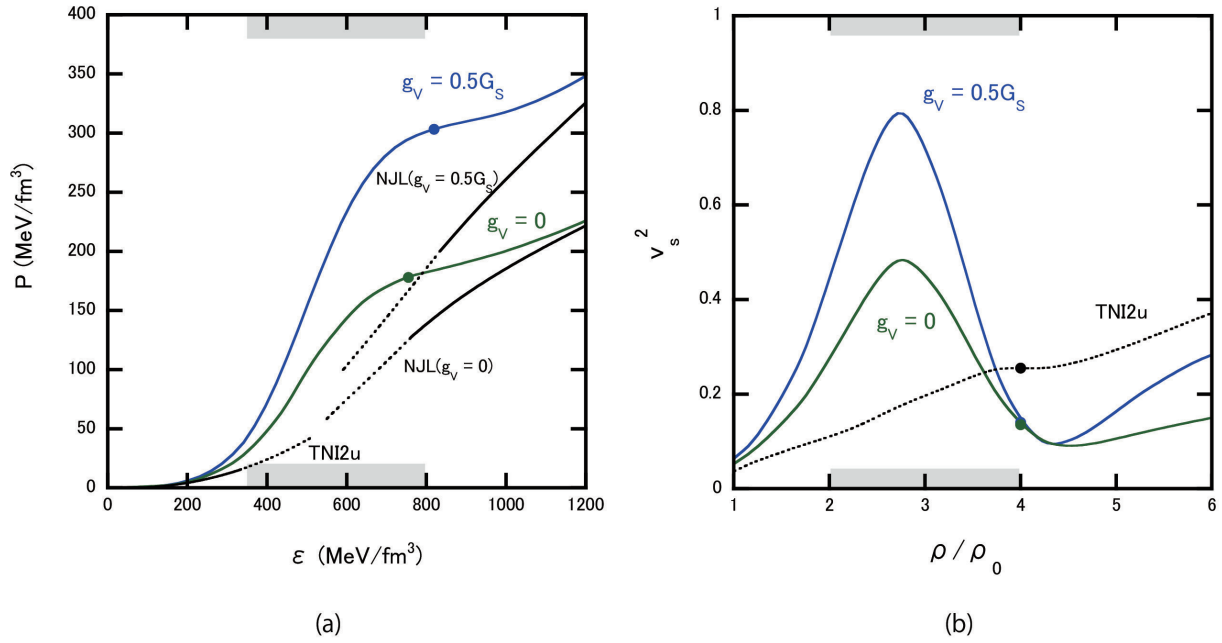

Figure 4.9: (a) The relation between the interpolated energy density and the resultant pressure for $g_V = 0$ (green) and $g_V = 0.5G_S$ (blue). The crossover window is $(2-4)\rho_0$. The filled circle denotes the threshold density of the strangeness. (b) Sound velocity squared v_s^2 as a function of baryon density ρ. Solid lines show $v_s^2 - \rho$ obtained from the interpolated EOS with $g_V/G_S = 0, 0.5$, while the dotted line corresponds to the TNI2u hadronic EOS. The filled circles denote the points beyond which strangeness starts to appear. Those figures are taken from [3].

in Fig.4.8 (a), the energy density is interpolated as a function of the baryon density between TNI2u for H-EOS and NJL with $g_V = 0.5G_S$ for Q-EOS. The crossover window is chosen to be $(\bar{\rho}, \Gamma) = (3\rho_0, \rho_0)$ and is shown by the shaded area on the horizontal axis. The pressure obtained from the interpolated energy density using the thermodynamic relation is shown in Fig. 4.8 (b). Due to the extra positive term ΔP in Eq.(4.10), the full pressure is larger than P_H and P_Q in the crossover region with the ε-interpolation procedure. Although ΔP is necessary for the thermodynamic consistency, its physical interpretation is not clear at the moment and is left for the future studies. The difference between P-interpolation and ε-interpolation is that the extra term in ε-interpolation vanishes at $\rho \to 0,\ \infty$. On the other hand, the extra term in P-interpolation does not vanish at all densities.

To see the stiffness of EOS, we show the energy density as a function of pressure for the ε-interpolated EOS between the TNI2u as a hadronic EOS and the NJL with $g_V = 0$ ($g_V = 0.5G_S$) as a quark EOS in Fig.4.9 (a). The sound velocity squared as a function of ρ is also shown in Fig.4.9 (b). In both figures, the onset of the strangeness is indicated by the filled circles. From both figures, one finds that the CRover-C EOS becomes stiffer than the quark phase and the hadronic phase in the crossover region indicated by the shaded band. Such stiffening is induced

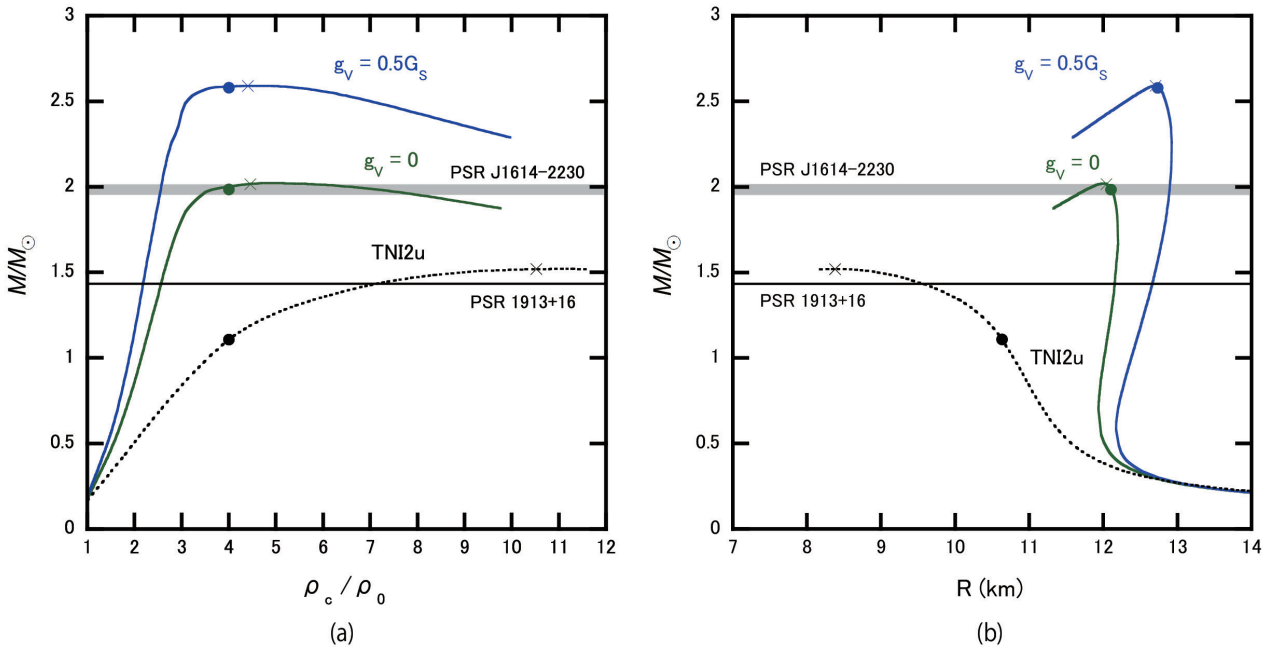

Figure 4.10: (a) $M-\rho_c$ relationships with the interpolated EOSs. We adopt the HK-parameter set for the Q-EOS with various $g_{_V}/G_{_S}=0,0.5$. The crossover window are fixed to be $(\bar{\rho},\Gamma)=(3\rho_0,\rho_0)$. The cross symbols denote the points of $M_{\max}$, while the filled circles denote the points beyond which the strangeness appears. The gray band denotes $M=(1.97\pm0.04)M_\odot$ for PSR J1614-2230. The solid black line denotes $M=1.44M_\odot$ for PSR 1913+16. (b) M-R relationships with the interpolated EOSs. These figures are taken from [3].

by the extra pressure in Eq. (4.10). Thus the maximum mass of the neutron star is expected to become large even for moderate value of $g_{_V}$ by comparing this v_S^2 with Fig. 4.7.

4.3.2 Bulk Properties of NSs

In Fig.4.10(a), we plot $M-\rho_c$ relationship between TNI2u for H-EOS and NJL Q-EOS for $g_{_V}/G_{_S}=0,0.5$ with HK parameter set. We choose the crossover window as $(\bar{\rho},\Gamma)=(3\rho_0,\rho_0)$. For comparison, the $M-\rho_c$ relationship only with TNI2u is also plotted by the dashed line. Fig.4.10(b) shows the corresponding $M-R$ relations. As anticipated from Fig. 4.9 (b), the maximum mass is larger than the case of the P-interpolation for given $g_{_V}$. The radius of NSs with ε-interpolated EOS is in (12.5 ± 0.5) km, which is slightly larger than that with P-interpolation due to the stiffness of the ε-interpolated EOS.

In Table 4.5, we show $M_{\max}$ and ρ_c for different H-EOS, vector type interaction $g_{_V}$ and choice of the crossover window parameterized by $\bar{\rho}$ and Γ. The ε-interpolation makes EOS stiff more drastically than the P-interpolation. Even for $(g_{_V},\bar{\rho})=(0,3\rho_0)$ and $(g_{_V},\bar{\rho})=(0.5,5\rho_0)$, the maximum mass $M_{\max}$ can exceed $1.97M_\odot$.

Table 4.5: $M_{\max}/M_\odot$ (ρ_c/ρ_0) for different choice of H-EOS, stiffness of Q-EOS and crossover window.

H-EOS	$g_V = 0$		$g_V = 0.5G_S$	
	$(\bar{\rho}, \Gamma) = (3\rho_0, \rho_0)$	$(5\rho_0, 2\rho_0)$	$(3\rho_0, \rho_0)$	$(5\rho_0, 2\rho_0)$
TNI2u	2.02 (4.5)	1.86 (8.7)	2.59 (4.4)	2.25 (6.1)
TNI2	2.02 (5.8)	1.84 (9.1)	2.59 (4.3)	2.23 (6.8)
TNI3u	1.99 (4.8)	1.89 (8.5)	2.57 (4.7)	2.26 (6.0)
TNI3	1.97 (5.8)	1.80 (6.3)	2.55 (4.5)	2.21 (7.3)
Paris+TBF	1.92 (4.8)	1.75 (6.5)	2.52 (4.7)	2.17 (6.5)
AV18+TBF	1.94 (4.7)	1.75 (7.2)	2.53 (4.7)	2.19 (6.1)
SCL3$\Lambda\Sigma$	1.85 (4.8)	1.73 (7.7)	2.46 (4.7)	2.15 (6.8)

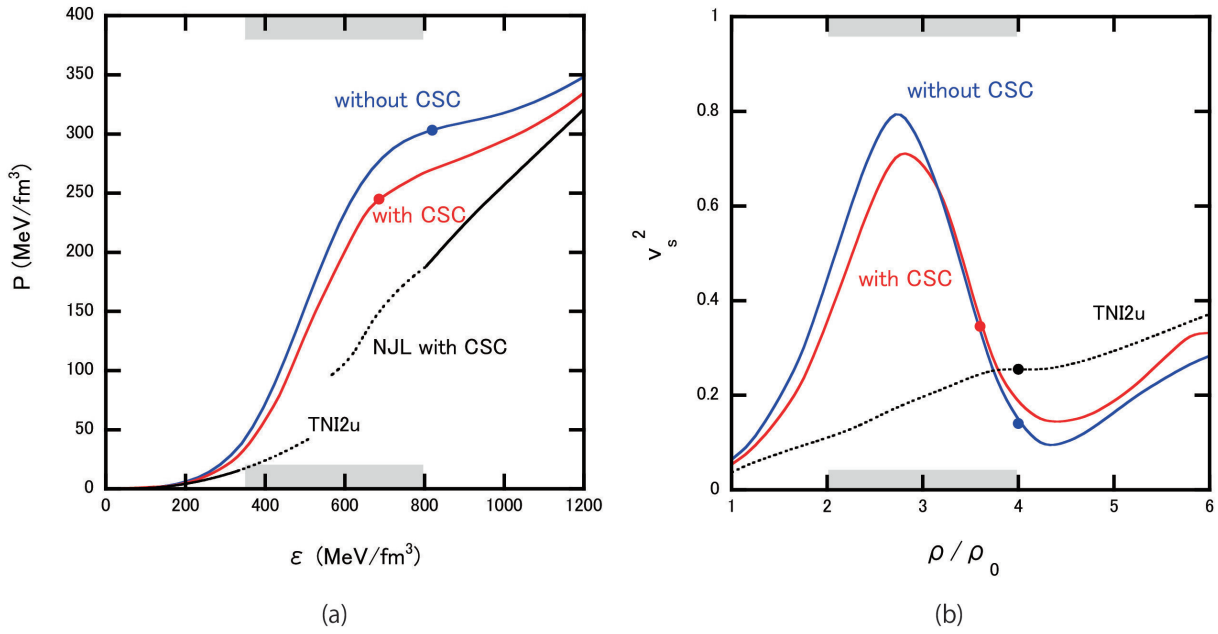

Figure 4.11: (a,b) Comparison between the CRover EOS and the sound velocity squared without CSC ($H = G'_D = 0$) and those with CSC ($H = G_S$ and $G'_D = G_D$) for $g_V/G_S = 0.5$. These figures are taken from [3].

4.4 Neutron Star Properties with ε-interpolation with CSC

In this section, we add the diquark channel with $H = G_S$ and $G'_D = G_D$. By turning on CSC, CRover-C EOS becomes a little bit softer than the case without CSC in the crossover region as

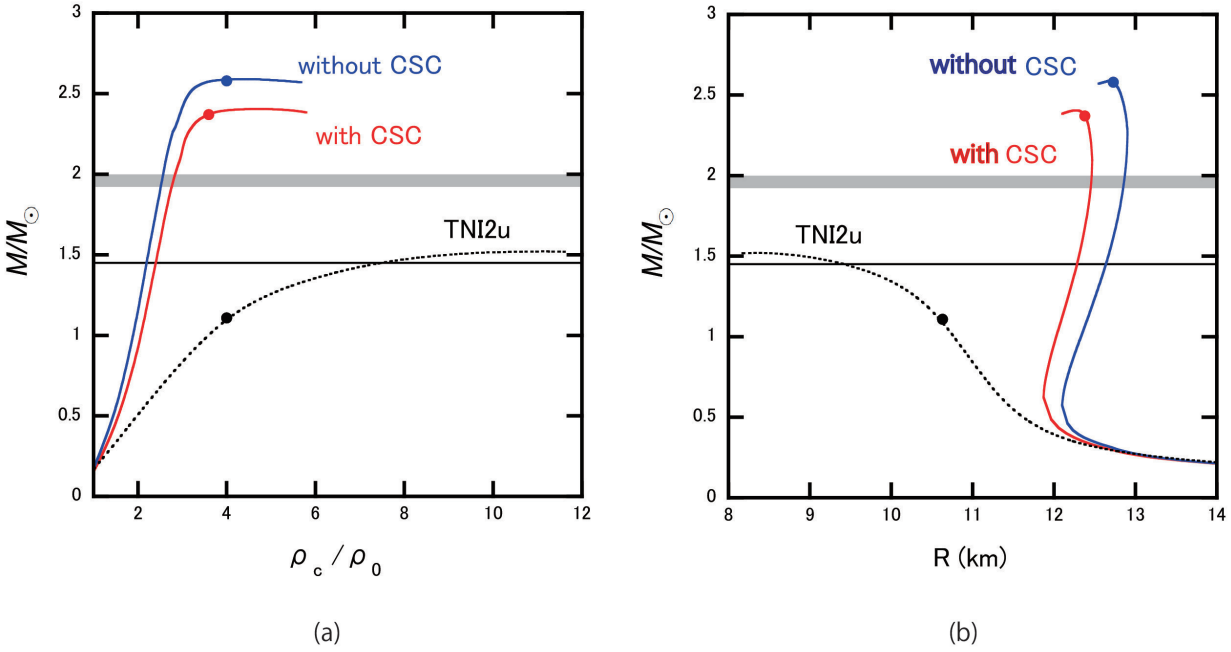

Figure 4.12: (a) The $M-\rho_c$ relations with the CRover EOS (solid lines) and TNI2u hadronic EOS (dotted line) with and without the CSC phase for $g_v/G_S = 0.5$. (b) The $M-R$ relation with the same EOSs as (a). These figures are taken from [3].

shown by the red lines in Fig.4.11 (a) pressure as a function of the energy density and (b) sound velocity squared v_S^2 as a function of baryon density. Associated with this, the onset density of the strangeness is reduced from $4\rho_0$ to $3.6\rho_0$ as shown by the solid circle. As we have discussed in Chapter 3, there is little room for the CFL phase to appear inside NSs in our CRover-C EOS, which is not considered in this figure.

In Fig. 4.12 (a,b), $M-\rho_c$ and $M-R$ relations are plotted by using the CRover-C EOS with and without CSC given in Fig.4.11(a). For comparison, the results of the TNI2u hadronic EOS are shown by the black dotted lines. As we have already discussed, the CSC softens the EOS. Then, the $M_{\rm max}$ of the NS with CSC becomes smaller by $0.2M_\odot$ than that without CSC phase. Such a reduction of $M_{\rm max}$ due to CSC is consistent with other calculations (see e.g., [112, 113]). However, the massive NSs with $2M_\odot$ can be still sustained by the interpolated EOS with CSC.

Two remarks are in order here about the effect of CSC on the $M-R$ relation: (i) The central density of the NSs does not exceed $4.9\rho_0$ in CRover EOS with CSC, so that the CFL phase barely appears inside the star. (ii) The effect of 2SC already becomes visible for low mass stars with the low central density . This is because we have a smooth interpolation between the hadronic EOS and quark EOS, so that the 2SC component has small but non-negligible contribution even in low densities. Physically, this could be interpreted as partial percolation of the nucleons into quarks with strong diquark correlations.

Table 4.6: $M_{\max}/M_\odot$ (ρ_c/ρ_0) for different choices of hadronic EOS, quark EOS. We fix $(\bar{\rho}, \Gamma)$ at $(3\rho_0, \rho_0)$.

	$g_V = 0$ without CSC	$g_V = 0.5G_S$ without CSC	$g_V = 0.5G_S$ with CSC
$(\bar{\rho}, \Gamma)$	$(3\rho_0, \rho_0)$	$(3\rho_0, \rho_0)$	$(3\rho_0, \rho_0)$
TNI2u	2.02 (4.5)	2.59 (4.4)	2.40 (4.9)
TNI2	2.02 (5.8)	2.59 (4.3)	2.40 (4.8)

Table 4.6 is a summary of the the maximum mass $M_{\max}$ and the central density ρ_c normalized by ρ_0 with the CRover-C EOS including CSC phase. Two sets of hadronic EOS (TNI2u and TNI2) are adopted, but the difference is small. The effect of CSC generally decreases $M_{\max}$ and increases ρ_c. As long as $\bar{\rho}$ is around $3\rho_0$, the CRover-C EOS can easily accommodate the $2M_\odot$ NSs.

4.5 Brief Summary

In this chapter, we introduced a phenomenological interpolation method between the hadronic phase and the quark phase at zero temperature on the basis of the smooth crossover. We call this EOS "CRover-C" EOS. We should note that thermodynamic relations are satisfied by our phenomenological EOS. Through the TOV equation, we can calculate bulk properties of cold NSs sustained by this CRover-C EOS. Due to the effects of the crossover, CRover-C EOS becomes stiff when the quark matter appears. This is in sharp contrast to the case of the first order transition. We showed this stiffness does not depend on the choice of H-EOSs and interpolation methods. Due to the stiffness of the interpolated EOS, the central density of NSs with crossover becomes much smaller than that without crossover. Therefore, if we have the universal repulsive three body force among hyperons, since the onset of the hyperon mixture delays, there is a possibility that our interpolated EOS solves the well-known rapid cooling problem with hyperons. Finally, we consider the effects of CSC on NSs. CSC makes EOS soft so that the maximum mass of NSs with CSC is smaller by about $0.2M_\odot$ than that without CSC. Interpolated EOSs including CSC can still sustain $2M_\odot$ NSs. Due to the partial percolation of nucleons to quarks, in our model, CSC has a small but non negligible effects even in low mass NSs.

Chapter 5

Hot Neutron Stars with Crossover

In this chapter, we discuss the bulk properties of hot NSs, which come from the contraction after the core-collapsed Type-II supernova explosion. To discuss the effect of the hadron-quark crossover on the hot NSs, we generalize the previous crossover model at zero temperature to the finite temperature region naturally. By using this new phenomenological EOS, we calculate the mass, radius and the temperature profiles about hot NSs. The discussions of this chapter are based on [3, 4].

5.1 Hot Neutron Stars

After the core-collapsed Type-II supernova explosion, a hot NS with the radius $\sim 10-20$ km emerges if the mass is so small that a proto NS does not evolve into a BH[34, 35, 36]. Since in hot NSs the neutrino trapping occurs at the baryon density ρ exceeding $10^{12}\mathrm{g/cm}^3$, the hot NS at birth in quasi-hydrostatic equilibrium is composed of the supernova matter with the typical lepton fraction, $Y_l = Y_e + Y_\nu \sim 0.3 - 0.4$, and the typical entropy per baryon, $\hat{S} \sim 1 - 2$.

Of course, cold NSs give us the rich information about dense QCD matter as we have already mentioned, the hot NSs also provide us with various information on the properties and dynamics of high density matter. Thermal properties of the hot NSs are intimately related to the physics of high density matter at finite temperature. We note that the hot neutron stars with the hadron-quark mixed phase has been studied previously, e.g. [114, 115, 116, 117]. Such a mixed phase generally leads to soft EOS, so that it is rather difficult to sustain $2M_\odot$ NSs as we have already discussed in Chapter 2. On the contrary, our hadron-quark crossover approach does not suffer from the problem, since it leads to stiff EOS in the crossover region shown in Chapter 4. The purpose of this chapter is to study the hot neutron star at birth with degenerate neutrinos on the basis of smooth percolation picture from the hadronic phase to quark phase.

In Fig.5.1, we show a schematic picture, which compares the internal structure of the hot and cold NSs with $2M_\odot$. Above the normal nuclear matter density ρ_0, we use the EOS interpolated between hadronic phase and quark phase. On the other hand, below ρ_0, we use the thermal

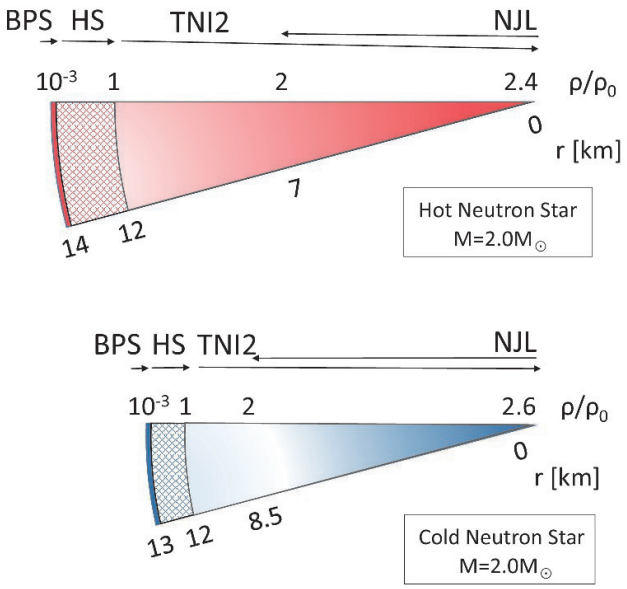

Figure 5.1: Comparison between the hot NS and cold NS with $M = 2M_\odot$ obtained by the CRover EOS with $g_V = 0.5G_S$. We take $(Y_l, \hat{S}) = (0.3, 1)$ to characterize the hot NS. As for the details of the EOSs adopted at different densities, BPS, HS, TNI2 and NJL, see the text. This figure is taken from [4].

EOS which consists of an ensemble of nuclei and interacting nucleons in nuclear statistical equilibrium given by Hempel and Schaffner-Bielich (HS EOS) [118]. As the density decreases, the temperature also decreases monotonically: For example, $T \sim 10$ (2) MeV at ρ=0.1 (0.001) fm^{-3} for $(Y_l, \hat{S}) = (0.3, 1)$. Other EOSs in this region do not show quantitative difference from the HS EOS as discussed in [119]. Once the baryon density becomes smaller than the neutron drip density $10^{-3}\rho_0$, the temperature becomes smaller than 0.1 MeV. Then we switch to the standard BPS EOS [19].

5.2 Crossover at Finite Temperature

There are some important differences between the cold matter and the supernova matter.

- The diffused Fermi surface due to the effect of finite T.
- The existence of degenerate neutrinos.
- The contributions from anti-particles.

The main purpose of this chapter is to see the differences between the cold EOS and the hot EOS with crossover. Therefore, in the following, we fix the typical crossover density $\bar{\rho}$ and the typical width of the crossover Γ at $(3\rho_0, \rho_0)$. We also fix the magnitude of the flavor independent four Fermi vector type interaction at $g_V = 0.5G_s$.

We neglect the strangeness in the hadronic matter since the typical threshold density for the strangeness in the hadronic matter is almost the same or larger than the typical crossover density $\bar{\rho} = 3\rho_0$. Also, we neglect muons since muons are irrelevant for the stiffness of EOS. Under these assumptions, we consider a system composed of n, p, e^-, e^+, ν_e and $\bar{\nu}_e$ in the hadronic EOS (TNI2) at finite T, and u, d,s, e^-, e^+, ν_e and $\bar{\nu}_e$ in the quark EOS (NJL) at finite T. We construct EOSs in the mean field approximation with the charge neutrality, chemical equilibrium and baryon and lepton number conservations. In practice, we find $\mu_e/T > 15$ in the interior of the hot NSs, so that the effects of anti-particles, e^+ and $\bar{\nu}_e$, and neutrinos in second and third generations are negligibly small. The color superconductivity is switched off for simplicity.

To generalize the ε-interpolation method to the finite temperature region naturally, we suggest the phenomenological interpolation of the Helmholtz free-energy per baryon $\hat{F} = F/N = \hat{E} - T\hat{S}$ to describe the smooth interpolation between the hadronic matter and the quark matter at finite T. $\hat{F}$ is a function of ρ, T and Y_l, so that we have

$$\hat{F}(\rho, T; Y_l) = \hat{F}_{\rm H}(\rho, T; Y_l) w_-(\rho, T) + \hat{F}_{\rm Q}(\rho, T; Y_l) w_+(\rho, T). \tag{5.1}$$

Here $\hat{F}_{\rm H}$ and $\hat{F}_{\rm Q}$ are the hadron+lepton free-energy per baryon and the quark+lepton free-energy per baryon, respectively. Of course, in the case of the supernova matter, the weight function $w_\pm$ depend on both the density and the temperature. However, the typical temperature of hot NSs is about 30MeV which is sufficiently smaller than the thermal dissociation temperature of hadrons of about 200 MeV, which is already known by the lattice QCD Monte Carlo simulation. Therefore, we ignore the T-dependence of these weight functions $w_\pm$,

$$w_\pm(\rho, T) \to w_\pm(\rho) \equiv \frac{1 \pm \tanh(\rho - \bar{\rho})/\Gamma}{2}. \tag{5.2}$$

As a result, the resultant Helmholtz free-energy per baryon $\hat{F}$ can be written as the following form,

$$\hat{F}(\rho, T; Y_l) = \hat{F}_{\rm H}(\rho, T; Y_l) w_-(\rho) + \hat{F}_{\rm Q}(\rho, T; Y_l) w_+(\rho). \tag{5.3}$$

The entropy per baryon $\hat{S} = -\partial\hat{F}/\partial T$ and the energy per baryon $\hat{E} = \hat{F} + T\hat{S}$ are obtained by using the thermodynamic relations,

$$\hat{S} = -\partial\hat{F}/\partial T, \tag{5.4}$$

$$\hat{E} = \hat{F} + T\hat{S}. \tag{5.5}$$

Under the assumption that $w_\pm$ is T-independent, Eq.(5.3) leads to

$$\begin{aligned} \hat{S}(\rho, T; Y_l) &= \hat{S}_{\rm H}(\rho, T; Y_l) w_-(\rho) + \hat{S}_{\rm Q}(\rho, T; Y_l) w_+(\rho), \\ \hat{E}(\rho, T; Y_l) &= \hat{E}_{\rm H}(\rho, T; Y_l) w_-(\rho) + \hat{E}_{\rm Q}(\rho, T; Y_l) w_+(\rho). \end{aligned}$$

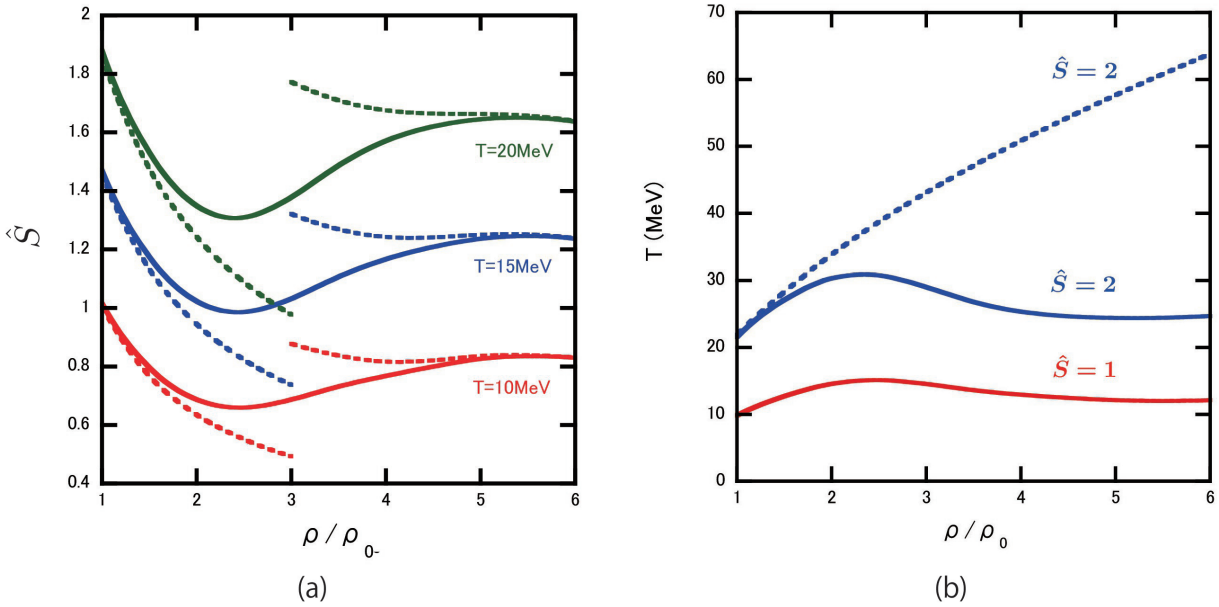

Figure 5.2: (a) The entropy per baryon $\hat{S}$ as a function of the baryon density ρ for $Y_l = 0.3$ with T=10 MeV (red), 15 MeV (blue) and 20 MeV (green). Solid lines correspond to the cases with crossover. Dotted lines at low and high density regions come from the hadronic and the quark phase respectively. (b) The temperature T of the isentropic matter as a function of the baryon density ρ for $Y_l = 0.3$ with $\hat{S} = 1$ (red) and $\hat{S} = 2$ (blue). Solid lines and the dashed line correspond to the cases with crossover and without crossover, respectively. These figure are taken from [4].

The thermodynamic quantities for isothermal matter with ρ, T and Y_l can be converted into those for isentropic matter by means of the T-ρ relationship constrained by the constant entropy per baryon, $\hat{S}$ =const. Then the isentropic pressure P and the isentropic baryon chemical potential $\mu_{_B}$ are obtained as

$$P(\rho, T(\rho); Y_l, \hat{S}) = -\left.\frac{\partial E}{\partial V}\right|_{S,N} = \rho^2 \left.\frac{\partial \hat{E}}{\partial \rho}\right|_{\hat{S}}, \tag{5.6}$$

$$\mu_{_B}(\rho, T(\rho); Y_l, \hat{S}) = \left.\frac{\partial E}{\partial N}\right|_{S,V} = \left.\frac{\partial \varepsilon}{\partial \rho}\right|_{\hat{S}} \tag{5.7}$$

where $\varepsilon \equiv \rho \hat{E}$ is the energy density. From the definition of our interpolation method Eq. (5.3), P and $\mu_{_B}$ approach those of pure hadronic (quark) matter in the low (high) density limit.

5.3 Construction of Hot EOS

In the following, we consider typical values of the lepton fraction $Y_l = 0.3, 0, 4$ and those of the entropy per baryon $\hat{S} = 1, 2$. To carry out the conversion from the isothermal matter with

fixed T and Y_l to the isentropic matter with fixed $\hat{S}$ and Y_l, firstly we calculate $\hat{S}(\rho, T, Y_l)$ as a function of ρ/ρ_0.

In Fig.5.2 (a), we show $\hat{S}$ for T=10, 15, 20 MeV and $Y_l = 0.3$ with crossover by the solid lines, while the entropy per baryon for the pure hadronic matter and the pure quark matter are shown by the dashed lines. One finds that the entropy per baryon turns out to increase at high densities, once the quark degrees of freedom start to appear. By imposing the isentropic condition, we can make the relation between the temperature T and the density ρ/ρ_0 as shown in Fig.5.2 (b). Fig.5.2 (b) shows the temperature as a function of ρ/ρ_0 under isentropic conditions for $\hat{S} = 1, 2$ and $Y_l = 0.3$ with crossover (solid lines) and for $\hat{S} = 2$ and $Y_l = 0.3$ without crossover (the dashed line).

The rapid increase of $\hat{S}$ given T in the crossover region as shown in Fig. 5.2 (a) can be understood as follows. First of all, the temperature is enough smaller than the Fermi energy at high densities, so that the low T expansion (the Sommerfeld expansion) is applicable. Then, let us consider, for illustrative purpose, the non-relativistic neutron matter in the hadronic phase and the massless u-d quark matter with β-equilibrium in the quark phase. The ratio of the entropy per baryon of the hadronic matter ($\hat{S}_H$) and that of the quark matter ($\hat{S}_Q$) for non-interacting case can be evaluated in the leading order of the Sommerfeld expansion as, $\frac{\hat{S}_Q}{\hat{S}_H} \sim 1.14 \frac{g_Q^{1/3}}{g_H^{2/3}} \left(\frac{\rho}{\rho_0}\right)^{1/3}$. Here, the fractional powers originate from the difference between relativistic and non-relativistic kinematics. Note that the right hand side is T-independent. By taking the number of degrees of freedom, $g_Q = 2_{\rm spin} \times 3_{\rm color}$ and $g_H = 2_{\rm spin}$, as well as the typical crossover density $\rho = 3\rho_0$, the ratio becomes 1.88. This essentially explains the jump between the two dashed lines in Fig. 2.3 (a) for given T. Because of the fact that $\hat{S}$ given T with the crossover (the solid line in Fig.5.2 (a)) becomes larger than $\hat{S}_H$ without the crossover, there is no need to increase T to keep $\hat{S}$ constant at high densities. This can be indeed seen from Fig. 5.2 (b) in which T is rather insensitive to ρ for fixed $\hat{S}$.

In Fig.5.3(a), (b), (c) and (d), we show the isentropic pressure $P(\rho, T(\rho), Y_l)$, the energy per baryon $\hat{E}(\rho, T(\rho), Y_l)$, the baryon chemical potential $\mu_{_B}$ as functions of ρ, and the $P - \varepsilon$ relation, respectively, for three characteristic sets, $(Y_l, \hat{S}) = (0.3, 1), (0.3, 2)$ and $(0.4, 1)$. For comparison, the EOS of cold neutron star matter ($T = 0$ without neutrino degeneracy) is also shown by the black solid lines. In the following, we call this new phenomenological EOS on the basis of hadron-quark smooth crossover as "CRover-H EOS".

5.4 Bulk Properties of Hot Neutron Stars

Now, by using the CRover-H EOS in the last section, we can solve the TOV equation to obtain the structure of hot NSs at birth; In the following, we consider the hot neutron stars with typical values, $(Y_l, \hat{S}) = (0.3, 1)$.

In Fig. 5.4 (a), we show the relation between the gravitational mass M and the baryon

number N_B for hot and cold NSs with and without crossover. First of all, the crossover leads to heavier NSs due to the stiffening of the EOS as shown by the case of the cold NSs. Furthermore, hot NSs have larger mass than the cold ones for given N_B. Moreover, the maximum N_B for hot NS is smaller than that of the cold NS. This fact means that if there is no accretion so that the baryon number N_B is a constant through the thermal evolution, there is no configuration, which collapses to BH. With the present hadron-quark crossover, the hot EOS is slightly softer

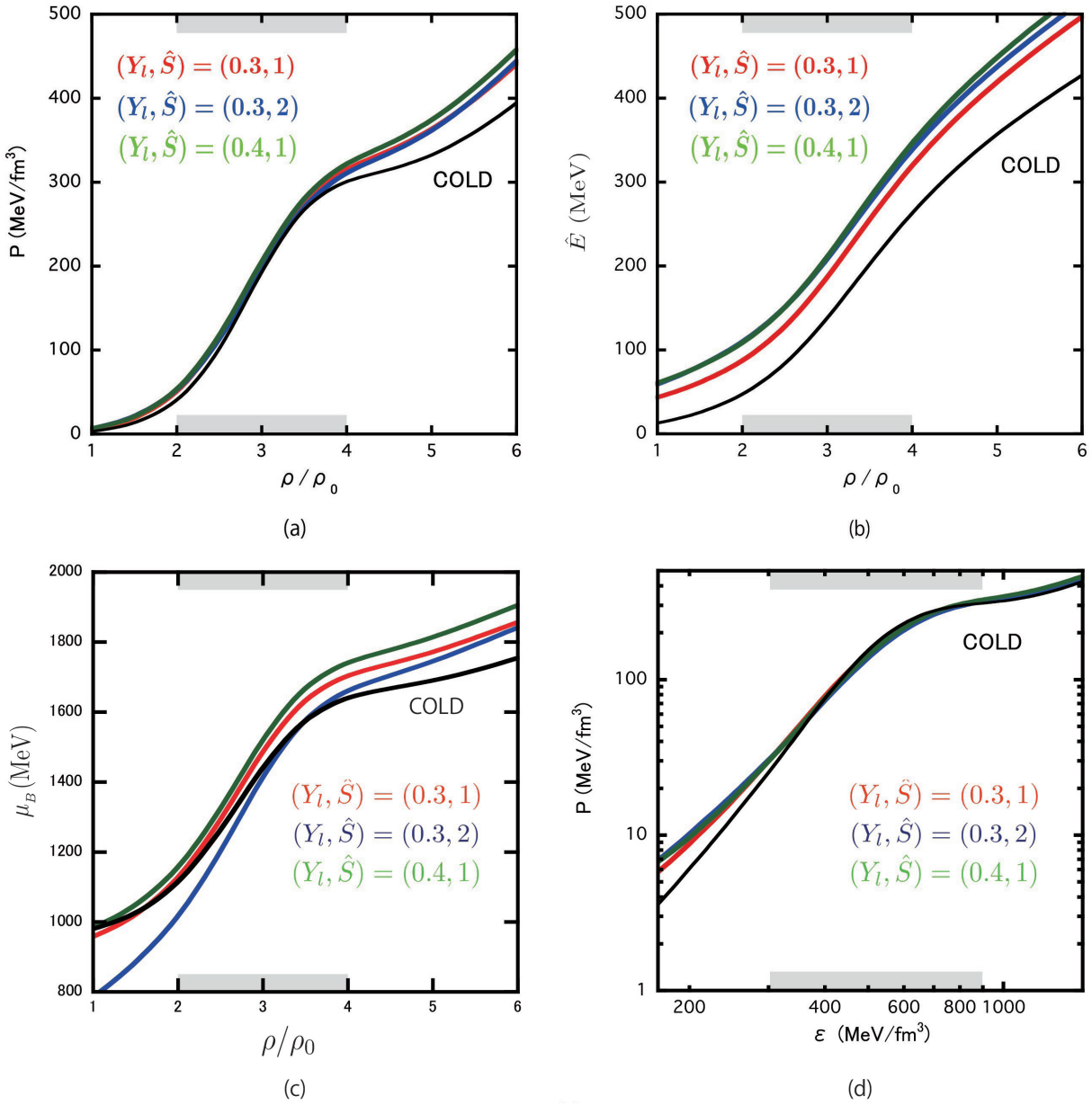

Figure 5.3: (a) The isentropic pressure P as a function of baryon density ρ for $(Y_l, \hat{S})$ =(0.3, 1), (0.3, 2) and (0.4, 1). The black line corresponds to the EOS for cold neutron star matter. The crossover window is shown by the shaded area on the horizontal axis. (b) The energy per baryon $\hat{E}$ with the same set of Y_l and $\hat{S}$ as (a). (c) Baryon chemical potential μ_B as a function of ρ. (d) P as a function of ε. These figures are taken from [4].

than the cold EOS in the crossover region as shown in Fig.5.3(d), so that the delayed collapse of the hot NSs to the black hole does not take place. We will discuss the reason why this softening occurs later. On the other hand, with the first-order hadron-quark phase transition, the softening of the EOS due to the mixed phase is tamed by the finite temperature effect, so that the hot NSs may eventually collapse into black holes [114, 116]. The possibility of the delayed collapse has been also reported in the context of the pion condensation [32]. In Fig. 5.4 (b), we show ΔE in the unit of $M_\odot$ as a function of the mass of cold neutron star, $M_{\rm cold}$. Typical energy release $\Delta E \equiv M_{\rm hot} - M_{\rm cold}$ for $M_{\rm cold} = 1.4 M_\odot$ due to the contraction reads

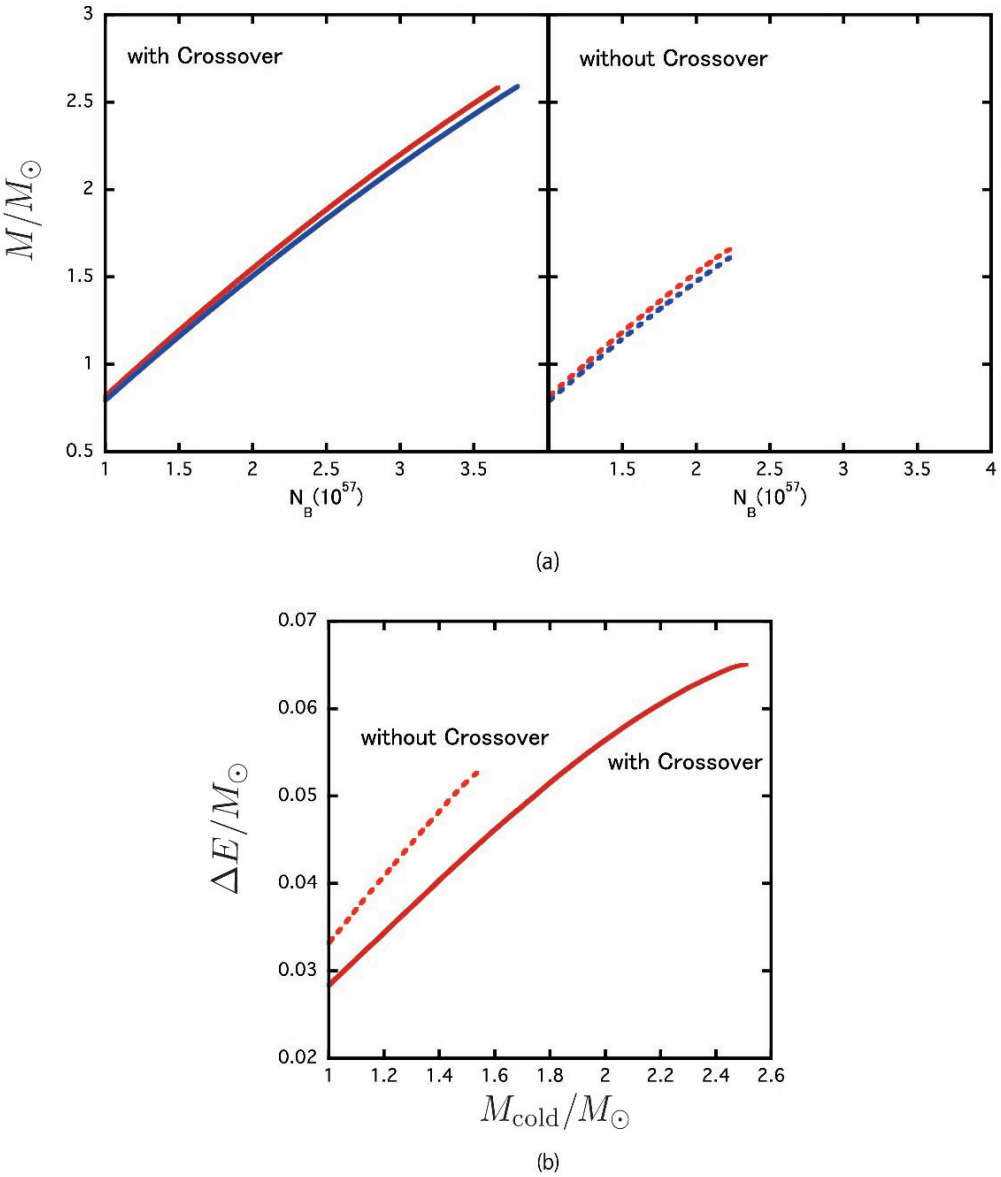

Figure 5.4: (a) The neutron star mass M as a function of the total baryon number N_B. Red (blue) curves correspond to the hot (cold) neutron stars with crossover. The dotted lines correspond to the case without crossover. (b) The energy release $\Delta E \equiv M_{\rm hot} - M_{\rm cold}$ as a function of the cold NS mass $M_{\rm cold}$. $(Y_l, \hat{S}) = (0.3, 1)$ is adopted. These figures are taken from [4].

$\Delta E \sim 0.04 M_\odot$. By assuming the conservation of angular momentum through the thermal evolution, we can estimate the spin-up rate. In this case, the spin-up rate is about 14 % for $M_{\rm cold} = 1.4 M_\odot$ of evolved cold neutron stars.

In Fig. 5.5 (a), the mass-radius (M-R) relations of the hot and cold neutron stars with hadron−quark crossover are shown. Although the maximum masses are similar between hot and cold NSs, the stiffening of the EOS at finite T at low density (see Fig. 5.3 (d)) makes the hot NS bigger in size, especially for NSs with small M. On the other hand, a slight softening of the EOS at finite T in the crossover region (see Fig. 5.3 (d)) leads to the maximum mass of the hot neutron star slightly smaller than that of the cold neutron star.

This is somewhat counter intuitive since the EOS with neutrinos at finite T usually becomes stiffer due to the thermal pressure from constituent particles and the degenerate pressure from neutrinos. However, it should be remembered that we are considering the isentropic situation (fixed $\hat{S}$) rather than the isothermal situation (fixed T). To see the difference, a schematic illustration of the EOSs at fixed T (the black solid lines) and the EOS at fixed $\hat{S}$ (the red line) is given in Fig. 5.6 (a). The black solid lines become stiffer as T increases. On the other hand, due to the decrease of T around the crossover region (see Fig. 5.2(b)), the red line (the isentropic EOS) can even become slightly softer than the EOS at T=0 in the crossover region. Such a slight softening can be seen quantitatively by the ratio of the sound velocities, $(v_S^{\rm hot} - v_S^{\rm cold})/v_S^{\rm cold}$, as shown in Fig. 5.6(b) drawn on the basis of our CRover EOS: The sound velocity ratio (the blue line) becomes negative associated with the decrease of T (the red line)

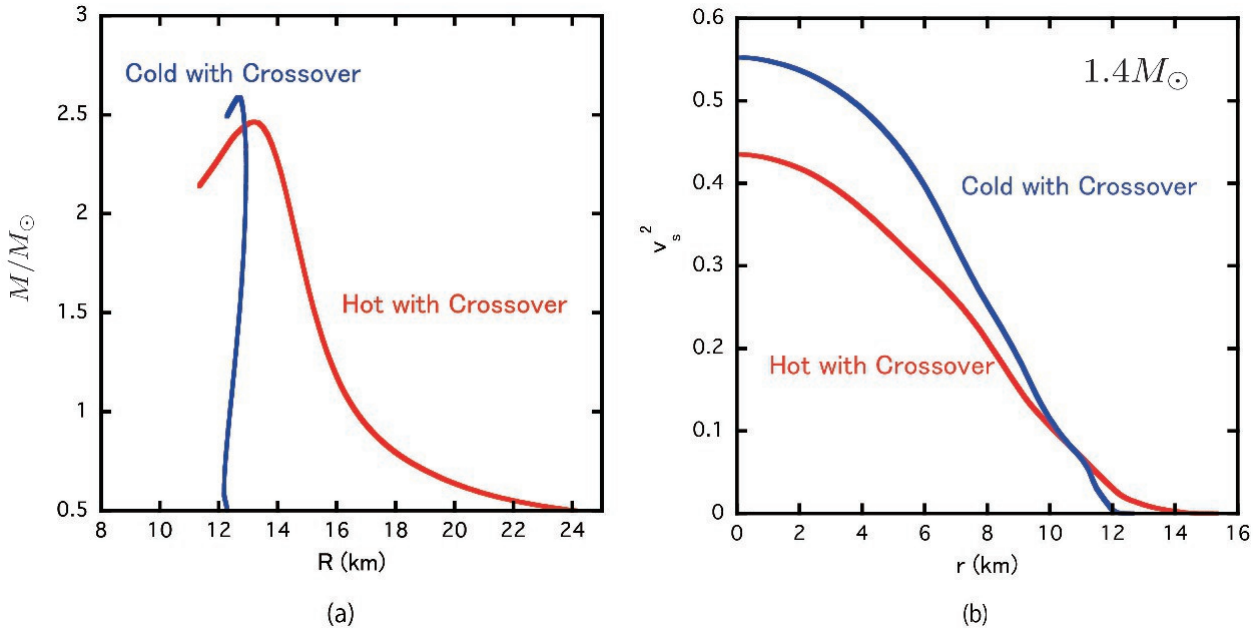

Figure 5.5: (a) Mass-radius relationship for $(Y_l, \hat{S}) = (0.3, 1)$. Red: hot neutron stars with crossover. Blue: cold neutron stars with crossover. (b) The sound velocity squared v_s^2 as a function of the distance from the center of $1.4 M_\odot$ neutron star. Colors on each line are the same as in (a). These figures are taken from [4].

in the crossover region.

In Fig.5.5 (b), we plot the local sound velocity squared $v_s^2(r)$ as a function of the distance from the center r for $M = 1.4M_\odot$, which is defined by

$$v_s^2(\rho; Y_l, \hat{S}) = \left.\frac{\partial P}{\partial \varepsilon}\right|_{Y_l,\hat{S}} = \left.\frac{dP(\rho, T(\rho); Y_l, \hat{S})/d\rho}{d\varepsilon(\rho, T(\rho); Y_l, \hat{S})/d\rho}\right|_{Y_l,\hat{S}} \tag{5.8}$$

with $\rho(r)$ obtained through the TOV equation. As we have demonstrated at $T = 0$ in Chapter 4, v_s^2 becomes large in the crossover region. The sound velocity for cold neutron star is larger (smaller) at higher (lower) density than that of the hot neutron star. We note that the sound velocity decreases towards the neutron star surface simply because the baryon density decreases.

In Fig. 5.7(a) and (b), the central temperature $T_{\rm cent}$ and the central density $\rho_{\rm cent}$ of the hot NSs with and without the crossover are plotted as a function of M. The temperature decreases due to the appearance of the quark degrees of freedom (see Fig.5.2(b)), so that the central temperature becomes significantly smaller with crossover as shown in Fig. 5.7(a). The central density of the NSs becomes significantly smaller with crossover as shown Fig. 5.7(b) due to the fact that the crossover EOS becomes stiffer than EOS without crossover.

To compare the internal structure of the hot NS with and without the crossover in terms of the temperature and density, we plot $T(r)$ and $\rho(r)$ in Fig. 5.8 (a) and (b), respectively. Here we consider the hot NS with a canonical mass $M = 1.4M_\odot$. Under the presence of the

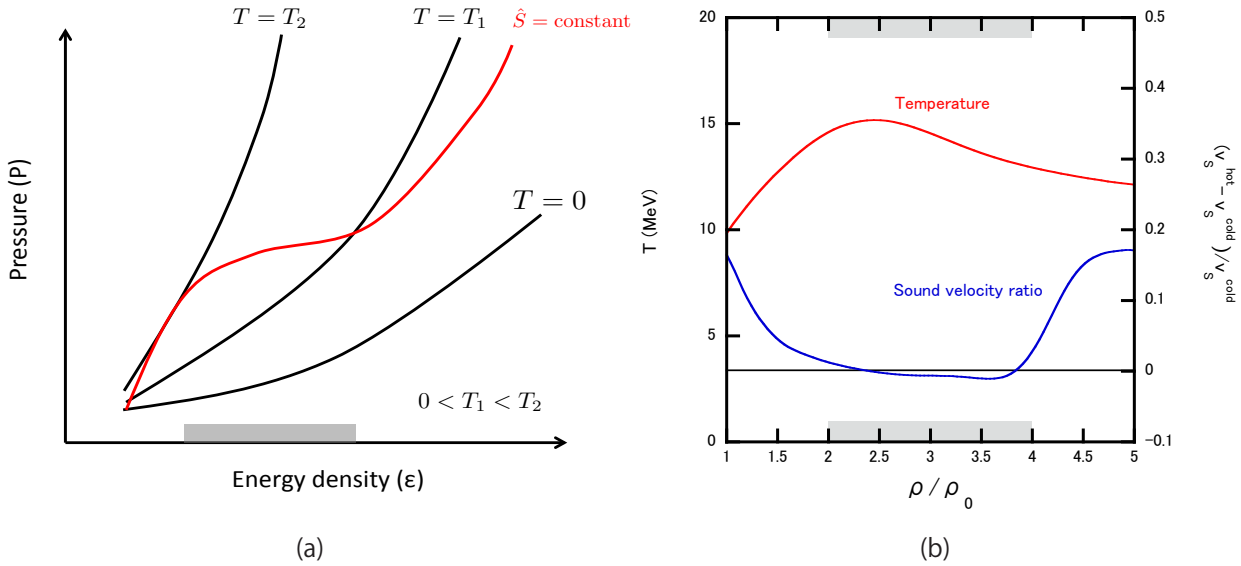

Figure 5.6: (a) The schematic illustration for EOSs at fixed T and fixed $\hat{S}$ by black lines and the red curve. The shaded area in the horizontal axis is the crossover region. T decreases in this region. The red line becomes slightly softer than the black line with $T = 0$ in the crossover region. (b) The temperature (red line) and the sound velocity ratio defined by $(v_s^{\rm hot} - v_s^{\rm cold})/v_s^{\rm cold}$ with $(Y_l, \hat{S}) = (0.3, 1)$ as a function of the baryon density. The shaded area in the horizontal axis is the crossover region. The sound velocity ratio becomes negative in the crossover region.

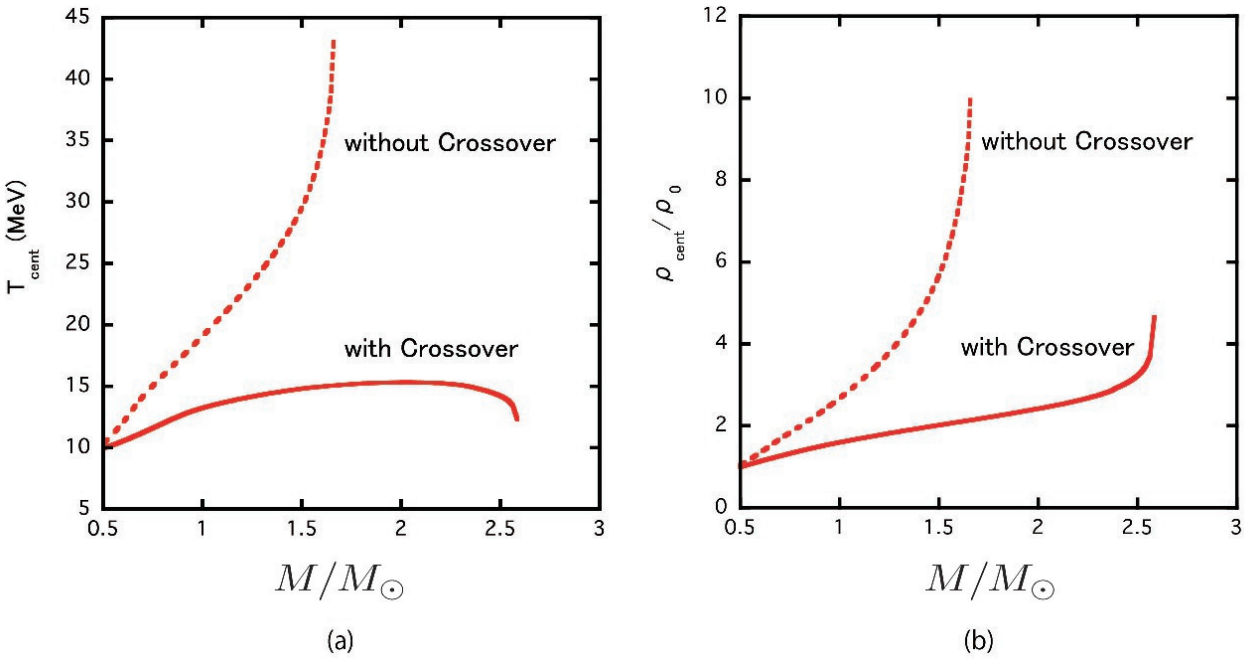

Figure 5.7: (a) The central temperature $T_{\rm cent}$ as a function of M. (b) The central density $\rho_{\rm cent}$ as a function of the neutron star mass M. The solid (dashed) lines correspond to the EOS with (without) crossover, and $(Y_l, \hat{S}) = (0.3, 1)$ is taken. These figures are taken from [4].

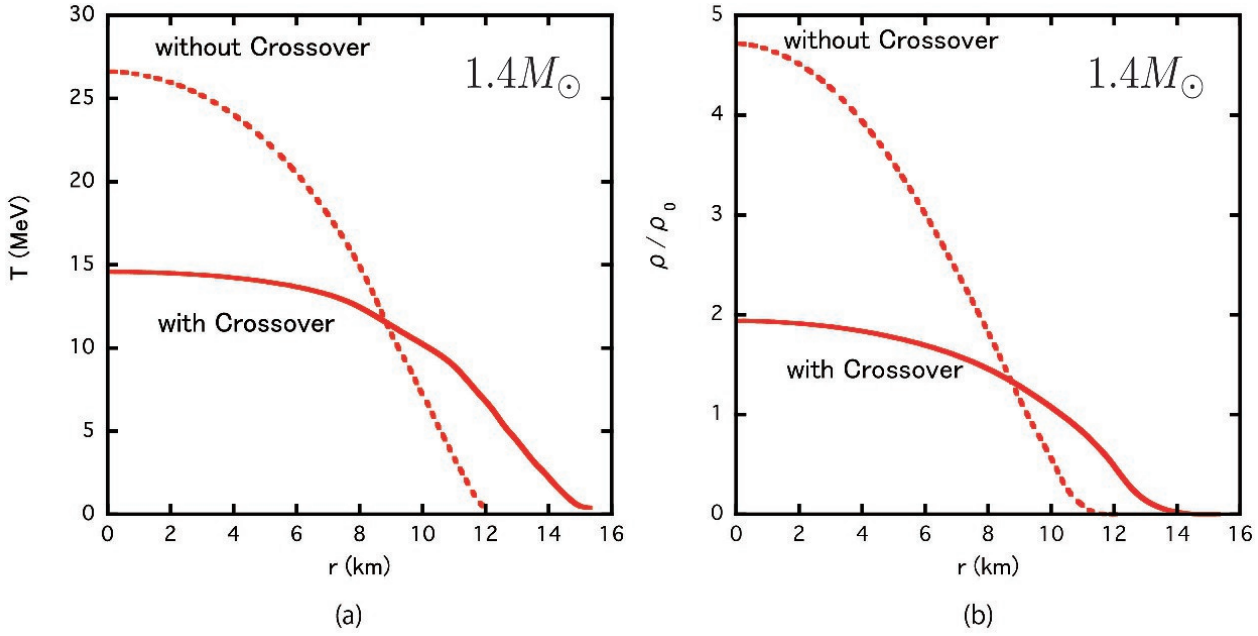

Figure 5.8: (a) The temperature profiles of the hot neutron star with $M = 1.4M_\odot$ and $(Y_l, \hat{S}) = (0.3, 1)$. Solid (dashed) lines correspond to the EOS with crossover and without crossover respectively. (b) The density profiles of the same neutron star as the case (a). These figures are taken from [4].

hadron−quark crossover, the crossover EOS becomes stiffer and hence the central density is smaller, so that the temperature and density profiles of the star are more uniform as compared

to those without the crossover.

5.5 Brief Summary

In this chapter, we have discussed the properties of hot NSs at birth on the basis of a new "CRover-H" EOS for supernova matter with hadron-quark crossover. Such a crossover leads to the EOS stiff enough to sustain $2M_\odot$ neutron stars as the case of "CRover-C" EOS, which is the phenomenological interpolated EOS on the basis of the smooth crossover at zero temperature. A noticeable point is that the crossover plays important roles not only to generate the stiff EOS but also to lower the internal temperature of hot neutron stars. Such suppression of temperature originates from a combined effect of the isentropy nature of the supernova matter and larger entropy for given temperature due to the quark degrees of freedom. Given baryon number, hot neutron stars have larger radius and larger gravitational mass caused by the high lepton fraction and the thermal effect. This suggests that, during the contraction from hot to cold stars, gravitational energy is released and simultaneously the spin-up takes place. In the present study, the released energy is about 0.04 $M_\odot$ and the spin-up rate is about 14 % (assuming the conservation of angular momentum) for $M_{\rm cold} = 1.4M_\odot$ of evolved cold neutron stars. It is worth noting here that the maximum baryon number $N_{\rm max}$ is smaller for the hot neutron star if there is a crossover. This implies that there could be massive neutron stars which can be reached only by the mass accretion after the birth.

Chapter 6

Summary and Discussion

Motivated by the recent observation of the massive neutrons stars with $2M_\odot$, we study the possible fate of the quark matter inside the NSs on the basis of a picture of hadron-quark crossover.

After the general introduction of high density QCD and neutron stars in Chapter 1, we have discussed the hadronic EOS with and without hyperons on the basis of the phenomenological 2-body and 3-body baryon interactions in Chapter 2. We showed the hyperon mixture makes hadronic EOSs soft and $2M_\odot$ NSs cannot be sustained even with the universal 3-body repulsions among baryons. We called this conflict between the observation of the massive NS with $2M_\odot$ and the hyperon mixture predicted by the nuclear theory as the "hyperon puzzle".

Then, in Chapter 3 we discussed the quark EOS which would play an important role at high baryon densities. Since the system in the core of NSs does not reach the asymptotic region where pQCD can be applied, we employed the $(2+1)$-flavor NJL model as an effective theory of QCD to describe the strongly interacting quark matter. The NJL model includes the two non-perturbative aspects of QCD, the chiral condensate induced by the strong $\bar{q}q$ correlation and the color superconductivity (CSC) induced by the strong qq correlation. We showed how the partial restoration of the chiral condensate and the diquark condensate evolve as a function of the baryon density in this model. As a result, if we take a relatively strong diquark coupling constant, 2-flavor color superconducting phase is shown to emerge at the densities relevant to the NS interior.

In Chapter 4, we examined the intermediate density region where neither the description by point-like hadrons nor that by weakly interacting quarks are reliable. On the basis of the percolation picture of hadrons in this region, we introduced a phenomenological interpolation method between the hadronic phase and the quark phase at zero temperature We called this EOS "CRover-C" EOS. Then, we estimated the bulk properties of cold NSs with this CRover-C EOS. Due to the effects of the crossover, CRover-C EOS becomes sufficiently stiff so that it can sustain $2M_\odot$. This fact is in contrast to the case of the first order transition, in which EOSs become softer due to the transition to quark matter. The radius of NSs with the $P(\varepsilon)$-interpolated EOS turns out to be in about (11 ± 1)km and (12.5 ± 0.5) km depending on the

interpolation methods, and is consistent with the recent estimations from qLMXB and PRE X-ray bursts. We also discussed the internal structure of NSs: Our crossover model has a possibility to solve the rapid cooling due to the hyperon mixture if the onset of the hyperon mixture is delayed by the universal repulsive force between hyperons. The effects of CSC on bulk properties of NSs are also discussed. CSC makes EOS soft by about $0.2M_\odot$. However, the interpolated EOS with CSC still can sustain $2M_\odot$. Also, we found that CSC has non-negligible effects even in low mass NSs in the case of smooth crossover.

Finally, in Chapter 5 we extended the phenomenological EOS at zero temperature to finite temperature to examine the properties of the hot NSs at birth characterized by the constant lepton fraction and constant entropy per baryon due to the neutrino trapping. We constructed a phenomenological EOS at finite temperature called as CRover-H EOS by imposing the constant entropy per baryon and the constant lepton fraction conditions. We checked this CRover-H EOS is sufficiently stiff so that $2M_\odot$ can be sustained. Then, we found that the hadron-quark crossover plays an important role to lower the central temperature of hot neutron stars in comparison to the case of hadronic EOS. This suppression of temperature comes from the presence of the quark degrees of freedom in the crossover region. At a given baryon number, hot neutron stars have generally larger radius and larger gravitational mass caused by the high lepton fraction and the thermal effect. This suggests that, during the contraction from hot NS to cold NS, gravitational energy is released and simultaneously the spin-up takes place. The released energy is shown to be about 0.04 $M_\odot$ and the spin-up rate is about 14 % (assuming the conservation of angular momentum) for $M_{\rm cold} = 1.4M_\odot$ of evolved cold neutron stars. On the other hand, the maximum total baryon number of hot NSs is smaller than that of cold NSs since the internal temperature decreases in the crossover region. This means there is no configuration to collapse into BHs if there is no accretion. Although there is no significant difference of the maximum mass between hot and cold NSs, the radius of hot NSs is much larger than that of cold NSs since hot EOS is harder than cold EOS at low density region due to the lepton and thermal effects.

There are several directions for future works. Firstly, extension of the present phenomenological model to higher temperature region is very important to survey the hadron-quark crossover effects on the neutron star mergers and supernovae. Secondly, the application of our CRover EOS to low-energy heavy ion collisions would be important to test the validity of the crossover picture. The compressibility of usual hadronic matter and that of CRover EOS are very different, so that the hadronic flows and the meson productions from heavy ion collisions could be good observables to differentiate between the crossover and the first-order transition.

The hadron-quark crossover turns out to have interesting phenomenological implications to the key issues of the neutron stars, such as the massive neutron stars and hyperon puzzle, the universal radius of the neutron stars, temperature and density profiles inside the hot neutron stars, and so on. One of the most important and yet challenging theoretical problems is to elucidate the QCD basis of the phenomenological hadron-quark crossover introduced in this

thesis.

Acknowledemets

I express my sincere gratitude to my supervisor Prof. Tetsuo Hatsuda for fruitful discussions, valuable advices and careful reading of this manuscript. I am also grateful to Prof. Tatsuyuki Takatsuka. He led me to this neutron star physics, taught me the history and gave me the great discussion. I acknowledge Prof. Muneto Nitta for useful discussions and collaborations on the topological properties of superfluid phase in neutron stars. I thank Prof. M. Alford, Prof. G. Baym, Prof. K. Itakura, Dr. T. Kanazawa, Dr. T. Kojo, Prof. T. Mizushima, Prof. A. Ohnishi, late Prof. R. Tamagaki, Mr. Y. Tanizaki, Prof. T. Tatsumi, and Prof. W. Weise for helpful discussions. I also thank all members of the quantum hadron physics laboratory in RIKEN for giving me kind encouragement.

Appendix A

Magnetic Properties of Neutron $^3P_2$ Superfluids

In this appendix, we discuss quantized vortices in neutron $^3P_2$ superfluids, which are believed to be realized in high density neutron matter in neutron stars. By using the Ginzburg-Landau free energy for $^3P_2$ superfluids, we not only determine the ground state but also construct the $^3P_2$ quantized vortices numerically in the absence and presence of the external poloidal magnetic field along the vortex axis. We find in certain situations the spontaneous magnetization of the vortex core with a typical magnitude of about 10^{7-8} Gauss. However, the net magnetic field turns out to be negligible if we take into account the area density of the vortices. The discussion in this appendix is based on [5].

A.1 Magnetic Field of NSs

We can estimate the magnitude of the surface magnetic field $B_{\rm sur}$ of the NSs from the P-$\dot{P}$ diagram under the assumption that the rotation energy loss comes only from the magnetic dipole radiation $P_{\rm RAD}$,

$$P_{\rm RAD} = -\frac{dE_{\rm ROT}}{dt} \tag{A.1}$$

where $E_{\rm ROT}$ is the rotational energy of NSs. $P_{\rm RAD}$ from the magnetic dipole inclined by the angle α from the rotational axis is given by the radius R and the surface magnetic field $B_{\rm sur}$.

$$P_{\rm RAD} = \frac{2}{3}(B_{\rm sur}R^3{\rm sin}\alpha)^2\left(\frac{2\pi}{P}\right)^4. \tag{A.2}$$

On the other hand, the rotational energy is

$$E_{\rm ROT} = \frac{1}{2}I\left(\frac{2\pi}{P}\right)^2 \tag{A.3}$$

where I is the momentum inertia of uniform and spherical NSs, $I = \frac{2}{5}MR^2$. As a result, by solving Eq. (A.1), we can obtain

$$B_{\rm sur}^2 = \frac{3I}{8\pi^2 R^6 \sin^2\alpha} P\dot{P}. \tag{A.4}$$

Most abundant middle-aged pulsars show $B_{\rm sur} = 10^{11-13}$ Gauss. In recent years, young NSs with strong magnetic field $\sim 10^{13-15}$ Gauss have been observed by the observations of some soft gamma ray repeaters and anomalous X-ray pulsars. This kind of NSs is called as the magnetar.

There have been various theoretical attempts to attribute the origin of the strong magnetic field of NSs to the intrinsic magnetization of the neutron star matter, spontaneous magnetization of neutron matter and its failure [120], the ferromagnetism from the quark matter [121, 122], the inhomogeneous phase [123] and the pion domain wall [124]. In [125], the authors discussed the possibility that the vortex core in neutron $^3P_2$ superfluidity may have the spontaneous magnetization. However, in this appendix, we show that there is only negligible spontaneous magnetization in the neutron $^3P_2$ phase in the realistic circumstance of NSs (see [5]).

A.2 Ginzburg Landau Free Energy for $^3P_2$ Superfluids and the Ground State

The GL free energy for the $^3P_2$ superfluidity in the weak coupling limit was derived in [126, 127, 128] assuming the contact interaction. Here let us follow their derivation. To this end, we consider properties of dense neutron matter by the following Hamiltonian H, which includes a zero range $^3P_2$ force

$$H = \int d^3\rho\ \psi^\dagger \left(-\frac{\boldsymbol{\nabla}^2}{2M} - \mu\right)\psi - \frac{1}{2}gT^\dagger_{\alpha\beta}(\boldsymbol{\rho})T_{\alpha\beta}(\boldsymbol{\rho}) \tag{A.5}$$

where $\boldsymbol{\rho}$ denote space coordinates, ψ is a neutron field, μ is a baryon chemical potential, M is the mass of neutrons, and $g(>0)$ is the coupling constant. Here, α, β are the space indices, and the tensor $T_{\alpha\beta}$ is given by

$$T^\dagger_{\alpha\beta}(\boldsymbol{\rho}) = \psi^\dagger_\sigma(\boldsymbol{\rho})(t^*_{\alpha\beta})_{\sigma\sigma'}(\boldsymbol{\nabla})\psi^\dagger_{\sigma'}(\boldsymbol{\rho}) \tag{A.6}$$

with a differential operator t defined by

$$\begin{aligned}(t_{\alpha\beta})_{\sigma\sigma'}(\boldsymbol{\nabla}) &= \frac{1}{2}((S_\alpha)_{\sigma\sigma'}\nabla_\beta + \nabla_\alpha(S_\beta)_{\sigma\sigma'}) \\ &\quad -\frac{1}{3}\delta_{\alpha\beta}(\boldsymbol{S})_{\sigma\sigma'}\cdot\boldsymbol{\nabla}\end{aligned} \tag{A.7}$$

and $\boldsymbol{S}$ defined by $(S_\alpha)_{\sigma\sigma'} = i(\sigma_y\sigma_\alpha)_{\sigma\sigma'}$ $(\alpha = x, y, z)$.

The order parameter for $^3P_2$ superfluidity is 3×3 traceless symmertic tensor $A_{\mu i}$, which is defined by

$$\Delta = \sum_{\mu i} i\sigma_\mu \sigma_y A_{\mu i} k_i \tag{A.8}$$

where Δ is the gap parameter. The Latin letter μ stands for the spin index as before while the Roman index i stands for the spatial coordinates. The symmetry acts on the tensor $A_{\mu i}$ as

$$A \to e^{i\theta} g A g^T, \quad e^{i\theta} \in U(1), \quad g \in SO(3) \tag{A.9}$$

in the matrix notation. The free energy density F as a function of tensor $A_{\mu i}$ can be written as

$$F = \int d^3\rho \ (f_{\rm grad} + f_{2+4} + f_6 + f_H) \tag{A.10}$$

where $f_{\rm grad}$ is the gradient term, f_{2+4} and f_6 [128] are the free energy densities up to fourth order and of the sixth order, respectively, and f_H is the magnetic term, given by

$$f_{\rm grad} = K_1 \partial_i A_{\mu j} \partial_i A^\dagger_{\mu j} + K_2 (\partial_i A_{\mu i} \partial_j A^\dagger_{\mu j} + \partial_i A_{\mu j} \partial_j A^\dagger_{\mu i}) \tag{A.11}$$

$$f_{2+4} = \alpha {\rm Tr} A A^\dagger + \beta [({\rm Tr} A A^\dagger)^2 - {\rm Tr} A^2 A^{\dagger 2}], \tag{A.12}$$

$$\begin{aligned} f_6 = \ & \gamma [-3({\rm Tr} A A^\dagger)|{\rm Tr} A A|^2 + 4({\rm Tr} A A^\dagger)^3 \\ & + 12({\rm Tr} A A^\dagger){\rm Tr}(A A^\dagger)^2 + 6({\rm Tr} A A^\dagger){\rm Tr}(A^2 A^{\dagger 2}) \\ & + 8{\rm Tr}(A A^\dagger)^3 + 12{\rm Tr}[(A A^\dagger)^2 A^\dagger A] \\ & - 12{\rm Tr}[A A^\dagger A^\dagger A A] - 12{\rm Tr} A A ({\rm Tr} A A^\dagger A A)^*] \end{aligned} \tag{A.13}$$

and

$$f_H = g'_H H^2 {\rm Tr}(A A^\dagger) + g_H H_\mu (A A^\dagger)_{\mu\nu} H_\nu. \tag{A.14}$$

In Table A.1, we summarize the coefficients (the GL parameters) calculated in the weak coupling limit by considering only the excitations around the Fermi surface [126, 127, 128]. In this limit, K_1 and K_2 take the same value. We ignore the first term with the coefficient g'_H of f_H in Eq. (A.14) since the effect of this term can be incorporated into the shift of α in f_{2+4} and consequently the phase structure is not modified.

The ground states of the GL free energy with total angular momentum two were classified by Mermin [129]. According to this classification, the ground state of $^3P_2$ superfluids in the weak coupling limit is in the nematic phase [130].

Firstly, we consider the simplest case f_{2+4}. At the fourth order level, the ground state $A_{\rm 4th}$ can be written as

$$A^{(x,y,z)}_{\rm 4th} = \sqrt{\frac{|\alpha|}{\beta(r^2 + (1+r)^2 + 1)}} \begin{pmatrix} r & 0 & 0 \\ 0 & -(1+r) & 0 \\ 0 & 0 & 1 \end{pmatrix} \tag{A.15}$$

α	$K_1 = K_2$	β	γ	g_H
$\frac{N(0)}{3}\frac{T-T_c}{T}k_F^2$	$\frac{7\zeta(3)}{240m^2}\frac{N(0)}{(\pi T_c)^2}k_F^4$	$\frac{7\zeta(3)}{60}\frac{N(0)}{(\pi T_c)^2}k_F^4$	$-\frac{31}{16}\frac{\zeta(5)}{840}\frac{N(0)}{(\pi T_c)^4}k_F^6$	$\frac{7\zeta(3)}{24}\frac{N(0)}{(\pi T_c)^2}\frac{(\gamma_n\hbar)^2}{2(1+F)^2}H^2k_F^2$

Table A.1: The GL parameters in the weak coupling limit. In the derivation of α, we took $g = \frac{3\pi^2}{mk_F^3}$ in order for the T dependence of α to become the same with that of the BCS theory. Here, k_F is the Fermi momentum defined by $k_F = \hbar c(3\pi^2\rho)^{1/3}$ where ρ is the neutron density. $N(0) \equiv \frac{mk_F}{2\pi^2}$ is the density of states $N = \frac{mk}{2\pi^2}$ on the Fermi surface $k = k_F$, T_c is the critical temperature for the $^3P_2$ superfluidity and the Riemann zeta function $\zeta(n)$ is defined by $\zeta(n) = \sum_{k=1}^{\infty}\frac{1}{k^n}$, for which $\zeta(3) \sim 1.202$ and $\zeta(5) \sim 1.037$. γ_n is the gyromagnetic ratio of the neutrons and F is the Fermi liquid correction about the Pauli spin susceptibility. We take $F = -0.75$, $T_c = 0.2$MeV, $T = 0.8T_c$ and $\rho = 0.17/\text{fm}^3$ for numerical simulations.

with a continuous degeneracy r up to the $SO(3)$ action, where (x, y, z) implies that we take the Cartesian xyz coordinates for the indices of the tensor A. Here, $r \in \mathbb{R}$ is a parameter whose range can be restricted to $-1 \le r \le -1/2$ without the loss of generality. In this range, the eigenvalues in the order parameter have the following magnitude relation

$$(1+r)^2 \le r^2 \le 1. \tag{A.16}$$

The ground states are continuously degenerate with parameterized by r [131] and are referred as the nematic phase. The ground state manifold can be decomposed into three region called strata that have the isomorphic unbroken symmetries H; the uniaxial nematic (UN) phase for $r = -1/2$, D_2 biaxial nematic (D_2 BN) phase for $-1 < r < -1/2$, and D_4 biaxial nematic (D_4 BN) phase for $r = -1$. We summarize the unbroken symmetry H, the order parameter manifold G/H and the homotopy groups from π_0 to π_4 of the order parameter manifold in Table A.2.

Next, let us consider the total free energy including the sixth order term and magnetic term $(f_{2+4} + f_6 + f_H)$, where we consider the magnetic field along the z axis. The intermediate states with the symmetry D_2, that we call the D_2 BN phase, are realized. The order parameter has the following form

$$A^{(x,y,z)} = N_{\text{tot}}\begin{pmatrix} 1 & 0 & 0 \\ 0 & r & 0 \\ 0 & 0 & -1-r \end{pmatrix}. \tag{A.17}$$

The free energy density $f_4 + f_6 + f_H$ can be written in terms of the parameter r and N_{tot} as follows:

$$\begin{aligned} f_{2+4} + f_6 + f_H &= (2\alpha(1+r+r^2) + g_H H_z^2(1+r)^2)N_{\text{tot}}^2 \\ &+ \beta(2r^4 + 4r^3 + 6r^2 + 4r + 2)N_{\text{tot}}^4 \\ &+ \gamma(48r^6 + 144r^5 + 312r^4 + 384r^3 \\ &\quad +312r^2 + 144r + 48)N_{\text{tot}}^6. \end{aligned} \tag{A.18}$$

r	Phase	H	G/H	π_0	π_1	π_2	π_3	π_4	Physical situation
$-1/2$	UN	$O(2)$	$U(1)\times[SO(3)/O(2)]$	0	$\mathbb{Z}\oplus\mathbb{Z}_2$	$\mathbb{Z}$	$\mathbb{Z}$	$\mathbb{Z}_2$	$f_{2+4}+f_6$
$-1<r<-1/2$	D_2 BN	D_2	$U(1)\times[SO(3)/D_2]$	0	$\mathbb{Z}\oplus\mathbb{Q}$	0	$\mathbb{Z}$	$\mathbb{Z}_2$	$f_{2+4}+f_6+f_H$
-1	D_4 BN	D_4	$[U(1)\times SO(3)]/D_4$	0	$\mathbb{Z}\times_h D_4^*$	0	$\mathbb{Z}$	$\mathbb{Z}_2$	$f_{2+4}+f_H$

Table A.2: The strata in the nematic phase. We show the range of r, the phase, the unbroken symmetry H, the order parameter manifold G/H, the homotopy groups from π_0 to π_4, and the physical situations (free energy) that realize these states. $*$ indicates the universal covering group, and $\mathbb{Q}=D_2^*$ is a quaternion group. For the definition of the product $\times_h$, see §4.2.2 and Appendix A of [132].

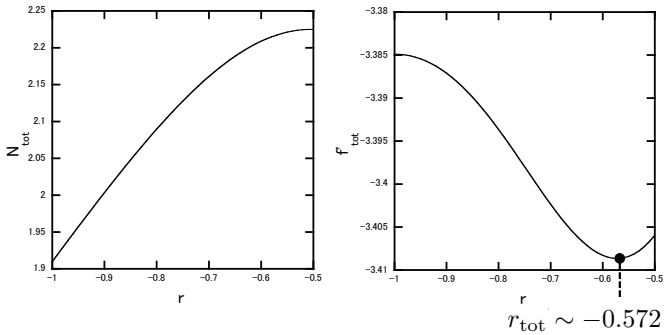

Figure A.1: The normalization and free energy $f_{2+4}+f_6+f_H$. Left panel: the normalization $N_{\rm tot}$ as a function of r. Right panel: $f'_{\rm tot}$ defined by $f_{2+4}+f_6+f_H\equiv\frac{|\alpha|^2}{6\beta}f'_{\rm tot}$ as a function of r (for $H=10^{15}$ Gauss). The intermediate state, the D_2 BN state (with $r\sim-0.572$ for $H=10^{15}$ Gauss), is the ground state.

By minimizing this free energy density with respect to r and $N_{\rm tot}$, we can obtain the ground state. In Fig. A.1, we plot $N_{\rm tot}$ and the free energy density as a function of r with $H=10^{15}$ Gauss. In this case, the minimum free energy density can be achieved at

$$r\sim-0.572\equiv r_{\rm tot}\ \text{for}\ H=10^{15}\ \text{Gauss}. \tag{A.19}$$

A.3 Vortex Structures in $^3P_2$ Superfluids

When superfluids are rotating, superfluid vortices are created along the rotation axis. In this section, we discuss vortices in the $^3P_2$ superfluids. The existence of vortices in the $^3P_2$ superfluids is topologically ensured by the first homotopy group summarized in Table A.2. The number

N_v of vortices with the unit circulation created inside rotating neutron stars can be estimated to be

$$N_v \sim 1.9 \times 10^{19} \left(\frac{1\text{ms}}{P}\right) \left(\frac{M^*}{900\text{MeV}}\right) \left(\frac{R}{10\text{km}}\right)^2 \tag{A.20}$$

where P is the period of the neutron star, M^* is the effective neutron mass, and R is the radius of the $^3P_2$ superfluid. Then, we can estimate the distance between vortices d from

$$\pi d^2 \times N_v = \pi R^2, \tag{A.21}$$

that implies the intervortex distance d to be

$$d \sim 1.7 \times 10^{-6}\text{m} \tag{A.22}$$

for the typical values for P, M^* and R in Eq. (A.20). On the other hand, the coherence length ξ of $^3P_2$ superfluid is about $10-100$ fm. Therefore the distance between vortices is much larger than the coherence length, and therefore we consider a single vortex below.

Let us derive the equation of motion from the free energy F introduced in the last section. Here, we consider the following Ansatz for the order parameter of a vortex state:

$$\begin{aligned} A^{(x,y,z)} &= \sqrt{\frac{|\alpha|}{6\beta}} R(n\theta) A^{(\rho,n\theta,z)} R^T(n\theta) e^{il\theta}, \\ A^{(\rho,n\theta,z)} &= \begin{pmatrix} f_1 & ige^{im\theta+i\delta} & 0 \\ ige^{im\theta+i\delta} & f_2 & 0 \\ 0 & 0 & -f_1-f_2 \end{pmatrix} \end{aligned} \tag{A.23}$$

in the cylindrical coordinates (ρ, θ, z), where l, m, n are integers, $l, m, n \in \mathbb{Z}$, explained below, δ is a constant, $A^{(x,y,z)}$ is the order parameters in the Cartesian basis and $A^{(\rho,n\theta,z)}$ is the order parameters in the cylindrical basis ($n = 1$) or its higher generalizations, which are related by a rotation matrix R, given by

$$R(n\theta) = \begin{pmatrix} \cos n\theta & -\sin n\theta & 0 \\ \sin n\theta & \cos n\theta & 0 \\ 0 & 0 & 1 \end{pmatrix}. \tag{A.24}$$

In Eq. (A.23), f_1, f_2, g are profile functions depending only on the radial coordinate ρ, and the boundary conditions for them are

$$\begin{aligned} &f_1, f_2 \to \text{constant}, \quad g \to 0 && \text{as } \rho \to \infty, \\ &f_1, f_2 \to 0, \quad \begin{cases} g \to 0 \text{ for } n \neq -1 \\ g' \to 0 \text{ for } n = -1 \end{cases} && \text{as } \rho \to 0, \end{aligned} \tag{A.25}$$

where the case of $n = -1$ is exceptional since the the total winding of g vanishes. As denoted, the configuration is labeled by the three integers $l, m, n \in \mathbb{Z}$, where l is the winding number of

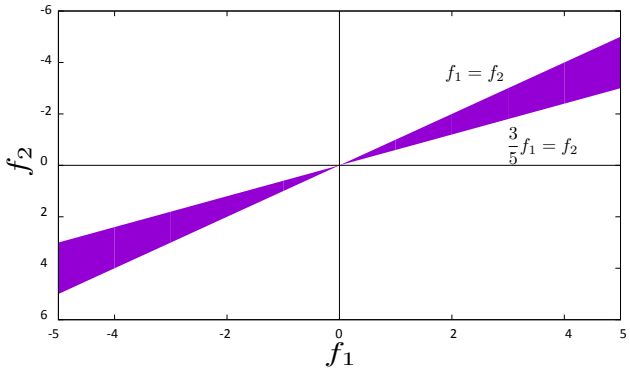

Figure A.2: The conditions for determining whether the Cartesian basis or cylindrical basis is realized. The cylindrical basis ($n = 1$) is realized in the shaded area while the Cartesian basis ($n = 0$) is realized in the rest.

the vortex, n represents a rotation of $SO(3)$ that does not have a topological nature, and m is a semi-topological winding number (relative to that of $f_{1,2}$) defined locally for the component g [1].

Let us consider the tension, the energy per unit length, of the vortex. A bulk part of free energy density, $f_{2+4} + f_6 + f_H$, does not depend on the integers l, m, n, while the gradient term depends on them; The leading contribution to the gradient energy at large ρ depends on n and l as follows:

$$\begin{aligned} F &= \int d^2\rho \frac{1}{\rho^2}\big[2K_1(l^2(f_1^2 + f_1 f_2 + f_2^2) + n^2(f_1 - f_2)^2) \\ &\quad +2K_2(f_1^2 \sin^2(n-1)\theta + f_2^2 \cos^2(n-1)\theta) + n^2(f_1 - f_2)^2\big] \\ &\sim 2\pi \log L[2K_1(l^2(f_1^2 + f_1 f_2 + f_2^2) + n^2(f_1 - f_2)^2)) \\ &\quad + \begin{cases} 2K_2(l^2 f_2^2 + n^2(f_1 - f_2)^2)] & (n = 1) \\ K_2\left(l^2(f_1^2 + f_2^2) + 2n^2(f_1 - f_2)^2\right)] & (n \neq 1) \end{cases} \end{aligned} \tag{A.26}$$

where $\sim$ denotes the asymptotic form and L is the system size transverse to the vortex, and f_1 and f_2 in the last line are the boundary values evaluated at $\rho \to \infty$.

From this equation, we first see that the configuration with $l = 1$ has the lower energy than the configuration with higher winding numbers $l > 1$, as for conventional superfluids, thereby a vortex with the higher winding l is unstable to be split into l unit winding vortices. In the following, we concentrate on $l = 1$.

As for n, we find that either the case of $n = 0$ (the xyz-basis) or of $n = 1$ (the cylindrical basis) gives the lowest free energy. The condition on f_1 and f_2 that determines which configuration with $n = 0$ or $n = 1$ has lower energy is plot in Fig. A.2, where the cylindrical basis

[1] Since the boundary condition for g are zero for $\rho = 0, \infty$, it is a ring-shape if it appears, and m denotes how many times the phase of g is twisted along the ring, see [133] for a similar example in a spinor BEC.

$(n = 1)$ gives lower energy in the shaded region defined by

$$\frac{3}{5}f_1 < f_2 < f_1, \tag{A.27}$$

while the xyz basis $(n = 0)$ gives lower energy in the rest.

We calculate the free energy per the unit vortex length analytically for each basis:

$$F = \int d^2\rho \, \frac{|\alpha|}{6\beta}\big(K_1 t_1 + K_2 t_2 + \alpha t_3 + \frac{|\alpha|}{6\beta}\beta t_4 + \frac{\alpha^2}{36\beta^2}\gamma t_5\big) \tag{A.28}$$

where the terms t_1 and t_2 come from the gradient terms and the terms t_3, t_4 and t_5 come from the second, fourth and sixth order terms in the GL free energy density. Here $t_{1,2}$ can be written in the cylindrical basis as

$$\begin{aligned} t_1^{(\rho,\theta,z)} &= 2(f_1'^2 + f_2'^2 + f_1' f_2' + g'^2) + \frac{1}{\rho^2}(4f_1^2 + 4f_2^2 - 2f_1 f_2 \\ &\quad +(8 + 2(m+1)^2)g^2 - 4(f_1 - f_2)g(m+2)\cos(m\theta + \delta)), \end{aligned} \tag{A.29}$$

$$\begin{aligned} t_2^{(\rho,\theta,z)} &= 2(f_1'^2 + g^2) + \frac{2}{\rho^2}(f_2^2 + 4g^2 + (m+1)^2 g^2 + (f_1 - f_2)^2 \\ &- 2g(m+1)(f_1 - f_2)\cos(m\theta + \delta) + 4f_2 g\cos(m\theta + \delta)) \\ &+ \frac{1}{\rho}(-2(f_1' + f_2')g(m+1)\cos(m\theta + \delta) + 2(f_1 + f_2)g'\cos(m\theta + \delta) \\ &+ 2(f_1' + f_2')(f_1 - f_2)), \end{aligned} \tag{A.30}$$

and in the xyz basis as

$$t_1^{(x,y,z)} = 2(f_1'^2 + f_2'^2 + f_1' f_2' + g'^2) + \frac{2}{\rho^2}(f_1^2 + f_2^2 + f_1 f_2 + (m+1)^2 g^2), \tag{A.31}$$

$$\begin{aligned} t_2^{(x,y,z)} &= 2(\cos^2\theta f_1'^2 + \sin^2\theta f_2'^2 + g'^2) + \frac{2}{\rho^2}(\sin^2\theta f_1^2 + \cos^2\theta f_2^2 + (m+1)^2 g^2) \\ &- 2\sin 2\theta \sin(m\theta + \delta)(f_1' + f_2')g' - \frac{2}{\rho}\cos 2\theta\cos(m\theta + \delta)(m+1)(f_1' + f_2')g \\ &+ \frac{2}{\rho}\cos 2\theta\cos(m\theta + \delta)(f_1 + f_2)g' + \frac{2}{\rho^2}\sin 2\theta\sin(m\theta + \delta)(m+1)(f_1 + f_2)g. \end{aligned} \tag{A.32}$$

The rest terms of the free energy density $t_{3,4,5}$ can be written in the both basis as

$$t_3 = 2(f_1^2 + f_2^2 + f_1 f_2 + g^2), \tag{A.33}$$

$$\begin{aligned} t_4 = {} & 2f_1^4 + 4f_1^3 f_2 + 6f_1^2 f_2^2 + 4f_1 + f_2^3 + 2f_2^4 \\ & +((6 + 2\cos 2(m\theta + \delta))f_1^2 + 4f_1 f_2 + (6 + 2\cos 2(m\theta + \delta))f_2^2)g^2 + 2g^4, \end{aligned} \tag{A.34}$$

$$\begin{aligned} t_5 &= 48f_1^6 + 144f_1^5 f_2 + 312f_1^4 f_2^2 + 384f_1^3 f_2^3 + 312f_1^2 f_2^4 + 144f_1 f_2^5 + 48f_2^6 + 48g^6 \\ &+ ((288 + 144\cos 2(m\theta + \delta))f_1^4 + (360 + 120\cos 2(m\theta + \delta))f_1^3 f_2 \\ &+ (576 + 240\cos 2(m\theta + \delta))f_1^2 f_2^2 + (360 + 120\cos 2(m\theta + \delta))f_1 f_2^3 \\ &+ (288 + 144\cos 2(m\theta + \delta))f_2^4)g^2 + ((288 + 120\cos 2(m\theta + \delta))f_1^2 \\ &+ (144 - 48\cos 2(m\theta + \delta))f_1 f_2 + (288 + 120\cos 2(m\theta + \delta))f_2^2)g^4. \end{aligned} \tag{A.35}$$

	Case (1)	Case (2)
Phase	D_2 BN	D_2 BN
$\begin{pmatrix} f_1 & & \\ & f_2 & \\ & & -f_1-f_2 \end{pmatrix}$ at $\rho \to \infty$	$\begin{pmatrix} r_{\rm grad} & & \\ & -1-r_{\rm grad} & \\ & & 1 \end{pmatrix}$	$\begin{pmatrix} 1 & & \\ & r_{\rm tot} & \\ & & -1-r_{\rm tot} \end{pmatrix}$
Basis	$n=1$	$n=0$
Situation ($f_{\rm grad}+f_{2+4}$ plus)	non	$f_6+f_{H(\|\|\boldsymbol{z})}$

Table A.3: The boundary conditions and physical situation for each case. $r_{\rm grad} \equiv 6-\sqrt{43} \sim -0.557$ given in Eq. (A.38), and $r_{\rm tot}$ depends on the magnetic field ($r_{\rm tot} \sim -0.572$ in Eq. (A.19) for $H = 10^{15}$ Gauss).

The effect of δ on the free energy density is not clear. At present, we restrict the case with $\delta = 0$, which is consistent with the equation of motion, since the imaginary part of non-diagonal elements is directly connected with real part of diagonal elements through the equation of motion. By substituting the order parameter into Eq. (A.10) and differentiating it with respect to f_1, f_2 and g, we obtain the sets of the equation of motions for each basis.

A.4 Vortex Solutions

In this section, we construct the vortex configurations in the following two cases:

- Case (1): $F = \int d^2\rho\ f_4$
- Case (2): $F = \int d^2\rho\ (f_4 + f_6 + f_H)$ and $\boldsymbol{H} \parallel \boldsymbol{z}$.

We summarize the forms of the order parameters in these cases in Table A.3. In numerical simulations, we change the variable ρ ($0 \le \rho < \infty$) by $\tanh\rho$ ($0 \le \tanh\rho < 1$). We divide the domain of $\tanh\rho$ into 100 parts and solve the equations of motion simultaneously by using the Newton's method.

Case (1)

This is only the case studied before [127, 134, 125]. This case may be thought to be unphysical because of the presence of the sixth order term, but it is relevant when the gap is small enough (f_6 is much smaller than f_4) and the magnetic field is small compared with f_4. In this case, the ground state takes the form in Eq. (A.15) due to the fourth order term. We can see from Eq. (A.26) that the leading part of free energy proportional to $\log L$ becomes lower when $f_2^2 \le f_1^2$, so that we take the following order parameter form

$$A^{(x,y,z)} \propto \sqrt{\frac{1}{r^2+r+1}} R(n\theta) \begin{pmatrix} r & 0 & 0 \\ 0 & -1-r & 0 \\ 0 & 0 & 1 \end{pmatrix} R^T(n\theta) e^{i\theta} \tag{A.36}$$

with $-1 \leq r \leq -1/2$. Let us assume that the ground state is in the cylindrical basis ($n = 1$). By putting the order parameter into Eqs. (A.29) and (A.30), we obtain

$$F \propto \frac{9r^2 + 10r + 3}{r^2 + r + 1} \log L. \tag{A.37}$$

Then, by differentiating this free energy with respect to r, we get [127, 134, 125]

$$r = 6 - \sqrt{43} \sim -0.557 \equiv r_{\rm grad} \tag{A.38}$$

that satisfies the condition for the realization of the cylindrical basis, Eq. (A.27), and so the lowest energy state is in the cylindrical basis ($n = 1$) consistently. It is interesting to emphasize that the particular r is selected as the vortex boundary state although the ground states are continuously degenerate with r.

In Fig. A.3, we plot the profiles functions f_1, f_2 and g as functions of the distance ρ from the vortex center. The red curves correspond to the case of $m = 0$ with $g \neq 0$, which is the case considered in Ref. [125] without explicit solutions. The new solution here is the case with $g = 0$ represented by the black curves. We check that all the terms in the equation of motion for g contain g if $m \neq 0$. Consequently, in this case, $g = 0$ is a trivial solution in the entire region of ρ since g is fixed to be zero at the both boundaries. This implies that all $m \neq 0$ give the same solution of $g = 0$. In order to determine which state between $g \neq 0$ (with $m = 0$) and $g = 0$ has less energy, we should compare the free energies for these two cases, but we leave it as a future problem.

Case (2)

Next, let us consider the most realistic case for neutron stars, that is, the case with the sixth order term in the presence of the magnetic field of 10^{15} Gauss along the $\boldsymbol{z}$ axis.

In this case, the smallest eigenvalue $-1 - r$ comes to the z component. By minimizing Eq. (A.18), we have $r = r_{\rm tot} \sim -0.572$ in Eq. (A.19) as the boundary condition at large distance. Therefore, the xyz basis ($n = 0$) is realized.

In Fig. A.4, we plot f_1, f_2 and g as functions of ρ with $m = -2, ..., 2$ in the case (2). In this situation, we find that $g = 0$ is a trivial solution in the entire region of ρ except for the cases of $m = \pm 2$. This implies that all $m(\neq \pm 2)$ give the same solution. In the $n = 0$ basis, the equation of motions for f_1 and f_2 have the same form. The blue, green and black curves correspond to the cases of $g \neq 0$ with $m = 2$, $g \neq 0$ with $m = -2$, and $g = 0$, respectively. In figures for f_1 and f_2, the cases of $g \neq 0$ with $m = \pm 2$ and of $g = 0$ take the different values numerically although they are almost overlapped.

A.5 Spontaneous Magnetization of the $^3P_2$ Vortex Core

In this section, we calculate the spontaneous magnetization of $^3P_2$ vortex cores due to the neutron anomalous magnetic moment for the vortex profiles obtained in the last section. The

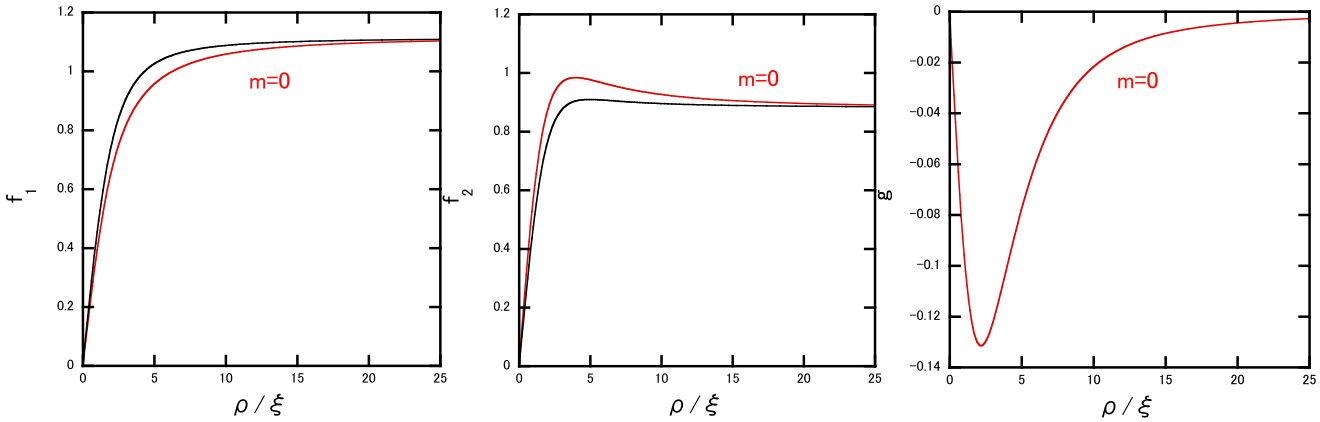

Figure A.3: The profile functions f_1, f_2 and g as functions of the distance ρ/ξ from the vortex center in the case (1). The red curves correspond to the case of $g \neq 0$ with $m = 0$, while the black curves correspond to the case of $g = 0$.

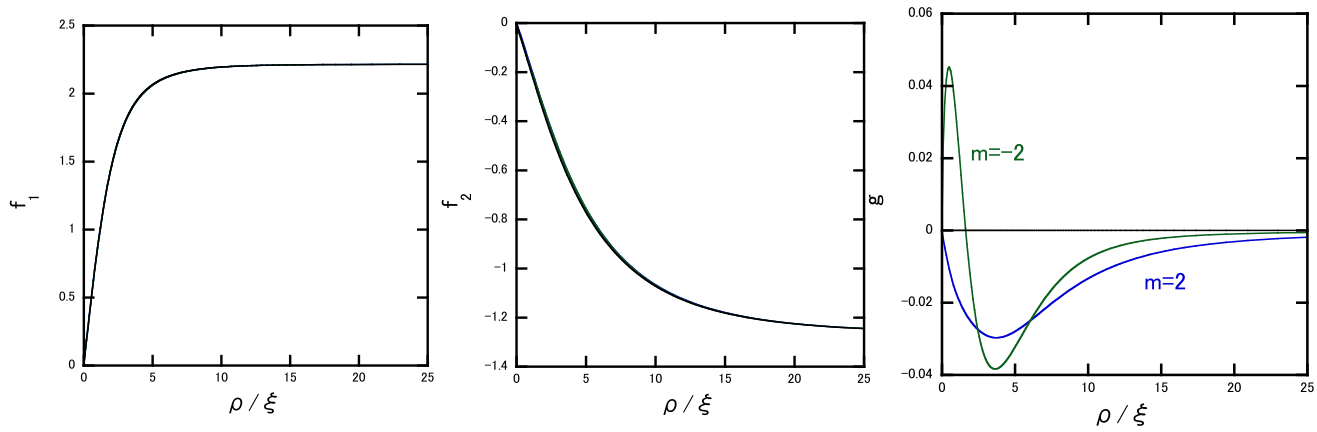

Figure A.4: The profile functions f_1, f_2 and g as functions of the distance ρ/ξ from the vortex center in the case (2). The blue, green and black curves correspond to the cases of $g \neq 0$ with $m = 2$, $g \neq 0$ with $m = -2$ and $g = 0$, respectively. In the figures of f_1 and f_2, all the cases take the different values numerically.

spontaneous magnetization was already reported in the case (1) [125]. This is a characteristic feature of $^3P_2$ vortices that is absent for conventional $^1S_0$ vortices. The vortex magnetization $\boldsymbol{M}(\rho)$ can be calculated as

$$\begin{aligned}
\boldsymbol{M} &= \frac{\gamma_n \hbar}{2}\hat{\boldsymbol{\sigma}}, \\
\hat{\boldsymbol{\sigma}} &= T\sum_n \int \frac{d^3k}{(2\pi)^3}\mathrm{Tr}(\boldsymbol{\sigma}G(k,\omega_n)) \\
&= \int \frac{d\Omega}{4\pi}\mathrm{Tr}(\boldsymbol{\sigma}\Delta\Delta^\dagger)T\sum_n \int d\xi N(0)\frac{i\omega_n + \xi}{(\omega_n^2+\xi^2)^2} \\
&= \frac{4}{9}N'(0)k_F^2\frac{|\alpha|}{6\beta}g(\rho)(f_1(\rho)-f_2(\rho))\mathrm{cos}m\theta\hat{\boldsymbol{z}}
\end{aligned} \tag{A.39}$$

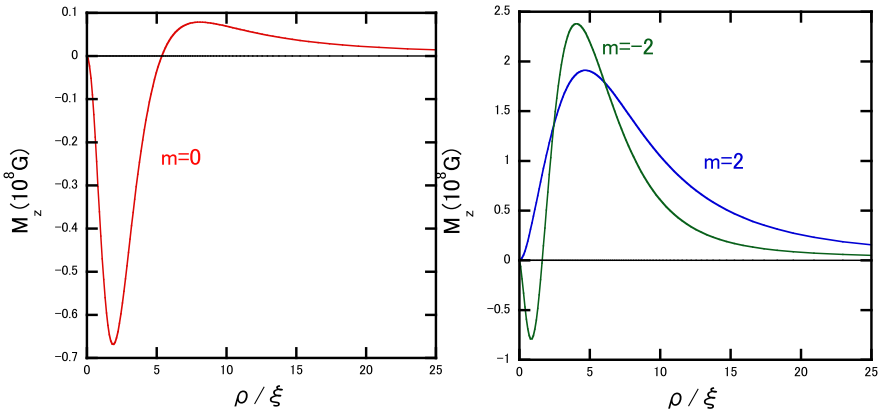

Figure A.5: The dependence of the magnetizations M_z on the distance ρ/ξ from the vortex core in the cases (1) and (2). The red, blue and green curves correspond to the cases of $m = 0$, $m = 2$ and $m = -2$ with $g \neq 0$, respectively, while the black lines correspond to the case with $g = 0$ in the cases (1) or (2).

where $G(k, \omega_n)$ is a thermal Green function and $\omega_n = (2n+1)\pi T$ is the Matsubara frequency and $N'(0) = \frac{m^2}{2\pi^2 k_F}$ is the density of states differentiated by the energy $E = k^2/2m$, $N' = \frac{m^2}{2\pi^2 k}$, evaluated at the Fermi surface $k = k_F$.

By using the results of the last section, we obtain the magnetization $\boldsymbol{M}$ as a function of ρ. We plot M_z (for $\theta = 0$) as a function of ρ in Fig. A.5. Red, blue and green curves correspond to the case with $m = 0$, $m = 2$ and $m = -2$ and with non-zero g. Black curves are the case with $g = 0$. The maximum value of M_z is about 10^8-10^9 Gauss when it is nonzero. The mean magnetic field in a vortex lattice, which is obtained roughly by multiplying $(\xi/d)^2 \sim 10^{-14}$, is much smaller than the observed magnetic field about 10^{12}-10^{15} Gauss, and consequently this magnetic field is negligible.

Note that the magnetization M_z is proportional to $(f_1(\rho) - f_2(\rho))g(\rho)\cos m\theta$. Since it is proportional to the off-diagonal profile function g appearing around the vortex cores, it is nonzero only for the cases of $m = 0$ in the cylindrical basis and of $m = \pm 2$ in the xyz-basis. When $f_1 \neq f_2$ in the region $g \neq 0$, the magnetization can occur. Among all the cases with nonzero magnetization M_z, only the case with $m = 0$ has a net magnetization, since the θ integration of $\cos m\theta$ vanishes for $m \neq 0$. Although the case of $m = \pm 2$ in the cylindrical basis has no net magnetization, the direction of the magnetization drastically changes upward and downward depending on θ, thereby implying the existence of the large current crossing to the vortex.

Appendix B

Tolman-Oppenheimer-Volkov Equation

In this appendix, we derive the Tolman-Oppenheimer-Volkov (TOV) equation, obtained through Einstein equation with the Schwarzschild metric, which is a spherically symmetric vacuum solution.

The metric with a spherical symmetry is

$$ds^2 = -e^{2\phi(r,t)}dt^2 + e^{2\lambda(r,t)}dr^2 + r^2(d\theta^2 + \sin^2\theta d\varphi^2). \tag{B.1}$$

From the Euler-Lagrange equations

$$\frac{\partial I}{\partial x^\mu} = \frac{d}{d\tau}\frac{\partial I}{\partial(dx^\mu/d\tau)} \tag{B.2}$$

where $\mu = t, r, \theta, \varphi$,

$$\begin{aligned} S &= -\int I d\tau \\ I &= e^{2\phi}\left(\frac{dt}{d\tau}\right)^2 - e^{2\lambda}\left(\frac{dr}{d\tau}\right)^2 - r^2\left(\frac{d\theta}{d\tau}\right)^2 - r^2\sin^2\theta\left(\frac{d\varphi}{d\tau}\right)^2 \end{aligned} \tag{B.3}$$

and the following geodesic equation

$$\frac{d^2x^\mu}{d\tau^2} + \Gamma^\mu_{\alpha\beta}\frac{dx^\alpha}{d\tau}\frac{dx^\beta}{d\tau} = 0 \tag{B.4}$$

where

$$\begin{aligned} \Gamma^\alpha_{\beta\gamma} &= g^{\alpha\mu}\Gamma_{\mu\beta\gamma} \\ &= g^{\alpha\mu}\frac{1}{2}(g_{\mu\beta,\gamma} + g_{\mu\gamma,\beta} - g_{\beta\gamma,\mu}) \end{aligned} \tag{B.5}$$

is the Christoffel symbols, we can obtain the explicit form of $\Gamma^\alpha_{\beta\gamma}$ with the metric Eq. (B.1). We summarize the Christoffel symbols in Table. B.1. Here $'$ and $\dot{}$ correspond to the derivative with respect to r and t respectively.

The Einstein equation is

$$R^\alpha_\beta - \frac{1}{2}\delta^\alpha_\beta R^\mu_\mu = 8\pi G T^\alpha_\beta \tag{B.6}$$

where R^{α}_{β} and T^{α}_{β} are Ricci tensor and the energy momentum tensor respectively can be written down explicitly:

$$8\pi G T^t_t = -\left(\frac{2\dot{r}\dot{\lambda}}{r} + \frac{\dot{r}^2}{r^2}\right)e^{-2\phi} + \left(\frac{2r''}{r} + \frac{r'^2}{r^2} - \frac{2r'\lambda'}{r}\right)e^{-2\lambda} - \frac{1}{r^2}, \tag{B.7}$$

$$8\pi G T^t_r = \frac{2e^{-2\phi}}{r}(\dot{r}' - \dot{r}\phi' - \dot{\lambda}r'), \tag{B.8}$$

$$8\pi G T^r_r = \left(\frac{2r'\phi'}{r} + \frac{r'^2}{r^2}\right)e^{-2\lambda} - \left(\frac{2\ddot{r}}{r} + \frac{\dot{r}^2}{r^2} - \frac{2\dot{r}\dot{\phi}}{r}\right)e^{-2\phi} - \frac{1}{r^2}, \tag{B.9}$$

$$\begin{aligned} 8\pi G T^{\theta}_{\theta} &= -\left(\ddot{\lambda} + \dot{\lambda}^2 - \dot{\phi}\dot{\lambda} - \frac{\dot{r}\dot{\phi}}{r} + \frac{\ddot{r}}{r} + \frac{\dot{r}\dot{\lambda}}{r}\right)e^{-2\phi} \\ &\quad + \left(\phi'' + \phi'^2 - \lambda'\phi' + \frac{r'\phi'}{r} - \frac{r'\lambda'}{r} + \frac{r''}{r}\right)e^{-2\lambda}. \end{aligned} \tag{B.10}$$

On the other hand, the energy momentum tensor for the perfect fluid in the left-hand side is given by

$$T_{\mu\nu} = (\varepsilon + P)u_\mu u_\nu + P g_{\mu\nu} \tag{B.11}$$

where u^μ is the fluid's four velocity and ε and P are the energy density and pressure. In the laboratory system, u^μ becomes

$$u^t = \frac{dt}{d\tau} = e^{-\phi},\ u^r = u^\theta = u^\varphi = 0. \tag{B.12}$$

Table B.1: Christoffel symbols with a spherically symmetric matric.

Γ	t	r	θ	φ
tt	$\dot{\phi}$	$\phi' e^{2\phi-2\lambda}$	0	0
tr	ϕ'	$\dot{\lambda}$	0	0
$t\theta$	0	0	$\dot{r}/r$	0
$t\varphi$	0	0	0	$\dot{r}/r$
rr	$\dot{\lambda}e^{2\lambda-2\phi}$	λ'	0	0
$r\theta$	0	0	r'/r	0
$r\varphi$	0	0	0	r'/r
$\theta\theta$	$\dot{r}re^{-2\phi}$	$-r're^{-2\lambda}$	0	0
$\theta\varphi$	0	0	0	$\cot\theta$
$\varphi\varphi$	$\dot{r}re^{-2\phi}\sin^2\theta$	$-r're^{-2\lambda}\sin^2\theta$	-$\sin\theta\cos\theta$	0

Firstly, we define

$$u \equiv \frac{\partial r}{\partial \tau} = e^{-\phi}\dot{r}, \tag{B.13}$$

$$\Gamma \equiv e^{-\lambda}r'. \tag{B.14}$$

From the derivative of u with respect to r and t,

$$u' = e^{-\phi}(\dot{r}' - \phi'\dot{r}) = e^{-\phi}\dot{\lambda}r', \tag{B.15}$$

$$\dot{u} = -\dot{r}\dot{\phi}e^{-\phi}, \tag{B.16}$$

we can get

$$2e^{-\phi}ru\dot{\lambda} = 2ru\frac{u'}{r'} = r\frac{\partial u^2}{\partial r} \tag{B.17}$$

$$\frac{\partial}{\partial r}(r\Gamma^2) = e^{-2\lambda}(r'^2 + 2rr'' - 2rr'\lambda') \tag{B.18}$$

through tr component of the Einstein equation

$$0 = \dot{r}\phi' + \dot{\lambda}r' - \dot{r}'. \tag{B.19}$$

By substituting Eq. (B.17) and (B.18) into the tt component of the Einstein equation

$$-8\pi G\varepsilon r^2 = -\left(2\dot{r}\dot{\lambda}r + \dot{r}^2\right)e^{-2\phi} + \left(2r''r + r'^2 - 2r'\lambda' r\right)e^{-2\lambda} - 1, \tag{B.20}$$

we obtain

$$\begin{aligned} -8\pi G\varepsilon r^2 &= 1 + u^2 + r\frac{\partial u^2}{\partial r} - (2r''r + r'^2 - 2r'\lambda' r)e^{-2\lambda} \\ &= \frac{\partial}{\partial r}(r(1 + u^2 - \Gamma^2)). \end{aligned} \tag{B.21}$$

From this equation, we can obtain

$$\Gamma^2 = 1 + u^2 - \frac{2GM}{r} \tag{B.22}$$

where

$$M(r,t) \equiv \int_0^r 4\pi r^2 \varepsilon dr \tag{B.23}$$

is the mass of the sphere with the radius r.

To derive the TOV equation, we finally consider rr component of the Einstein equation

$$8\pi GPr^2 = \left(2r'\phi' + r'^2\right)e^{-2\lambda} - \left(2\ddot{r}r + \dot{r}^2 - 2\dot{r}\dot{\phi}r\right)e^{-2\phi} - 1 \tag{B.24}$$

$$= \left(2r\frac{\phi'}{r'} + 1\right)\Gamma^2 - u^2 - 2r\dot{u}e^{-\phi} - 1 \tag{B.25}$$

where we use Eq. (B.16). From the energy momentum conservation law along r direction, we obtain

$$\begin{aligned} 0 = T^{\mu}_{r;\mu} &= \frac{1}{e^{\phi+\lambda}r^2}\frac{\partial(\varepsilon e^{\phi+\lambda}r^2)}{\partial t} - \frac{1}{2}\left(-2\phi'\varepsilon + 2\lambda' P + 4\frac{r'}{r}P\right) \\ &= P' + \phi'\varepsilon + \phi' P = 0 \end{aligned} \tag{B.26}$$

by using the covariant derivative

$$T^{\mu}_{\nu;\mu} = \frac{1}{\sqrt{-g}}\frac{\partial(\sqrt{-g}T_{\mu\nu})}{\partial x^{\mu}} - \frac{1}{2}\frac{\partial g_{\mu\alpha}}{\partial x^{\nu}}T^{\mu\alpha}, \tag{B.27}$$

$$\sqrt{-g} = e^{\phi+\lambda}r^2\sin\theta. \tag{B.28}$$

By substituting Eq. (B.26) and (B.22) into Eq. (B.25), we finally get

$$e^{-\phi}\frac{\partial u}{\partial t} = -\frac{1+u^2-2GM/r}{\varepsilon+P}\frac{\partial P}{\partial r} - \frac{GM}{r^2} - 4\pi GPr. \tag{B.29}$$

By imposing the equilibrium state, $u = 0$, this equation is called as the TOV equation,

$$-r^2\frac{dP}{dr} = G\left(M + 4\pi Pr^3\right)(\varepsilon + P)\left(1 - 2GM/r\right)^{-1}. \tag{B.30}$$

The ratios in each term in the right hand side are

$$\frac{P}{\varepsilon} \sim \frac{v_s^2}{c^2},\ \frac{4\pi Pr^3}{M} \sim 3\frac{v_s^2}{c^2},\ \frac{2GM}{r} \sim 4\times 10^{-6}\left(\frac{M}{M_\odot}\right)\left(\frac{R_\odot}{r}\right). \tag{B.31}$$

Therefore, under the condition

$$v_s \ll c,\ r \gg 2GM, \tag{B.32}$$

the TOV equation reduces to the non-relativistic hydrostatic equilibrium equation,

$$\frac{\partial P}{\partial r} = -\frac{GM\varepsilon}{r^2}. \tag{B.33}$$

Appendix C

Fierz Transformation

Generally, the following interaction term $\mathcal{L}_{\rm int}$

$$\mathcal{L}_{\rm int} = g(\bar{q}\Gamma q)^2 = g\Gamma_{il}\Gamma_{kl}\bar{q}_i q_j \bar{q}_k q_l \tag{C.1}$$

can be deformed into the quark-antiquark interaction term $\mathcal{L}_{\rm ex}$ and the quark-quark (antiqaurk-antiquark) interaction term $\mathcal{L}_{\rm qq}$:

$$\mathcal{L}_{\rm int} = -g\Gamma_{ij}\Gamma_{kl}\bar{q}_i q_l \bar{q}_k q_j \equiv \mathcal{L}_{\rm ex}, \tag{C.2}$$

$$\mathcal{L}_{\rm int} = g\Gamma_{ij}\Gamma_{kl}\bar{q}_i \bar{q}_k q_l q_j \equiv \mathcal{L}_{\rm qq}. \tag{C.3}$$

More explicitly, the products of Γ can be decomposed into

$$\Gamma_{ij}\Gamma_{kl} = \sum_M c_M \Gamma^{(M)}_{il}\Gamma^{(M)}_{kj}, \tag{C.4}$$

$$\Gamma_{ij}\Gamma_{kl} = \sum_D c_D (\Gamma^{(D)}C)_{ik}(C\Gamma^{(D)})_{lj}. \tag{C.5}$$

Here, the coefficients c_M and c_D are

$$\begin{pmatrix} (\mathbf{1})_{ij}(\mathbf{1})_{kl} \\ (i\gamma_5)_{ij}(i\gamma_5)_{kl} \\ (\gamma^\mu)_{ij}(\gamma_\mu)_{kl} \\ (\gamma^\mu\gamma_5)_{ij}(\gamma_\mu\gamma_5)_{kl} \\ (\sigma^{\mu\nu})_{ij}(\sigma_{\mu\nu})_{kl} \end{pmatrix} = \begin{pmatrix} \frac{1}{4} & -\frac{1}{4} & \frac{1}{4} & -\frac{1}{4} & \frac{1}{8} \\ -\frac{1}{4} & \frac{1}{4} & \frac{1}{4} & -\frac{1}{4} & -\frac{1}{8} \\ 1 & 1 & -\frac{1}{2} & -\frac{1}{2} & 0 \\ -1 & -1 & \frac{1}{2} & -\frac{1}{2} & 0 \\ 3 & -3 & 0 & 0 & -\frac{1}{2} \end{pmatrix} \begin{pmatrix} (\mathbf{1})_{il}(\mathbf{1})_{kj} \\ (i\gamma_5)_{il}(i\gamma_5)_{kj} \\ (\gamma^\mu)_{il}(\gamma_\mu)_{kj} \\ (\gamma^\mu\gamma_5)_{il}(\gamma_\mu\gamma_5)_{kj} \\ (\sigma^{\mu\nu})_{il}(\sigma_{\mu\nu})_{kj} \end{pmatrix}, \tag{C.6}$$

$$\begin{aligned} (\gamma^0)_{ij}(\gamma^0)_{kl} = \quad & \frac{1}{4}[(\mathbf{1})_{il}(\mathbf{1})_{kj} + (i\gamma_5)_{il}(i\gamma_5)_{kj} \\ & +(\gamma^0)_{il}(\gamma^0)_{kj} - (\gamma^m)_{il}(\gamma_m)_{kj} + (\gamma^0\gamma_5)_{il}(\gamma^0\gamma_5)_{kj} - (\gamma^m\gamma_5)_{il}(\gamma_m\gamma_5)_{kj} \\ & -(\sigma^{0n})_{il}(\sigma_{0n})_{kj} + (\sigma^{mn})_{il}(\sigma_{mn})_{kj}], \end{aligned} \tag{C.7}$$

$$\begin{pmatrix} (\mathbf{1})_{ij}(\mathbf{1})_{kl} \\ (i\gamma_5)_{ij}(i\gamma_5)_{kl} \\ (\gamma^\mu)_{ij}(\gamma_\mu)_{kl} \\ (\gamma^\mu\gamma_5)_{ij}(\gamma_\mu\gamma_5)_{kl} \\ (\sigma^{\mu\nu})_{ij}(\sigma_{\mu\nu})_{kl} \end{pmatrix} = \begin{pmatrix} \frac{1}{4} & -\frac{1}{4} & \frac{1}{4} & -\frac{1}{4} & -\frac{1}{8} \\ -\frac{1}{4} & \frac{1}{4} & \frac{1}{4} & -\frac{1}{4} & \frac{1}{8} \\ 1 & 1 & -\frac{1}{2} & -\frac{1}{2} & 0 \\ 1 & 1 & \frac{1}{2} & \frac{1}{2} & 0 \\ -3 & 3 & 0 & 0 & -\frac{1}{2} \end{pmatrix} \begin{pmatrix} (i\gamma_5 C)_{ik}(Ci\gamma_5)_{lj} \\ (C)_{ik}(C)_{lj} \\ (\gamma^\mu\gamma_5 C)_{ik}(C\gamma_\mu\gamma_5)_{lj} \\ (\gamma^\mu C)_{ik}(C\gamma_\mu)_{lj} \\ (\sigma^{\mu\nu}C)_{ik}(C\sigma_{\mu\nu})_{lj} \end{pmatrix}, \tag{C.8}$$

$$\begin{aligned} (\gamma^0)_{ij}(\gamma^0)_{kl} = \quad & \frac{1}{4}[(i\gamma_5 C)_{ik}(Ci\gamma_5)_{lj} + (C)_{ik}(C)_{lj} \\ & +(\gamma^0\gamma_5 C)_{ik}(C\gamma^0\gamma_5)_{lj} - (\gamma^m\gamma_5 C)_{ik}(C\gamma_m\gamma_5)_{lj} + (\gamma^0 C)_{ik}(C\gamma^0)_{lj} - (\gamma^m C)_{ik}(C\gamma_m)_{lj} \\ & -(\sigma^{0n}C)_{ik}(C\sigma_{0n})_{lj} + (\sigma^{mn}C)_{ik}(C\sigma_{mn})_{lj}]. \end{aligned} \tag{C.9}$$

The similar decomposition for the generators of $U(N)$ is the following. We define $\tau_a (a = 1, ..., N^2-1)$ as the generators for $SU(N)$ normalized by $\mathrm{tr}[\tau_a\tau_b] = 2\delta_{ab}$. Under these definitions, the the quark-antiquark interaction can be written as

$$\begin{pmatrix} (\mathbf{1})_{ij}(\mathbf{1})_{kl} \\ (\tau_a)_{ij}(\tau_a)_{kl} \end{pmatrix} = \begin{pmatrix} \frac{1}{N} & \frac{1}{2} \\ 2\frac{N^2-1}{N^2} & -\frac{1}{N} \end{pmatrix} \begin{pmatrix} (\mathbf{1})_{il}(\mathbf{1})_{kj} \\ (\tau_a)_{il}(\tau_a)_{kj} \end{pmatrix}. \tag{C.10}$$

On the other hand, interaction terms for quark-quark (antiqaurk-antiquark) is

$$\begin{pmatrix} (\mathbf{1})_{ij}(\mathbf{1})_{kl} \\ (\tau_a)_{ij}(\tau_a)_{kl} \end{pmatrix} = \begin{pmatrix} \frac{1}{2} & \frac{1}{2} \\ 2\frac{N-1}{N} & -\frac{N+1}{N} \end{pmatrix} \begin{pmatrix} (\tau_S)_{ik}(\tau_S)_{lj} \\ (\tau_A)_{ik}(\tau_A)_{lj} \end{pmatrix}. \tag{C.11}$$

Here, the subscript S means the symmetric generators and A corresponds to the anti-symmetric generators

By using these deformations, we can write down the interaction terms in $(2+1)$-NJL model in Chapter 3 by using the following current-current interaction

$$\mathcal{L}_{\mathrm{cur}} = -g(\bar{q}\gamma^\mu\tau_a q)^2. \tag{C.12}$$

By using above Fierz transformation for this $\mathcal{L}_{\mathrm{cur}}$,

$$\begin{aligned} \mathcal{L}_{\mathrm{ex}} = \quad & \frac{N_c^2-1}{N_f N_c^2} g \sum_{a=0}^{N_f^2-1} \left((\bar{q}\lambda_a q)^2 + (\bar{q}i\gamma_5\lambda_a q)^2 - \frac{1}{2}(\bar{q}\gamma^\mu\lambda_a q)^2 - \frac{1}{2}(\bar{q}\gamma^\mu\gamma_5\lambda_a q)^2 \right) \\ & -\frac{1}{2N_c} g \sum_{a=0}^{N_f^2-1} \left((\bar{q}\tau_{a'}\lambda_a q)^2 + (\bar{q}i\gamma_5\tau_{a'}\lambda_a q)^2 - \frac{1}{2}(\bar{q}\gamma^\mu\tau_{a'}\lambda_a q)^2 \right. \\ & \left. -\frac{1}{2}(\bar{q}\gamma^\mu\gamma_5\tau_{a'}\lambda_a q)^2 \right), \end{aligned} \tag{C.13}$$

$$
\begin{aligned}
\mathcal{L}_{\rm qq} = \quad & \frac{N_c+1}{2N_c} g(\bar{q} i\gamma_5 C\tau_A\lambda_{A'}\bar{q}^T)(q^T C i\gamma_5\tau_A\lambda_{A'}q) + (\bar{q}C\tau_A\lambda_{A'}\bar{q}^T)(q^T C\tau_A\lambda_{A'}q) \\
& -\frac{1}{2}(\bar{q}\gamma^\mu\gamma_5 C\tau_A\lambda_{A'}\bar{q}^T)(q^T C\gamma_\mu\gamma_5\tau_A\lambda_{A'}q) - \frac{1}{2}(\bar{q}\gamma^\mu C\tau_A\lambda_{S'}\bar{q}^T)(q^T C\gamma_\mu\tau_A\lambda_{S'}q) \\
& -\frac{N_c-1}{2N_c} g(\bar{q} i\gamma_5 C\tau_S\lambda_{S'}\bar{q}^T)(q^T C i\gamma_5\tau_S\lambda_{S'}q) + (\bar{q}C\tau_S\lambda_{S'}\bar{q}^T)(q^T C\tau_S\lambda_{S'}q) \\
& -\frac{1}{2}(\bar{q}\gamma^\mu\gamma_5 C\tau_S\lambda_{S'}\bar{q}^T)(q^T C\gamma_\mu\gamma_5\tau_S\lambda_{S'}q) \\
& -\frac{1}{2}(\bar{q}\gamma^\mu C\tau_S\lambda_{A'}\bar{q}^T)(q^T C\gamma_\mu\gamma_\mu\tau_S\lambda_{A'}q)
\end{aligned} \tag{C.14}
$$

are derived. Here λ_a (τ_a) are the generators for flavor (color) $SU(N)$. As a result, scalar-type four Fermi interaction $G_{_S}$ and diquark interaction H are

$$
G_{_S} = \frac{(N_c^2-1)}{N_c^2} g, \tag{C.15}
$$

$$
H = \frac{N_c+1}{2N_c} g. \tag{C.16}
$$

Especially, if $N_c = 3$, $H = \frac{3}{4}G_{_S}$ is obtained.

Appendix D

The Bogoliubov-Valatin Approach

In this appendix, we derive the gap equation in Chapter 3 by using the Bogoliubov-Valatin transformation and the Dyson-Schwinger approach. For simplicity, we consider $N_f = 2$ case with

$$\mathcal{L}_{\rm NJL} = \overline{q} i \partial\!\!\!/ q + \frac{1}{2} G_s [(\overline{q} q)^2 + (\overline{q} i \gamma_5 \tau^a q)^2]. \tag{D.1}$$

A quark field q is

$$q(x,0) = \sum_s \int \frac{d^3p}{(2\pi)^3} \left(b(\boldsymbol{p},s) u(\boldsymbol{p},s) e^{i\boldsymbol{p}\cdot\boldsymbol{x}} + d^\dagger(\boldsymbol{p},s) v(\boldsymbol{p},s) e^{-i\boldsymbol{p}\cdot\boldsymbol{x}} \right) \tag{D.2}$$

where b and d are the annihilation operator for the particle and antiparticle respectively and s means the helicity. $|0\rangle$ satisfies the following relations

$$b(\boldsymbol{p},s)\,|0\rangle = d(\boldsymbol{p},s)\,|0\rangle = 0. \tag{D.3}$$

$$p\!\!\!/ u(\boldsymbol{p},s) = p\!\!\!/ v(\boldsymbol{p},s) = 0,\ u^\dagger(\boldsymbol{p},s) u(\boldsymbol{p},s) = v^\dagger(\boldsymbol{p},s) v(\boldsymbol{p},s) = 1 \tag{D.4}$$

are also satisfied by spinors u, v. By the analogy with the BCS theory, we construct the following vacuum $|vac\rangle$

$$|vac\rangle = \prod_{\boldsymbol{p},s} \left(\cos\theta(p) + s\, \sin\theta(p) b^\dagger(\boldsymbol{p},s) d^\dagger(-\boldsymbol{p},s) \right) |0\rangle\,. \tag{D.5}$$

The difference from the BCS theory is that Eq. (D.5) considers the pairing between a particle and an anti-particle. On the other hand, BCS theory treats the pairing between the same kind of particles. If $\boldsymbol{p}$ is given, $|vac\rangle$ can be written down more explicitly,

$$\begin{aligned} |vac\rangle = & \cos^2\theta\,|0\rangle + \sin\theta\cos\theta b^\dagger(\boldsymbol{p},+) d^\dagger(-\boldsymbol{p},+)\,|0\rangle \\ & + \sin\theta\cos\theta b^\dagger(\boldsymbol{p},-) d^\dagger(-\boldsymbol{p},-)\,|0\rangle \\ & - \sin^2\theta b^\dagger(\boldsymbol{p},-) d^\dagger(-\boldsymbol{p},-) b^\dagger(\boldsymbol{p},+) d^\dagger(-\boldsymbol{p},+)\,|0\rangle\,. \end{aligned} \tag{D.6}$$

By Bogoliubov-Valatin transformation, we can obtain the annihilation operators B and D on $|vac\rangle$ defined by

$$B(\boldsymbol{p},s) = \cos\theta b(\boldsymbol{p},s) + s\sin\theta d^{\dagger}(-\boldsymbol{p},s), \tag{D.7}$$

$$D(\boldsymbol{p},s) = \cos\theta d(\boldsymbol{p},s) - s\sin\theta b^{\dagger}(-\boldsymbol{p},s). \tag{D.8}$$

B and D of course satisfy the following relations,

$$B(\boldsymbol{p},s)\,|vac\rangle = D(\boldsymbol{p},s)\,|vac\rangle = 0. \tag{D.9}$$

A quark field q can be decomposed by these operators as follows,

$$q(x,0) = \sum_s \int \frac{d^3p}{(2\pi)^3}\left(B(\boldsymbol{p},s)M_1(\boldsymbol{p},s)e^{i\boldsymbol{p}\cdot\boldsymbol{x}} + D^{\dagger}(\boldsymbol{p},s)M_2(\boldsymbol{p},s)e^{-i\boldsymbol{p}\cdot\boldsymbol{x}}\right) \tag{D.10}$$

where

$$M_1(\boldsymbol{p},s) = \left(\cos\theta + \gamma^0\sin\theta\right)u(\boldsymbol{p},s), \tag{D.11}$$

$$M_2(\boldsymbol{p},s) = \left(\cos\theta - \gamma^0\sin\theta\right)u(\boldsymbol{p},s). \tag{D.12}$$

By using the relations explained above, we can calculate the energy W under the mean field approximation,

$$W \equiv \langle vac|\,\mathcal{H}_{\rm NJL}\,|vac\rangle \tag{D.13}$$

$$= -2N_cN_f\int\frac{d^3p}{(2\pi)^3}p\cos\phi - 2G_{_S}(N_cN_f)^2\left[\int\frac{d^3p}{(2\pi)^3}\sin\phi\right]^2 \tag{D.14}$$

where $\phi = 2\theta$. Here we use

$$\gamma_0 sv(-\boldsymbol{p},s) = u(\boldsymbol{p},s),\ \sum_s u(\boldsymbol{p},s)u^{\dagger}(\boldsymbol{p},s) = \frac{1}{2}\left(1 - \gamma\cdot\frac{\boldsymbol{p}}{p}\gamma^0\right). \tag{D.15}$$

ϕ can be determined by minimizing W with respect to ϕ

$$\frac{\delta W}{\delta\phi} = 0. \tag{D.16}$$

After the calculation, we obtain

$$p\tan\phi = 2G_{_S}N_cN_f\int\frac{d^3p'}{(4\pi)^3}\sin\phi(p'), \tag{D.17}$$

which is the gap equation. Since the right hand side does not depend on p, we put the right hand side as M, which is not a function of p. Then

$$\tan\phi = \frac{M}{p},\ \sin\phi = \frac{M}{\sqrt{\boldsymbol{p}^2 + M^2}} \tag{D.18}$$

are achieved and from Eq. (D.17) we can finally obtain the usual gap equation:

$$M = 2G_S N_c N_f \int \frac{d^3p'}{(2\pi)^3} \frac{M}{\sqrt{\boldsymbol{p}^2 + M^2}}. \tag{D.19}$$

On the other hand, we can derive this gap equation more directly from the Dyson-Schwinger approach. In the Hartree approximation, we can obtain the following gap equation,

$$M = iG_S 4N_c N_f \int \frac{d^4p'}{(2\pi)^4} \frac{M}{p'^2 - M^2 + i\varepsilon}, \tag{D.20}$$

which is the same as Eq. (D.19). Here, the factor $4N_cN_f$ corresponds to the degree of freedom for the Dirac, color and flavor. If we consider the Hartree-Fock approximation, this gap equation changes to

$$M = 4iG_S \left(N_c N_f + \frac{1}{2}\right) \int \frac{d^4p'}{(2\pi)^4} \frac{M}{p'^2 - M^2 + i\varepsilon}. \tag{D.21}$$

Therefore, the gap equation Eq. (D.19) can be considered as the first order term of the $1/N_c$ expansion.

Appendix E

Calculation of the Thermodynamic Potential

In this appendix, we introduce the decomposition of the quark propagator S in Chapter 3 for the numerical calculation. For simplicity, we ignore G'_{D} which gives a coupling between the chiral condensate and the diquark condensate.

We explicitly calculate Eq. (3.33),

$$\left[S^{-1}\right]^{ij}_{\alpha\beta} = \begin{pmatrix} [G_0^+]^{-1} & \sum_{i=1,2,3} \Delta_i \gamma_5 \tilde{\lambda}_i \tilde{\tau}_i \\ -\sum_{i=1,2,3} \Delta_i^* \gamma_5 \tilde{\lambda}_i \tilde{\tau}_i & [G_0^-]^{-1} \end{pmatrix}. \tag{E.1}$$

In the following, we define

$$\Phi^- \equiv \sum_{i=1,2,3} \Delta_i \gamma_5 \tilde{\lambda}_i \tilde{\tau}_i \tag{E.2}$$

$$\Phi^+ \equiv -\sum_{i=1,2,3} \Delta_i^* \gamma_5 \tilde{\lambda}_i \tilde{\tau}_i. \tag{E.3}$$

$\Phi^{\pm}$ have the following relation

$$\Phi^+ = -(\Phi^-)^\dagger. \tag{E.4}$$

If we take the basis of the quark field q as

$$q = (q_r^u, q_r^d, q_r^s, q_g^u, q_g^d, q_g^s, q_b^u, q_b^d, q_b^s)^T \tag{E.5}$$

where u, d, s mean flavors of quarks and r, g, b correspond to the colors of quarks, Φ^- becomes

$$\Phi^- = -\gamma_5 \begin{pmatrix} 0 & 0 & 0 & 0 & \Delta_3 & 0 & 0 & 0 & \Delta_2 \\ 0 & 0 & 0 & -\Delta_3 & 0 & 0 & 0 & 0 & 0 \\ 0 & 0 & 0 & 0 & 0 & 0 & -\Delta_2 & 0 & 0 \\ 0 & -\Delta_3 & 0 & 0 & 0 & 0 & 0 & 0 & 0 \\ \Delta_3 & 0 & 0 & 0 & 0 & 0 & 0 & 0 & \Delta_1 \\ 0 & 0 & 0 & 0 & 0 & 0 & 0 & -\Delta_1 & 0 \\ 0 & 0 & -\Delta_2 & 0 & 0 & 0 & 0 & 0 & 0 \\ 0 & 0 & 0 & 0 & 0 & -\Delta_1 & 0 & 0 & 0 \\ \Delta_2 & 0 & 0 & 0 & \Delta_1 & 0 & 0 & 0 & 0 \end{pmatrix}. \tag{E.6}$$

By using the project operator $\mathcal{P}_\pm$ defined by

$$\mathcal{P}_\pm = \frac{1}{2}(1 \pm \boldsymbol{\sigma} \cdot \hat{\boldsymbol{k}}), \tag{E.7}$$

we can obtain the following two equations,

$$\gamma_0 [G_0^\pm]^{-1} = \sum_{s=\pm} \begin{pmatrix} p_0 \pm \hat{\mu} - \hat{M} & -sp \\ -sp & p_0 \pm \hat{\mu} + \hat{M} \end{pmatrix} \mathcal{P}_s \tag{E.8}$$

where each component of $\hat{\mu}$ is given by

$$\mu^{ij}_{\alpha\beta} = (\mu\delta^{ij} + \mu_Q Q^{ij})\delta_{\alpha\beta} + (\mu_3(\tau_3)_{\alpha\beta} + \mu_8(\tau_8)_{\alpha\beta})\delta^{ij},$$

$\hat{M}$ is the diagonal matrix in the flavor space $\hat{M} = \mathrm{diag}_f(M_u, M_d, M_s)$ and

$$\gamma_0 \Phi^\pm = \pm \sum_{s=\pm} \begin{pmatrix} 0 & \Phi \\ -\Phi & 0 \end{pmatrix} \mathcal{P}_s \tag{E.9}$$

where Φ is defined as

$$\Phi^\pm = \pm\gamma_5 \Phi. \tag{E.10}$$

Finally, $\gamma_0 S^{-1}$ can be decomposed into two parts by using $\mathcal{P}_\pm$,

$$\begin{aligned} \gamma_0 S^{-1} &= \sum_{s=\pm} \hat{S}_s^{-1} \mathcal{P}_s \\ \hat{S}_s^{-1} &= p_0 - \mathcal{M}_s \\ \mathcal{M}_s &= \begin{pmatrix} -\hat{\mu} + \hat{M} & sp & 0 & \Phi \\ sp & -\hat{\mu} - \hat{M} & -\Phi & 0 \\ 0 & -\Phi & \hat{\mu} + \hat{M} & sp \\ \Phi & 0 & sp & \hat{\mu} - \hat{M} \end{pmatrix}. \end{aligned} \tag{E.11}$$

Moreover, since $\det S^{-1} = \det(\gamma_0 S^{-1})$ and $\det S_+^{-1} = \det S_-^{-1}$ are satisfied, the determinant of the inverse quark propagator S^{-1} becomes

$$\det(S^{-1}) = \prod_{i=1}^{18} (p_0^2 - \varepsilon_i^2)^2. \tag{E.12}$$

Here, ε_i are eigenvalues of the matrix $\mathcal{M}_+$. The important point is this 36×36 matrix $\mathcal{M}_+$ can be decomposed into six 4×4 matrices and one 12×12 matrix. This decomposition makes the numerical calculation easy drastically. These matrices can be written as follows explicitly,

$$\mathcal{M}_+^1 = \begin{pmatrix} -\mu_r^d + M_d & p & 0 & -\Delta_3 \\ p & -\mu_r^d - M_d & \Delta_3 & 0 \\ 0 & \Delta_3 & \mu_g^u + M_u & p \\ -\Delta_3 & 0 & p & \mu_g^u - M_u \end{pmatrix}, \tag{E.13}$$

$$\mathcal{M}_+^2 = \begin{pmatrix} \mu_r^d - M_d & p & 0 & -\Delta_3 \\ p & \mu_r^d + M_d & \Delta_3 & 0 \\ 0 & \Delta_3 & -\mu_g^u - M_u & p \\ -\Delta_3 & 0 & p & -\mu_g^u + M_u \end{pmatrix}, \tag{E.14}$$

$$\mathcal{M}_+^3 = \begin{pmatrix} -\mu_r^s + M_s & p & 0 & -\Delta_2 \\ p & -\mu_r^s - M_s & \Delta_2 & 0 \\ 0 & \Delta_2 & \mu_b^u + M_u & p \\ -\Delta_2 & 0 & p & \mu_b^u - M_u \end{pmatrix}, \tag{E.15}$$

$$\mathcal{M}_+^4 = \begin{pmatrix} \mu_r^s - M_s & p & 0 & -\Delta_2 \\ p & \mu_r^s + M_s & \Delta_2 & 0 \\ 0 & \Delta_2 & -\mu_b^u - M_u & p \\ -\Delta_2 & 0 & p & -\mu_b^u + M_u \end{pmatrix}, \tag{E.16}$$

$$\mathcal{M}_+^5 = \begin{pmatrix} -\mu_g^s + M_s & p & 0 & -\Delta_1 \\ p & -\mu_g^s - M_s & \Delta_1 & 0 \\ 0 & \Delta_1 & \mu_b^d + M_d & p \\ -\Delta_1 & 0 & p & \mu_b^d - M_d \end{pmatrix}, \tag{E.17}$$

$$\mathcal{M}_+^6 = \begin{pmatrix} \mu_g^s - M_s & p & 0 & -\Delta_1 \\ p & \mu_g^s + M_s & \Delta_1 & 0 \\ 0 & \Delta_1 & -\mu_b^d - M_d & p \\ -\Delta_1 & 0 & p & -\mu_b^d + M_d \end{pmatrix}, \tag{E.18}$$

$$\mathcal{M}_{+}^{7}=\begin{pmatrix}
-\mu_r^u-M_u & p & 0 & 0 & 0 & 0 & 0 & -\Delta_3 & 0 & 0 & 0 & -\Delta_2 \\
p & -\mu_r^u+M_u & 0 & 0 & 0 & 0 & \Delta_3 & 0 & 0 & 0 & \Delta_2 & 0 \\
0 & 0 & \mu_r^u-M_u & p & 0 & \Delta_3 & 0 & 0 & 0 & \Delta_2 & 0 & 0 \\
0 & 0 & p & \mu_r^u+M_u & -\Delta_3 & 0 & 0 & 0 & -\Delta_2 & 0 & 0 & 0 \\
0 & 0 & 0 & -\Delta_3 & -\mu_g^d-M_d & p & 0 & 0 & 0 & 0 & 0 & -\Delta_1 \\
0 & 0 & \Delta_3 & 0 & p & -\mu_g^d+M_d & 0 & 0 & 0 & 0 & \Delta_1 & 0 \\
0 & \Delta_3 & 0 & 0 & 0 & 0 & \mu_g^d-M_d & p & 0 & \Delta_1 & 0 & 0 \\
-\Delta_3 & 0 & 0 & 0 & 0 & 0 & p & \mu_g^d+M_d & -\Delta_1 & 0 & 0 & 0 \\
0 & 0 & 0 & -\Delta_2 & 0 & 0 & 0 & -\Delta_1 & -\mu_b^s-M_s & p & 0 & 0 \\
0 & 0 & \Delta_2 & 0 & 0 & 0 & \Delta_1 & 0 & p & -\mu_b^s+M_s & 0 & 0 \\
0 & \Delta_2 & 0 & 0 & 0 & \Delta_1 & 0 & 0 & 0 & 0 & \mu_b^s-M_s & p \\
-\Delta_2 & 0 & 0 & 0 & -\Delta_1 & 0 & 0 & 0 & 0 & 0 & p & \mu_b^s+M_s
\end{pmatrix} \tag{E.19}$$

Here, we use the chemical potential $\hat{\mu}$ defined in Eq. (E.9) is the diagonal in the flavor and color space. We define $\mu_{\alpha\alpha}^{ii} \equiv \mu 6 i_\alpha$. Then, we can finally obtain the thermodynamic potential Ω

$$\begin{aligned}
\Omega &= -\frac{1}{4\pi^2}\sum_{i=1,36}\int_0^\Lambda dp p^2\left(|\varepsilon_i| + 2T\ln\left(1+e^{-|\varepsilon_i/T|}\right)\right) \\
&\quad + G_{_S}\sum_i \sigma_i^2 + 4G_{_D}\sigma_u\sigma_d\sigma_s - \frac{1}{2}g_{_V}\left(\sum_i n_i\right)^2 + \sum_{\text{color}}\frac{|\Delta_c|^2}{2H}
\end{aligned} \tag{E.20}$$

by using

$$-\frac{T}{2}\sum_i\sum_\ell\int\frac{d^3p}{(2\pi)^3}\text{Trln}\left(\frac{S_i^{-1}(i\omega_\ell,\mathbf{p})}{T}\right) = -\frac{1}{4\pi^2}\sum_{i=1,36}\int_0^\Lambda dp p^2\left(|\varepsilon_i| + 2T\ln\left(1+e^{-|\varepsilon_i/T|}\right)\right),$$

$$T\sum_n \ln\left(\frac{1}{T^2}(\omega_n^2+\lambda_k^2)\right) = \lambda_k + 2T\ln(1+e^{-\lambda_k/T}). \tag{E.21}$$

Appendix F

Crossover at Finite Temperature

In this appendix, we summarize the previous work [106], in which the phenomenological interpolation of the entropy density as a function of the temperature was suggested. This model can reproduce some of results of the lattice QCD Monte Carlo simulations at least qualitatively.

Among a lot of unique properties for the non-perturbative effect, which were found by the lattice QCD simulations, we focus on the following three characteristics.

- P/T^4 approaches the Stefan-Boltzmann limit smoothly as the temperature T increases.
- ε/T^4 has the peak at T_c and approaches the high temperature limit from above as the temperature T increases.
- At the region $T > T_c$, the trace anomaly $\varepsilon - 3P$ takes a large value.

From the thermodynamic laws, we require the following condition for the entropy density s

$$\frac{\partial s(T)}{\partial T} > 0, \tag{F.1}$$

$$s(0) = 0. \tag{F.2}$$

To satisfy these conditions, we define s as

$$s(T) = s_{_H}(T)w_{_H}(T) + s_{_Q}(T)w_{_Q}(T) \tag{F.3}$$

$$w_{_Q}(T) = \frac{n\left(1+\tanh\left(\frac{T-T_c}{\Gamma}\right)\right)}{m\left(1-\tanh\left(\frac{T-T_c}{\Gamma}\right)\right)+n\left(1+\tanh\left(\frac{T-T_c}{\Gamma}\right)\right)}, \tag{F.4}$$

$$w_{_H} = 1 - w_{_Q}. \tag{F.5}$$

Here, $s_{_H}(T)(s_{_Q}(T))$ is the entropy density for the hadronic (quark) phase for the massless and

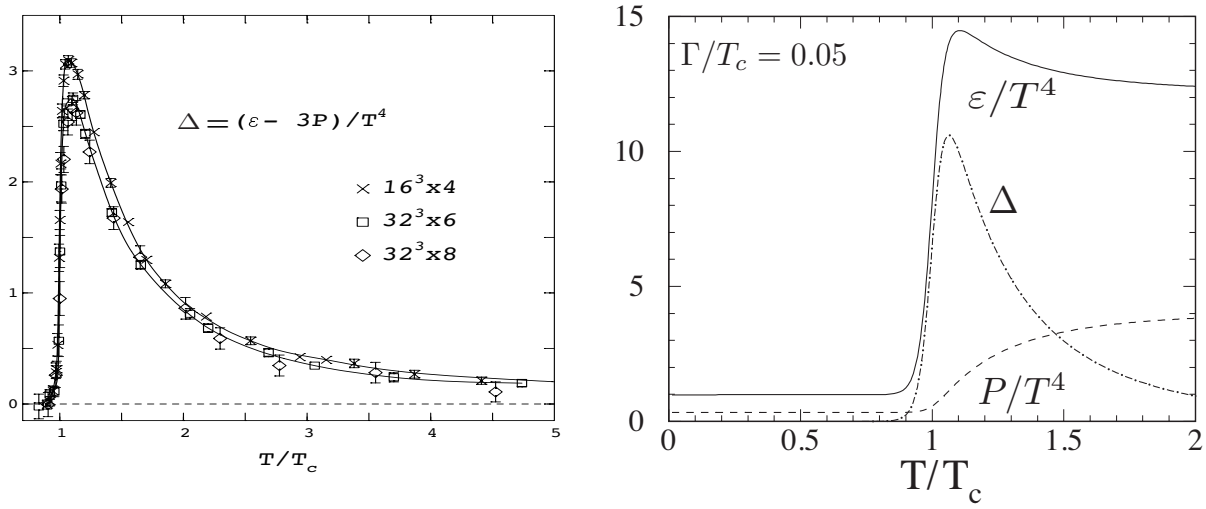

(a) Lattice QCD caluculation (b) Phenomenological caluculation

Figure F.1: (a) The trace anomaly $\varepsilon - 3P$ calculated through lattice QCD simulations [135]. (b) P/T^4, ε/T^4 and the trace anomaly calculated from the phenomenological model ($m = n$) [106].

2-flavor matter,

$$s_{_H}(T) = 12\frac{\pi^2 T^3}{90}, \tag{F.6}$$

$$s_{_Q}(T) = 148\frac{\pi^2 T^3}{90}. \tag{F.7}$$

$m,\ n$ correspond to the asymmetry between hadronic and quark phases. From the definition of the weight function $w_{H/Q}$, in the region $T - T_c \ll \Gamma$, the EOS reaches at the pure hadronic EOS and in the region $T - T_c \gg \Gamma$, the system becomes the pure quark matter. Therefore, this model satisfies the description discussed above: The resultant thermodynamic properties approach the non-interactive hadronic or quark matter at the low or high temperature region and have the non-trivial behavior at the intermediate region $T_c - \Gamma < T < T_c + \Gamma$.

From this entropy density Eq. (F.3), we can derive the other thermodynamical quantities analytically through the thermodynamical relations.

$$P(T) = \int_0^T s(t)dt, \tag{F.8}$$

$$\varepsilon(T) = Ts(T) - P(T). \tag{F.9}$$

In Fig. F.1 (a) [135], the lattice QCD calculation of the trace anomaly $\varepsilon - 3P$ as a function of the temperature normalized by the critical temperature T_c is plotted. Fig. F.1 (b) [106] shows

P/T^4, ε/T^4 and the trace anomaly $\Delta \equiv \varepsilon - 3P$ calculated from this phenomenological model ($m = n$). We can see from these figures that this phenomenological interpolation method of the entropy density as a function of the temperature using the function "tanh" can reproduce at least three non-perturbative effects in the intermediate region quantitatively.

Finally, Iet us comment on the proof that ε/T^4 has the peak at T_c analytically. By considering

$$\begin{aligned} T^5 \frac{\partial\left(\varepsilon/T^4\right)}{\partial T} &= T^2\left(s_{_H}(T)\frac{\partial w_{_H}(T)}{\partial T} + s_{_Q}(T)\frac{\partial w_{_Q}(T)}{\partial T}\right) \\ &\quad - \int_0^T dt\ t\left(s_{_H}(t)\frac{\partial w_{_H}(t)}{\partial t} + s_{_Q}(t)\frac{\partial w_{_Q}(t)}{\partial t}\right), \end{aligned} \tag{F.10}$$

$$s_{H,Q}(T) \propto T^3, \tag{F.11}$$

$$\frac{\partial w_{_Q}(t)}{\partial t} > 0, \tag{F.12}$$

$$\frac{\partial w_{_Q}(t)}{\partial t} \to \mathcal{O}(1/t^4)\ (t \to \infty), \tag{F.13}$$

we can easily prove that $T^5\frac{\partial\left(\varepsilon/T^4\right)}{\partial T}$ is positive (negative) at the region where T is small (large). Therefore, ε/T^4 has the peak.

References

[1] K. Masuda, T. Hatsuda, and T. Takatsuka. *Astrophys. J. 764, 12*, 2013.

[2] K. Masuda, T. Hatsuda, and T. Takatsuka. *PTEP 2013, no. 7, 073D01*, 2013.

[3] K. Masuda, T. Hatsuda, and T. Takatsuka. *arXiv:1508.04861*.

[4] K. Masuda, T. Hatsuda, and T. Takatsuka. *arXiv:1506.00984*, (accepted for publication in PTEP).

[5] K. Masuda and M. Nitta. *arXiv: 1512.01946*.

[6] T. Muta. Foundation of Quantum Chromodynamics: an introduction to Perturbative Methods in Gauge Theories. *World Scientific, Singapore*, 1998.

[7] Particle Data Group. *Chin. Phys. C38, 090001*, 2014.

[8] D. J. Gross and F. Wilczek. *Phys. Rev. Lett. 30, 1343*, 1973.

[9] H. D. Politzer. *Phys. Rev. Lett. 30, 1346*, 1973.

[10] A. Bazavov. Proceedings, 32nd international symposium on lattice field theory (lattice 2014). *arXiv: 1505.05543*.

[11] K. Fukushima and T. Hatsuda. *Rept. Prog. Phys. 74, 014001*, 2011.

[12] P. Braun-Munzinger, B. Friman, and J. Stachel (eds.). Proceedings, 24th international conference on ultra-relativistic nucleus-nucleus collisions (quark matter 2014). *Nucl.Phys. A931, 1*, 2014.

[13] K. Fukushima and C. Sasaki. *Prog. Part. Nucl. Phys. 72, 99*, 2013.

[14] N. Ishii, S. Aoki, and T. Hatsuda. *Phys.Rev.Lett. 99, 022001*, 2007.

[15] J. M. Lattimer and M. Prakash. *Phys. Rept. 442, 109*, 2007.

[16] A. W. Steiner, J. M. Lattimer, and E. F. Brown. *arXiv:1510.07515*.

[17] P. B. Demorest, T. Pennucci, S. M. Ranson, M. S. E. Roberts, and J. W. T. Hessels. *Nature 467, 1081*, 2010.

[18] J. Antoniadis, P. C. C. Freire, N. Wex, T. M. Tauris, R. S. Lynch, M. H. van Kerkwijk, M. Kramer, and C. Bassa it et al. *Science 340, 6131*, 2013.

[19] G. Baym, C. Pethick, and P. Sutherland. *Astrophys. J. 170, 299*, 1971.

[20] S. Guillot and R. E. Rutledg. *Astrophys. J. 796, 1, L3*, 2010.

[21] V. Suleimanov, J. Poutanen, M. Revnivtsev, and K. Werner. *Astrophys. J. 742, 122*, 2011.

[22] A. W. Steiner, J. M. Lattimer, and E. F. Brown. *Astrophys. J. 765, L5*, 2013.

[23] F. Ozel, D. Psaltis, T. Guver, G. Baym, C. Heink, and S. Guillot. *arXiv:1505.05155.*

[24] T. Takatsuka. *Prog. Theor. Phys. Suppl. 156, 84*, 2004.

[25] S. Weissenborn, D. Chatterjee, and J. Schaffner-Bielich. *Nucl. Phys. A 881, 62*, 2010.

[26] H. J. Schulze, A. Polls, A. Ramos, and I. Vidana. *Phys. Rev. C 73, 058801*, 2006.

[27] T. Takatsuka, S. Nishizaki, and R. Tamagaki. *Proc. Int. Symp. "FM50" (AIP Conference proceedings) 209*, 2008.

[28] F. Ozel, D. Psaltis, S. Ransom, P. B. Demorest, and M. Alford. *Astrophys. J. 724, 1199*, 2010.

[29] H. Djapo, B. J. Schaefer, and J. Wambach. *Phys. Rev. C 81, 035803*, 2010.

[30] A. Kurkela, P. Romatschke, A. Vuorinen, and B. Wu. *arXiv 1006.4062 [astro-ph.HE].*

[31] S. Nishizaki, Y. Yamamoto, and T. Takatsuka. *Prog. Theor. Phys.105, 607*, 2001.

[32] T. Takatsuka. *Prog. Theor. Phys. 95, 901*, 1996.

[33] L. F. Roberts, G. Shen, V. Cirigliano, J. A. Pons, S. Reddy, and S. E. Woosley. *Phys. Rev. Lett. 108, 061103*, 2012.

[34] M. Prakash, J. M. Lattimer, J. A. Pons, A. W. Steiner, and S. Reddy. *Lect. Notes Phys. 578, 364*, 2001.

[35] H. T. Janka. *Ann. Rev. Nucl. Part. Sci. 62, 407*, 2012.

[36] L. F. Roberts. *Astrophys. J. 755, 126*, 2012.

[37] T. Takatsuka, T. Hatsuda, and K. Masuda. *Proceedings of the 11th Int. Symp. on "Origin of Matter and Evolution of Galaxies (OMEG 11)"*, 2011.

[38] M. A. Baranov. *Phys. Rept. 464, 71*, 2008.

[39] G. Baym. *Physica 96A, 131*, 1979.

[40] T. Celik, F. Karsch, and H. Satz. *Phys. Lett. B 97, 128*, 1980.

[41] T. Schafer and F. Wilczek. *Phys. Rev. Lett. 82, 3956*, 1999.

[42] K. Fukushima. *Phys. Lett. B 591, 277*, 2004.

[43] T. Hatsuda, M. Tachibana, N. Yamamoto, and G. Baym. *Phys. Rev. Lett. 97, 122001*, 2006.

[44] K. Maeda, G. Baym, and T. Hatsuda. *Phys. Rev. Lett. 103, 085301*, 2009.

[45] D. E. Alvarez-Castillo, S. Benic, D. Blaschke, and R. Lastowiecki. *Acta Phys. Polon. Supp. 7, no. 1, 203*, 2014.

[46] T. Hell and W. Weise. *Phys. Rev. C 90, no. 4, 045801*, 2014.

[47] T. Kojo, P. D. Powell, Y. Song, and G. Baym. *Phys. Rev. D 91, no. 4, 045003*, 2015.

[48] H. Yukawa. *Proc. Phys. Math. Soc. Jap. 17, 48*, 1935.

[49] M. Taketani, S. Nakamura, and M. Sasaki. *PTP. 6, 581*, 1951.

[50] M. Taketani. *PTP. S3, 1*, 1956.

[51] Jr. R. V. Reid. *Annals Phys. 50, 411*, 1968.

[52] W. N. Cottingham, M. Lacombe, B. Loiseau, J. M. Richard, and R. Vinhman. *Phys. Rev. D 8, 800*, 1973.

[53] R. B. Wiringa, V. Stoks, and R. Schiavilla. *Phys. Rev. C 51, 38*, 1995.

[54] M. M. Nagels, T.A. Rijken, and J. J. deSwart. *Phys. Rev. D 15, 2547*, 1977.

[55] M. M. Nagels, T.A. Rijken, and J. J. deSwart. *Phys. Rev. D 20, 1633*, 1979.

[56] T. A. Rijken, V. G. J. Stoks, and Y. Yamamoto. *Phys. Rev. C 59, 21*, 1999.

[57] T. Nagae. *Prog. Theor. Phys. Suppl. 185, 299*, 2010.

[58] H. Tamura. *Prog. Theor. Phys. Suppl. 185, 315*, 2010.

[59] K. Nakazawa and H. Takahashi. *Prog. Theor. Phys. Suppl. 185, 335*, 2010.

[60] T. Inoue it et al. [HAL QCD Collaboration]. *Nucl. Phys. A 881, 28*, 2012.

[61] Y. Yamamoto, T. Motoba, H. Himeno, K. Ikeda, and S. Nagata. *Prog. Theor. Phys. Suppl. 117, 361*, 1994.

[62] I. E. Lagaris and V. R. Pandharipande. *Nucl. Phys. A 359, 331*, 1981.

[63] B. Friedman and V. R. Pandharipande. *Nucl. Phys. A 361, 502*, 1981.

[64] S. Nishizaki, T. Takatsuka, and J. Hiura. *PTP 92, 1*, 1994.

[65] A. Akmal, V.R. Pandharipande, and D.G. Ravenhall. *Phys. Rev. C 58, 1804*, 1998.

[66] B. D. Day. *Rev.Mod.Phys. 39, 719*, 1967.

[67] R. Rajaraman and H. A. Bethe. *Rev.Mod.Phys. 39, 745*, 1967.

[68] B. H. Brandow. *Rev.Mod.Phys. 39, 771*, 1967.

[69] M. Gell-Mann and F. Low. *Phys. Rev. 84, 350*, 1951.

[70] M. Baldo. Nuclear methods and the nuclear equation of state. *World Scientific, Singapore*, 1999.

[71] K. Tsubakihara, H. Maekawa, H. Matsumiya, and A. Ohnishi. *Phys. Rev. C 81, 065206*, 2010.

[72] S. Okubo. *Phys. Lett. 5, 165*, 1963.

[73] G. Zweig. Developments in the quark theory of hadrons (hadronic press, massachusetts). 1980.

[74] J. Iizuka. *PTP. S37, 3*, 1966.

[75] S. Nishizaki, Y. Yamamoto, and T. Takatsuka. *Prog. Theor. Phys. 108, 703*, 2002.

[76] M. Baldo, G.F. Burgio, and H.J. Schulze. *Phys. Rev. C 61, 055801*, 2000.

[77] I. Vidana. *AIP Conf. Proc.1645, 79*, 2015.

[78] T. Takatsuka, S. Nishizaki, and R. Tamagaki. *AIP con. proc. 1011 p.209*, 2008.

[79] Y. Yamamoto, T. Furumoto, N. Yasutake, and T. A. Rijken. *Phys. Rev. C 90, 045805*, 2014.

[80] D. Lonardoni, A. Lovato, S. Gandolfi, and F. Pederiva. *Phys. Rev. Lett. 114, no. 9, 092301*, 2015.

[81] T. Katayama and K. Saito. *Phys. Lett. B 747, 43*, 2015.

[82] Z. H. Li and H.J. Schulze. *Phys. Rev. C 78, 028801*, 2008.

[83] H.J. Schulze and T. Rijken. *Phys. Rev. C 84, 035801*, 2011.

[84] Y. Nambu. *Phys. Rev. Lett. 4, 380*, 1960.

[85] J. Goldstone, A. Salam, and S. Weinberg. *Phys. Rev. 127, 965*, 1962.

[86] M. Gell-Mann, R. J. Oakes, and B. Renner. *Phys. Rev. 175, 2195*, 1968.

[87] D. Bailin and A. Love. *Phys. Rept. 107, 325*, 1984.

[88] T. Schafer. *Nucl. Phys. B 575, 269*, 2000.

[89] R. D. Pisarski and D. H. Rischke. *Phys. Rev. Lett. 83, 37*, 1999.

[90] A.J. Paterson. *Nucl. Phys. B 190, 188*, 1981.

[91] M. Alford, K. Rajagopal, and F. Wilczek. *Phys. Lett. B 422, 247*, 1998.

[92] E. D'Hoker and J. Goldston. *Phys. Lett. B158, 429*, 1985.

[93] M. Kobayashi and T. Maskawa. *Prog. Theor. Phys. 44, 1422*, 1970.

[94] G. 't Hooft. *Phys. Rev. D 14, 3432*, 1976.

[95] A. Kurkela, P. Romatschke, and A. Vuorine. *Phys. Rev. D 81, 105021*, 2010.

[96] U. Vogel and W. Weise. *Prog. Part. Nucl. Phys. 27, 195*, 1991.

[97] S. P. Klevansky. *Rev. Mod. Phys. 64, 649*, 1992.

[98] T. Hatsuda and T. Kunihiro. *Phys. Rep. 247, 221*, 1994.

[99] M. Buballa. *Phys. Rept. 407, 205*, 2005.

[100] N. M. Bratovic, T. Hatsuda, and W. Weise. *Phys. Lett. B 719, 131*, 2013.

[101] O. Lourenco, M. Dutra, T. Frederico, A. Delfino, and M. Malheiro. *Phys. Rev. D 85, 097504*, 2012.

[102] N. Yamamoto, M. Tachibana, T. Hatsuda, and G. Baym. *Phys. Rev. D 76, 074001*, 2007.

[103] H. Abuki, G. Baym, T. Hatsuda, and N. Yamamoto. *Phys. Rev. D 81, 125010*, 2010.

[104] K. Fukushima and T. Kojo. *arXiv:1509.00356 [nucl-th].*

[105] G. Baym, T. Hatsuda, M. Tachibana, and N. Yamamoto. *J. Phys. G 35, 104021*, 2008.

[106] M. Asakawa and T. Hatsuda. *Phys. Rev. D 55, 4488*, 1997.

[107] J. P. Blaizot and J. Y. Ollitrault. *Phys. Lett. B 191, 21*, 1987.

[108] J. P. Blaizot and J. Y. Ollitrault. *Phys. Rev. D 36, 916*, 1987.

[109] F.Ozel, A.Gould, and T.Guver. *Astrophys.J.748*, 2012.

[110] S. Shlomo, V. M. Kolomietz, and G. Colo. *Eur. Phys. J. A 30, 23*, 2006.

[111] S. L. Shapiro and S. A. Teukolsky. lack holes, white dwarfs, and neutron stars: the physics of compact objects. *John Wiley and Sons, New York*, 1983.

[112] M. Alford, M. Braby, M. W. Paris, and S. Reddy. *Astrophys. J. 629, 969*, 2005.

[113] R. Lastowiecki, D. Blaschke, T. Fischer, and T. Klahn. *arXiv:1503.04832 [nucl-th].*

[114] M. Prakash, J. R. Cooke, and J. M. Lattimer. *Phys. Rev. D 52, 661*, 1995.

[115] K. Nakazato, K. Sumiyoshi, and S. Yamada. *Phys. Rev. D 77, 103006*, 2008.

[116] G. Pagliara, M. Hempel, and J. Schaffner-Bielich. *Phys. Rev. Lett 103, 171102*, 2009.

[117] H. Chen, G. F. Burgio, H. J. Schulze, and N. Yasutake. *Astron. Astrophys. 551, A13*, 2013.

[118] M. Hempel and J. Schaffner-Bielich. *Nucl. Phys. A 837, 210*, 2010.

[119] N. Buyukcizmeci, A. S. Botvina, I. N. Mishustin, R. Ogul, M. Hempel, J. Schaffner-Bielich, F.-K. Thielemann, and S. Furusawa it et al. *Nucl. Phys. A 907, 13*, 2013.

[120] G. H. Bordbar and M. Bigdeli. *Phys. Rev. C77, 015805*, 2008.

[121] T. Tatsumi. *Phys. Lett. B 489, 280*, 2000.

[122] T. Tatsumi. *arXiv:1107.0807.*

[123] R. Yoshiike, K. Nishiyama, and T. Tatsumi. *arXiv:1507.02110.*

[124] M. Eto, K. Hashimoto, and T. Hatsuda. *Phys. Rev. D 88, 081701*, 2013.

[125] J. A. Sauls, D. L. Stein, and J. W. Serene. *Phys. Rev. D 25, 967*, 1982.

[126] T. Fujita and T. Tsuneto. *Prog. Theor. Phys. 48, 766*, 1972.

[127] R. W. Richardson. *Phys. Rev. D 5 , 1883*, 1972.

[128] J. A. Sauls. PhD thesis, SUNY Stony Brook, 5 1980.

[129] N. D. Mermin. *Phys. Rev. A9, 868*, 1974.

[130] J. Sauls and J. Serene. *Phys. Rev. D17, 1524*, 1978.

[131] R. Barnett, A. Turner, and E. Demler. *Phys. Rev. Lett. 97, 180412*, Nov 2006.

[132] S. Kobayashi, M. Kobayashi, Y. Kawaguchi, M. Nitta, and M. Ueda. *Nucl. Phys. B856, 577*, 2012.

[133] S. Kobayashi, Y. Kawaguchi, M. Nitta, and M. Ueda. *Phys. Rev. A86 023612*, 2012.

[134] P. Muzikar, J. A. Sauls, and J. W. Serene. *Phys. Rev. D 21, 1494*, 1980.

[135] F. Karsch. *arXiv:hep-lat/9512029*.